Interreg
Öresund-Kattegat-Skagerrak
European Regional Development Fund

EUROPEAN UNION

ESS & MAX IV:
Cross Border
Science and Society

MAX4ESSFUN

annual meeting

2016

Interreg
Öresund-Kattegat-Skagerrak
European Regional Development Fund

EUROPEAN UNION

ESS & MAX IV:
Cross Border
Science and Society

MAX4ESSFUN Annual Meeting 2016

Poster Book

UNIVERSITY OF COPENHAGEN

LUND UNIVERSITY

CHALMERS
UNIVERSITY OF TECHNOLOGY

UNIVERSITY OF GOTHENBURG

MALMÖ UNIVERSITY

UiO : University of Oslo

Technical University of Denmark

DTU

ESS EUROPEAN SPALLATION SOURCE

MAX IV LABORATORY

AARHUS UNIVERSITET

Interreg
Öresund-Kattegat-Skagerrak
European Regional Development Fund

EUROPEAN UNION

ESS & MAX IV:
Cross Border
Science and Society

The picture of the European Spallation Source is printed with the courtesy of ESS/Team Henning Larsen Architects.

The photograph of MAX IV is taken by Lars B. Dahlin.

Printed at Media-Tryck, Lund University

Interreg
Öresund-Kattegat-Skagerrak
European Regional Development Fund

EUROPEAN UNION

ESS & MAX IV:
Cross Border
Science and Society

ESS & MAX IV: Cross Border Science and Society is a three-year project (ending on August 31, 2018) involving 27 different partners within the ÖKS region. The aim of the project is for the region to be internationally leading in the use of neutrons and synchrotron light. A primary goal is to increase the regional potential to exploit the unique large-scale research facilities ESS and MAX IV in the future.

The subproject MAX4ESSFUN involves 10 partner organizations, 8 universities (University of Copenhagen, Lund University, Chalmers University of Technology, University of Gothenburg, Malmö University, University of Oslo, Technical University of Denmark, Aarhus University) together with ESS and MAX IV. The subproject aims to stimulate collaborative research across national borders for researchers using neutrons and synchrotron light. It builds on research strengths in the region and developing new research areas by regional synergies is an important goal. The program provides direct support for PhD student and postdoc projects, in addition to an educational package of courses, workshops and summer schools.

The main goals of MAX4ESSFUN are:

- To increase the number of researchers in the region with expertise in experiments with neutrons and/or synchrotron light.
- To establish an inter-regional network of researchers from universities and facilities that will facilitate future research.
- Develop a framework for education of PhD students and postdocs. This includes carrying out experiments in regional constellations, courses and workshops.
- Increase the overall potential of scientific research at the facilities by building on the complementary strengths of different institutions in the region, and by educating young researchers.

For more information please contact us at **max4essfun@chem.ku.dk**

Interreg
Öresund-Kattegat-Skagerrak
European Regional Development Fund

EUROPEAN UNION

ESS & MAX IV:
Cross Border
Science and Society

Annual meeting MAX4ESSFUN 2016, 6-7th of October at ELITE Hotel Ideon in Lund

Program

Thursday, October 6

11.30	Registration
12.00	Lunch
13.00	Welcome by the organizers ESS and MAX IV state of the art including status of beam lines, Yngve Cerenius (MAX IV) and Pascale Deen (ESS)
14.00	CBSS and MAX4ESSFUN, Eskil Mårtensson (Region Skåne) and Jakob Øster (The Capital Region of Denmark) Presentation of activities in MAX4ESSFUN, Sine Larsen (University of Copenhagen) and Stacey Sörensen (Lund University)
14.30	Small scale complementary facilities/instruments Core technologies for life Science: Lund University Protein Production Platform Wolfgang Knecht (Lund University) Visions for the DTU Imaging Center, Anders Björholm Dahl (DTU) Norwegian Center for Neutron Research – NcNeutron, Magnus Helgerud Sørby (Kjeller)
15.00	Coffee/tea and afternoon snacks
15.30	*Theme 1: Imaging and Material Sciences,* chair Anders Bjørholm Dahl (DTU) In-situ neutron imaging of solid oxide electrochemical cells, Luise Theil Kuhn (DTU) X-ray scanning probe microscopy - imaging of x-ray scattering, Martin Bech (Lund University) Photoelectron spectroscopy of negative ions, Dag Hanstorp (University of Gothenburg)
17.00	Poster session, networking
19.00	Dinner

Friday, October 7

9.00	*Theme 2: Structural biology*, chair Gregers Rom Andersen (Aarhus University) Regulation of water and glycerol by eukaryotic aquaporins, Karin Lindkvist (Lund University) Membrane protein structures - where do we go, Poul Nissen (Aarhus University) MicroMAX and BioMAX - essential tools in structural biology at MAX IV, Thomas Ursby (MAX IV)
10.30	Coffee break
11.00	*Theme 3: Material science*, chair Helmer Fjellvåg (University of Oslo) Neutron & Synchrotron Scattering for Fundamental Studies of Soft Materials, Reidar Lund (University of Oslo) Live imaging using high-energy electrons, Reine Wallenberg (Lund University)
12.30	Lunch
13.30	Buses depart from ELITE Hotel Ideon for visit tour of MAX IV including a look out at the ESS premises

MAX4ESSFUN annual meeting 2016
organising committee: Ulf Olsson (LU), Kajsa Paulsson (LU), Sine Larsen (UCPH), Jeppe Knudsen Baden (UCPH), Ellen Juel Nielsen (UCPH) and
scientific committee: Luise Theil Kuhn (DTU), Gregers Rom Andersen (AU) and Helmer Fjellvåg (OiU).

List of MAX4ESSFUN keywords

The Steering Committee of MAX4ESSFUN has decided on the list of keywords in the box below. The keywords are used to identify the researchers in the network when searches are made in the database of researchers http://max4essfun.ku.dk/database-of-researchers/. The keywords are also used to identify relevant university courses related to the use of neutrons and synchrotron light. All researchers in the MAX4ESSFUN network are asked to include the keywords relevant for their research in their university profiles.

Research areas	Techniques
Hard condensed matter science	Imaging
Applied material science	Small Angle Scattering
Engineering	Diffraction
Chemistry	X-ray Spectroscopy
Soft condensed matter science	Neutron Spectroscopy
Life sciences	Reflectometry
Structural biology	
Medicine	
Earth science	
Environment	
Cultural heritage	
Methods and instrumentation	
Magnetism	

Presented, revised and decided on Steering Committee meeting held April 11, 2016 at MAX IV.

Imaging

DTU Technical University of Denmark

DTU Compute
Institut for Matematik og Computer Science

A tomography approach to investigate the impactite formation processes

A. Fedrigo[1], C. Bender Koch[2], K. Marstal[1,3], M. Lyksborg[1], M. Strobl[4], C. Gundlach[5], and A. Bjorholm Dahl[1]

[1] DTU Compute, Lyngby (DK)
[2] Copenhagen University, Copenhagen (DK)
[3] Biomedical Imaging Group Rotterdam (NL)
[4] European Spallation Source ESS, Lund (SE)
[5] DTU Physics, Lyngby (DK)

*E-mail address: annfe@dtu.dk

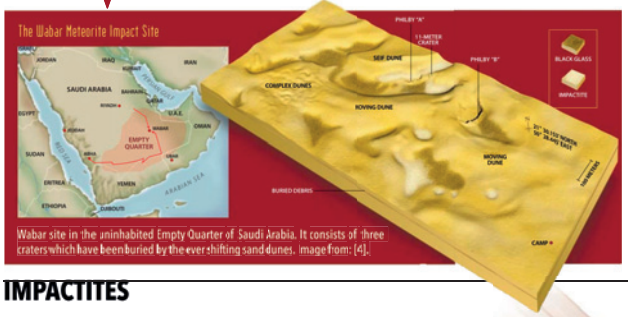

Wabar site in the uninhabited Empty Quarter of Saudi Arabia. It consists of three craters which have been buried by the ever-shifting sand dunes. Image from: [4].

Field samples of impactites from the Wabar meteorite impact site (Saudi Arabia) are investigated by applying X-ray and neutron tomography, in order to understand both the extent of impacts and the physical and chemical processes that occur during and following the impact.
Impact induced processes represent the most recently realised planetary surface creating processes and the least understood in details. In particular it is a challenge to identify material that has been subjected to temperature of several thousands of Kelvin and pressures of several GPa. Impacts area from iron meteorites show the presence of shock-induced microscopic rock deformations or iridium concentration anomalies [1, 2], but despite the strong correlation, these characteristics are not truly unique to meteoritic events. In order to univocally identify impacts of iron meteorites, two factors would co-occur [3]:

- a vesiculated partly melted sandstone (sedimentary), the impactite rock;
- Fe-Ni metallic micro-spheres of meteoric origin scattered in the impactite.

IMPACTITES

Impactites include Fe-Ni spheres (variable diameter ≃ 30-80 μm), which have been extracted by cutting the impactite and studied by scanning techniques. SEM analysis showed:

- the disappearance of the Widmanstätten structures (Ni-rich meteorites);
- the appearance of FeS (troilite) enriched regions on the surface of the spheres.

This suggest a full melting of the metal, followed by a density driven separation of the liquid immiscible troilite.

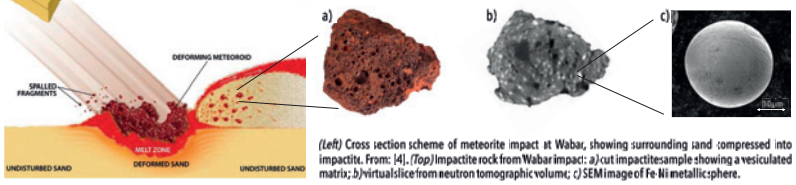

(Left) Cross section scheme of meteorite impact at Wabar, showing surrounding sand compressed into impactite. From: [4]. *(Top)* Impactite rock from Wabar impact: *a)* cut impactite sample showing a vesiculated matrix; *b)* virtual slice from neutron tomographic volume; *c)* SEM image of Fe-Ni metallic sphere.

IMAGING TECHNIQUES

Computed tomography is used as a non-destructive method of studying the morphology of the impactites and distribution and size variability of the metallic spheres. The combination of neutron and X-ray provides additional compositional information as the two probes have different attenuation coefficients with a non linear relation. Here are presented some of the results from a ~ 3 cm size impactite.

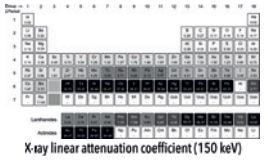

X-ray linear attenuation coefficient (150 keV)

X-RAY	vs	NEUTRON
Interactions with the electrons in the atomic shell		Interactions with the atomic nuclei
High spatial resolution		Lower spatial resolution
High sensitivity to heavy materials		Contrast between neighbouring atoms in the periodic table

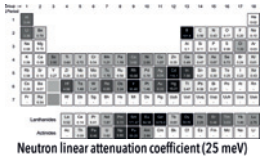

Neutron linear attenuation coefficient (25 meV)

X-RAY TOMOGRAPHY

X-ray CTs were carried out at the 3D Imaging Centre, DTU Lyngby (DK).

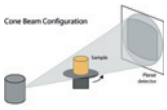

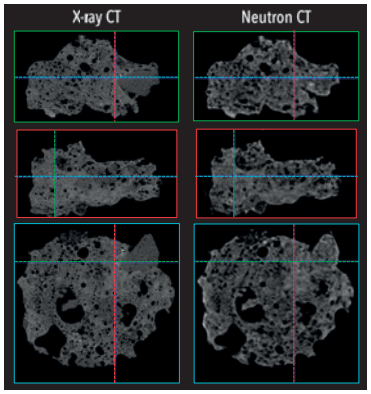

NEUTRON TOMOGRAPHY

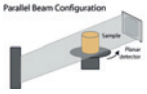

White beam neutron tomographies were carried out at the IMAGINE beamline [5], the cold neutron imaging facility at the Laboratoire Léon Brillouin CEA/CNRS (FR).

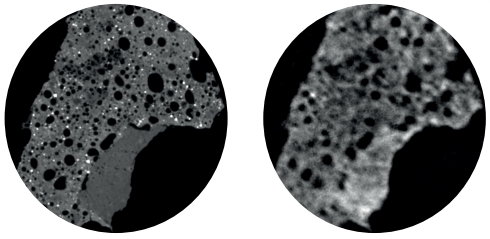

Close-ups of corresponding slices from a reconstructed impactite using (*left*) X-ray and (*right*) neutrons. X-ray imaging provides higher contrast for the metallic spheres, while neutrons highlights the inhomogeneous nature of the sandstone matrix.

IMAGE REGISTRATION

The two data sets have been registered (scaled and aligned on a common coordinate system) using the Statistical Parametric Mapping SPM8 software package [6], through a normalised mutual information coregistration [7].
This process allows for pixel-wise comparison between images from the two different data sets.

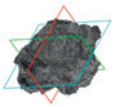

(*top*) 3D Volume rendering of the impactite, with orientation of the slicing planes. (*left*) Reconstruction of perpendicular sections from x-ray (left column) and neutron (right column) volumes.

FUTURE TASKS

- Apply registration to the remaining impactites
- Creation of bivariate histograms
- Segmentation following morphological features and the bivariate method
- Porosity evaluation

CONCLUSIONS

X-ray CT allowed us to obtain high resolution details on the morphology of the impactite, and on the distribution and size variability of the metallic spheres. Neutron imaging provided complementary information which will be used for improving the segmentation of the object.

REFERENCES
[1] Ebert M. *et al.*, *Meteorit. Planet. Sci.* **48**, 134-149 (2013).
[2] Hamann C. *et al.*, *Geochimica et Cosmochimica Acta* **121**, 291-310 (2013).
[3] French B.M. and Koeberl C., *Earth-Science Reviews* **98**, 123-170 (2010).
[4] Wynn J.C. and Shoemaker E.M., The Day the Sands Caught Fire, *Scientific American* **279**, 64-71 (1998).
[5] www-llb.cea.fr/fr-en/pdf/Imagine.pdf
[6] http://www.fil.ion.ucl.ac.uk/spm/software/spm8/
[7] Studholme C. *et al.*, *Pattern Recognition* **32**, 71-86 (1999).

ESS & MAX IV: Cross Border Science and Society
Interreg Öresund-Kattegat-Skagerrak European Regional Development Fund
EUROPEAN UNION
EUROPEAN SPALLATION SOURCE

FACULTY OF SCIENCE
UNIVERSITY OF COPENHAGEN

Interreg
Öresund-Kattegat-Skagerrak
European Regional Development Fund
EUROPEAN UNION
DTU

MICROSTRUCTURE AND MICROMECHANICS OF SEA URCHIN SHELLS FROM X-RAY TOMOGRAPHY

D. Müter[1], H. O. Sørensen[1], J. Oddershede[2], S. L. S. Stipp[1]

[1]Nano Science Center, Department of Chemistry, University of Copenhagen, Denmark
[2]Department of Physics, Technical University of Denmark, Kongens Lyngby, Denmark

Introduction

Biotemplating, i.e. copying nature's construction principles, has become a very successful approach for improving man made materials. Prominent examples include non-stick surfaces, exploiting the lotus leaf effect, or swim suits that imitate shark skin. Here, we demonstrate how nature optimizes the mechanical properties of biomineralised exoskeletons of marine organisms using the example of *Echinocardium cordatum* (Heart Urchin or Sea Potato).

Echinocardium cordatum

E. Cordatum is an irregular echinoid species, i.e. the test (shell) does not show the typical five-fold symmetry. It is cosmopolitan and lives buried in the sand on the middle to lower shore. It feeds on detritus via a channel connecting its burrow to the water column. The specimen in the photo (spines missing) is extremely light-weight: 2.5 g.

X-ray Tomography

- X-ray microtomography data were recorded on small fragments of the shells (tests) at the Imaging Industry Portal at DTU with a voxel size of about 1 µm
- Samples from three locations in Europe:
  - England (Irish Sea)
  - Scotland (North Sea)
  - Croatia (Adriatic Sea)

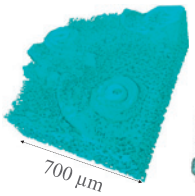

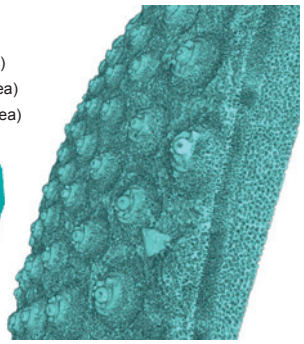

Micromechanics

- Subvolumes of the tomography data were segmented and subsequently surface and volume meshed
- Volume meshes were imported into finite element software, assigned material properties (calcite) and put under tensile load
- Ratio of strain to applied external load leads to Young's modulus

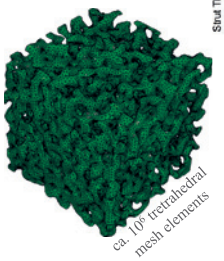

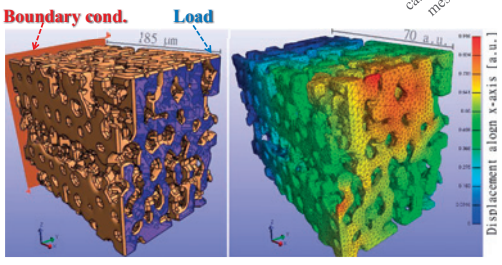

Microstructure

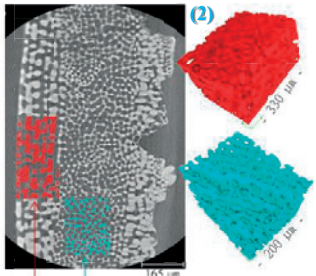

1) Microstructure of the shell consists of foam-like network of struts (stereom)
2) Two distinct regions can be observed forming a "sandwich"-structure
3) Within each of the regions the strut thickness is fairly constant although porosity varies widely
4) The density of strut connections is very high (human bone = 1/mm³) but sensible in relation to the size of the platelets (ossicles)

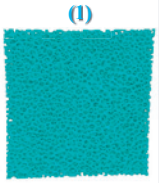

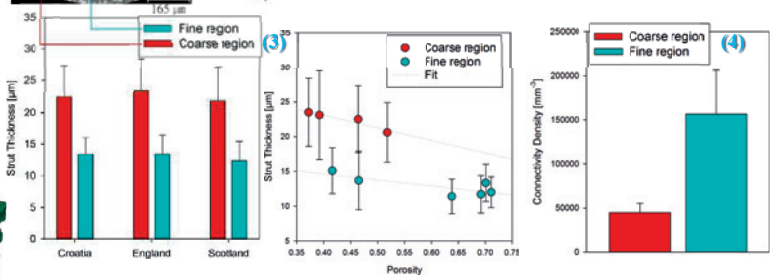

A. Spatial average of Young's modulus in dependence on porosity behaves like ideal open foam and performs by far better than a rock made from the same material

B. Local anisotropy in the mechanical properties correlates with functionalised regions

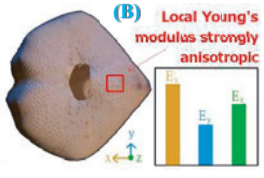

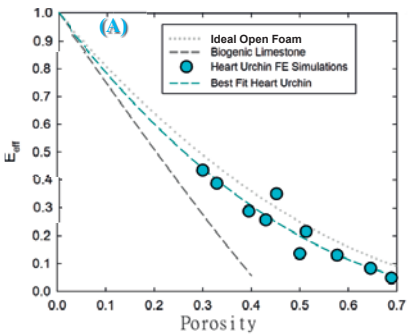

Conclusions

The intricate, highly porous microstructure of the heart urchin shell nicely illustrates how nature manages to provide the animal with an exoskeleton that withstands high pressure from both sand and water while preserving light weight and strength in the material. Despite its high porosity, the mechanical properties of the shell are consistent with the analytical expectation for the type of structure, i.e. foams. Local alterations show adaptions to the expected direction of load, e.g. around the mouth. However, the general design of a fenestrated structure, without long range order is maintained, possibly because fractures cannot easily penetrate the structure.

Acknowledgements

We thank the Imaging Industry Portal at DTU for providing access to the tomography facilities. D. M. is grateful for financial support through the EC FP7 Marie-Curie Project TOMOMECH and INTERREG.

Publication

D. Müter, H. O. Sørensen, J. Oddershede, K. N. Dalby, S. L. S. Stipp
Microstructure and Micromechanics of the Heart Urchin Test from X-ray tomography
Acta Biomaterialia 23 (2015) 21–26

The nucleation of rupture in rocks studied by 4D X-ray-imaging

François Renard, Benoit Cordonnier, Maya Kobchenko, and Dag Dysthe

Department of Geosciences, PGP, University of Oslo, Norway

Prior to failure, a transition from elastic to brittle behavior occurs in rocks through the development of microscopic damage that tends to localize, leading to shear localization. Here, we have imaged such damage using synchrotron time-lapse computed tomography and an X-ray transparent triaxial deformation rig. Centimeter-scale samples of sandstone, limestone, marble, and shale were axially loaded under compression, with a constant confining pressure in the range 5-30 MPa, at 20°C. For all samples, an elastic strain behavior is measured at low axial stress, followed by some inelastic deformations until the sample fails. The inelastic part corresponds to the development of damage (pore emanated cracks, pore collapse, mode I microcracks, wing cracks), and then a macroscopic shear fracture forms leading to failure. The initiation and mechanical interactions between these various modes of damage are observed to evolve in 3D with time and axial load, and depend on the initial amount of heterogeneities (i.e. pores) in the rock.

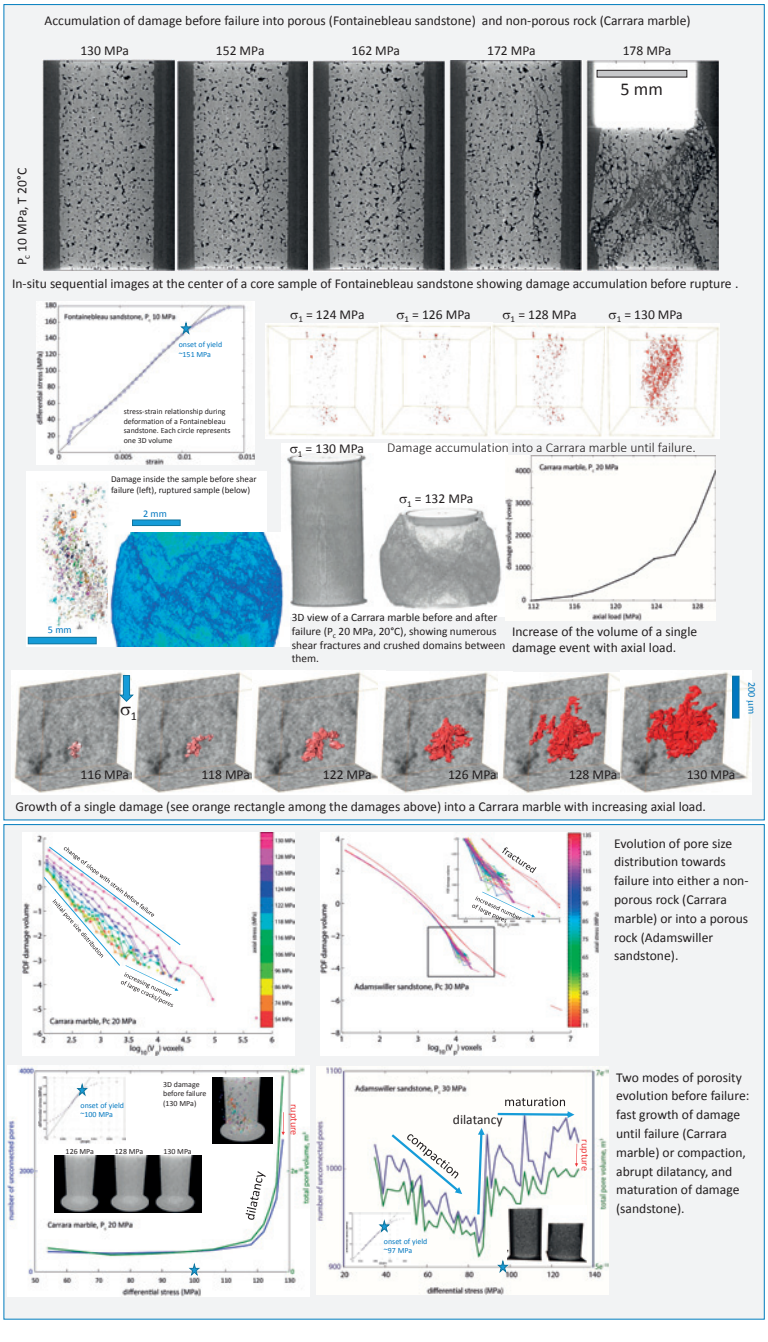

Evolution of pore size distribution towards failure into either a non-porous rock (Carrara marble) or into a porous rock (Adamswiller sandstone).

Two modes of porosity evolution before failure: fast growth of damage until failure (Carrara marble) or compaction, abrupt dilatancy, and maturation of damage (sandstone).

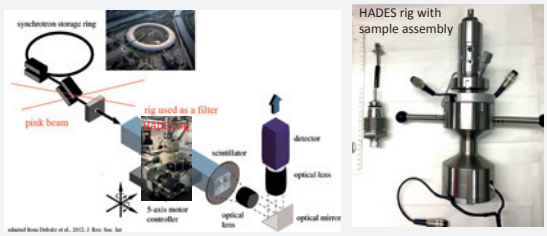

The HADES triaxial deformation rig is installed on beamline ID19 at the European Synchrotron Radiation Facility. The technical specifications are: 200 MPa axial load, 100 MPa confining load, 250°C, independent pore fluid pressure control. The rig is X-ray transparent and 3D tomography images can be acquired in situ at a voxel size in the range 2-6.5 micrometers (Renard et al., 2016).

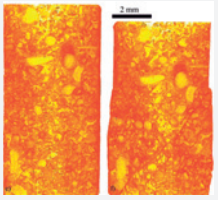

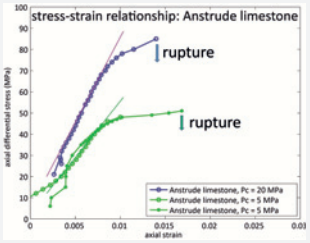

Limestone (Anstrude) imaged at 6.5 micron voxel size before and after shear rupture.

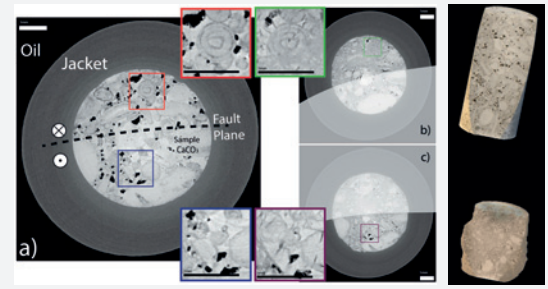

Intra-granular cracks, pore collapse, and development of a shear fracture into a limestone. a) 2D view in the middle of the sample before failure. b-c) after failure (development of a shear fracture). Insets show damage before and after failure. Right side: 3D views.

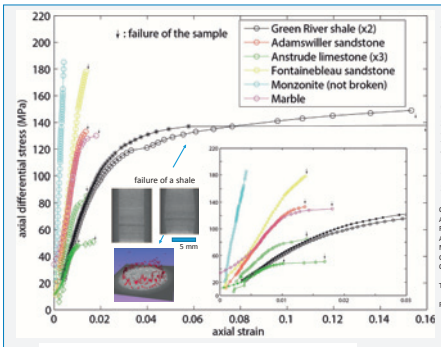

Stress-strain curves of in-situ deformation of different porous and non-porous rocks (5mm x 10 mm cylindrical cores). Each symbol indicates a 3D X-ray synchrotron tomography scan acquired with a voxel size of 6.5 micrometer.

Confining pressure:
Anstrude limestone: 5 or 20 MPa
Fontainebleau sandstone: 10 or 20 MPa
Adamswiller sandstone: 30 MPa
Monzonite: 20 MPa
Green River shale: 20 MPa
Carrara marble: 20 MPa

Temperature: 20 °C

Pore pressure: 1 MPa

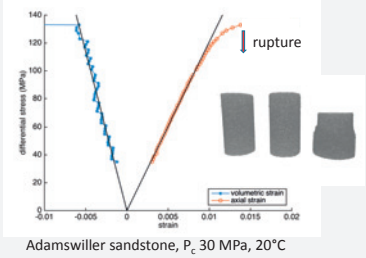

Stress-strain curves of in-situ deformation of a sandstone (Adamswiller) with axial and volumetric strains (small jumps are an artefact of the data processing).

Adamswiller sandstone, P_c 30 MPa, 20°C

Damage accumulation controls the nucleation of rupture in rocks. Time-lapse imaging at conditions relevant to earthquake nucleation was performed in deforming porous and non-porous rocks and show that 1) the damage maturation process before failure is different in porous and non-porous rocks; 2) pore size distribution evolves before failure and only the largest pores participate to damage in porous rocks; 3) microcracks parallel to the main compressive stress start developing in the elastic domain and the inelastic domain represents the onset of mode I crack linkage through shear cracks.

Renard, F., Cordonnier, B., Dysthe, D. K., Boller, E., Tafforeau, P. and Rack, A. (2016) A deformation rig for synchrotron microtomography studies of geomaterials under conditions down to 8 km depth in the Earth, Journal of Synchrotron Radiation, 23, 1030-1034.

Imaging (with) the last impression of an ancient eye

Gavin Taylor[1]*, Stephen Hall[2], Johan Gren[3] & Emily Baird[1]
[1]Department of Biology, [2]Division of Solid Mechanics, [3]Department of Geology - Lund University
*gavin.taylor@biol.lu.se

Eocene baltic amber from Blekinge

Tomography with XRADIA XRM520

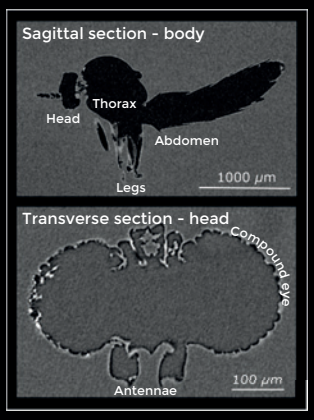

Fungus gnat/Soppmygg (Orfellini sp.)

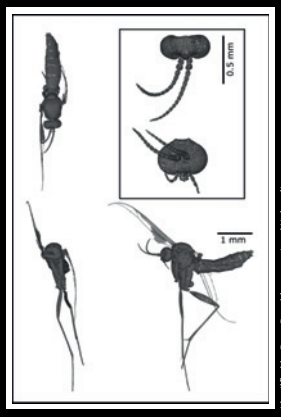

Identified by Rune Bygebjerg - Lund University
Jostein Kjærandsen - University of Tromsø

Segmented left compound eye
333 facets

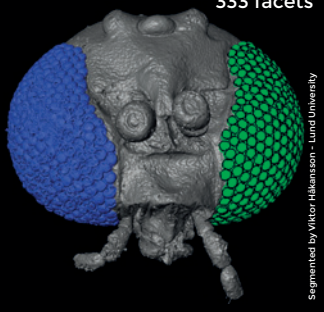

Segmented by Viktor Håkansson - Lund University

Optical axis of each facet

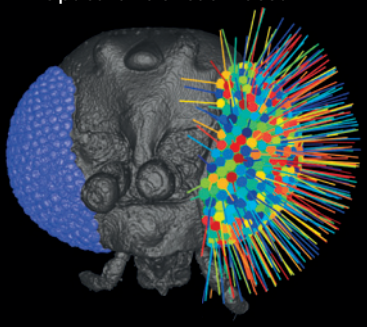

Field of view
for each eye

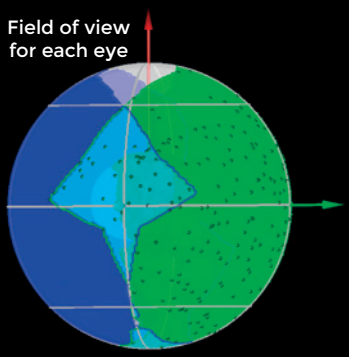

Sampling resolution
between facets

Mapped to eye

Mapped to
world

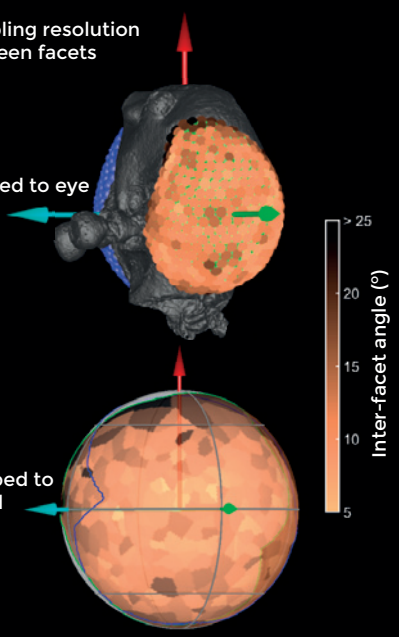

Optical axes projected onto spherical image

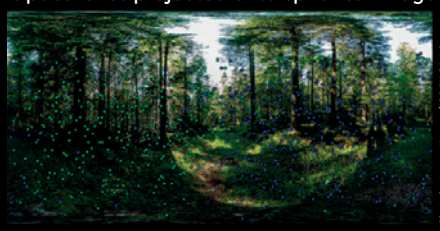

Photo by Ansgar Koreng / CC BY-SA 4.0
Wikicommons

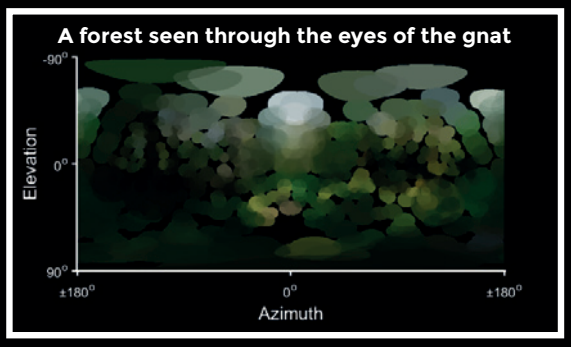

Interreg
Öresund-Kattegat-Skagerrak
European Regional Development Fund
EUROPEAN UNION
LUND UNIVERSITY

Resolution and contrast quantification of forward ptychography measurements in soft matter using thin film organic solar cells

Giovanni Fevola[1], **Gerardina Carbone**[2], **Jens Wenzel Andreasen**[1]

[1] Technical University of Denmark DTU, Department of Energy Conversion and Storage

[2] MAX IV Laboratory, NanoMAX beamline

Abstract

In this experiment we propose the acquisition of 2D ptychography projection images at the NanoMAX beam line at MAXIV of an organic tandem solar cell with a similar composition and structure to ones previously imaged at state of the art world leading beam lines. We foresee that the higher beam coherence at MAXIV will produce a better signal in materials with low electron density contrast such as the polymers and other organic materials used.

Introduction

Two-dimensional forward ptychography imaging can be used as a forward projection technique for high-resolution tomography enabling the study of the internal nano-structure of numerous engineering materials. The "quality" and accuracy of the tridimensional models is directly related to and limited by the ptychography image resolution and artefacts. We have previously imaged and characterized the inner structure of tandem solar cells [1], [2] by means of ptychographic tomography, but a lack in contrast between the constituents of the photoactive layers was always observed (view Figure 1 and Figure 2). This effect, along with noise or artefacts in the ptychography projection images, has prevented us to distinctively visualize and define the cell donor-acceptor domain structures.

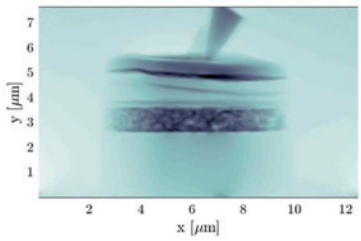

Figure 1. 2D Ptychographic projection image of a tandem solar cell. PSI 2014

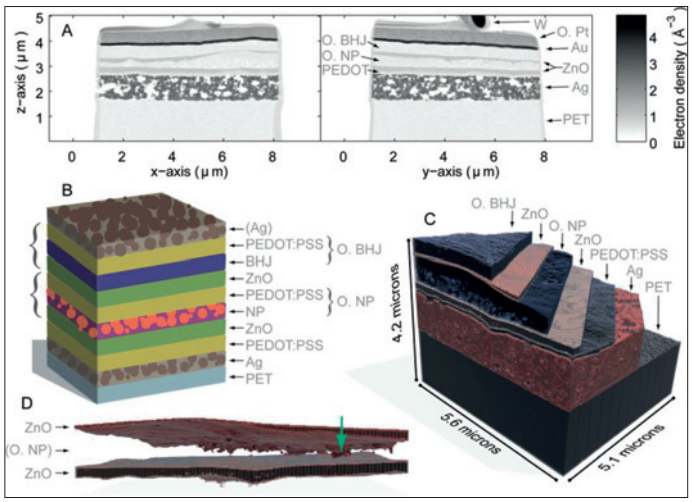

Figure 2. Ptychographic X-ray computed tomography of an organic tandem solar cell.
(A) Tomogram slices showing the electron density of the layers that make up the tandem solar cell. The device itself consists of PEDOT:PSS and a bulk heterojunction (O. BHJ), zinc oxide (ZnO), PEDOT:PSS and Landfester nanoparticles (O. NP), PEDOT:PSS (PEDOT) and silver nanoparticles (Ag) on PET foil (PET). (B) Schematic drawing of device layers. There are two active layers: a bulk heterojunction (BHJ) and a Landfester nanoparticle layer (NP). (C) Cutaway view of segmented layers annotated as in B. The active layer consisting of nanoparticles contains sub 20 nm pores whereas the bulk heterojunction is homogeneous. (D) Zinc oxide layers surrounding the nanoparticle layers. The vertical arrow marks a short circuit that penetrates through the porous nanoparticle layer [1].

Expected Outcome

The higher brilliance and coherence of the MAX-IV beam is expected to produce a superior image result for similar acquisition times. We foresee that a higher coherent flux will produce a better signal in materials with low electron density contrast such as between the polymers and other organic materials used. The different composition of the twelve layers that constitute a full organic tandem cell will allow a better comparison of the image improvement results for different materials.
If an image resolution increase is verified, especially for the photoactive layers materials, we would become more optimistic in achieving the goal of 10 nm resolution or better for a 3D tomogram in soft matter. Such resolution is for us required in order to **image the donor-acceptor domain structures** that are expected to be 10-20 nm in size.

Methodology

The measurements will be performed in air at 10 keV with similar exposure times and with similar full scan duration (relative to previous measurements). The reconstructed image quality will also be quantified using the Fourier ring correlation for the overall resolution estimation.
We will initially focus on single 2D ptychography projections, in order to benchmark the instrument and prepare for full tomographic reconstruction at a later stage.
The sample will be manufactured at DTU by the roll-to-roll process and prepared by focused ion beam (FIB) milling. The horizontal sample size is flexible and can be adjusted if required. Previous tested samples were scanned over a region of interest of 12 μm x 7 μm.

References

[1] E. B. L. Pedersen, D. Angmo, H. F. Dam, K. T. S. Thydén, T. R. Andersen, E. T. B. Skjønsfjell, F. C. Krebs, M. Holler, A. Diaz, D. W. Breiby, and J. W. Andreasen, "Improving organic tandem solar cells based on water-processed nanoparticles by quantitative 3D nanoimaging," *Nanoscale*, vol. 7, pp. 13765– 13774, 2015.

[2] H. F. Dam, T. R. Andersen, E. B. L. Pedersen, K. T. S. Thydén, M. Helgesen, J. E. Carlé, P. S. Jørgensen, J. Reinhardt, R. R. Søndergaard, M. Jørgensen, E. Bundgaard, F. C. Krebs, and J. W. Andreasen, "Enabling Flexible Polymer Tandem Solar Cells by 3D Ptychographic Imaging," *Adv. Energy Mater.*, vol. 5, no. 1, p. 1400736, Aug. 2015.

NANO-SCALE INFRARED IMAGING OF β-SHEET STRUCTURES IN SYNAPTIC JUNCTIONS OF PRIMARY NEURONS ISOLATED FROM TRANSGENIC MICE, MODELS OF ALZHEIMER´S DISEASE

O. Klementieva[1], J. Mathurin[2], A. Engdahl[3], R. Freitas[4], K. Willen[1], P. Uvdal[3, 5], L.M. Miller[6], G. Gouras[1]

[1] Department of Experimental Medical Science, Lund University, Lund, Sweden. [2] Laboratiore de Chimie Physique, Université Paris -Sud, Orsay, France.[3] MAX IV Laboratory, Lund University, Lund, Sweden.[4] Brazilian Synchrotron Light Laboratory, CNPEM, Campinas, Brasil. [5] Chemical Physics, Department of Chemistry, Lund University, Lund, Sweden. [6] National Syncalighrotron Light Source, Brookhaven National Laboratory, Upton, USA.

Contact: oxana.klementieva@med.lu.se

Amyloid β is a class of aggregation-prone proteins, which may misfold into stable, β-sheet rich fibrils. Amyloid β is linked to the development of synaptic pathology in Alzheimer's disease (AD). However, a main question in the AD field is how amyloid β contributes to AD neuropathology? Up to now there is little evidence for protein structural changes in diseased neuron. Our aim is to study the distribution of β-sheet structures in AD transgenic neurons in order to uncover sub-cellular mechanism(s) by which amyloid β-sheet structures are involved in AD pathology.

µFTIR

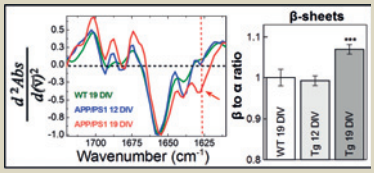

β-sheet aggregation in cultured AD transgenic primary neurons. Left panel: Averaged and normalized 2nd derivatives of FTIR spectra taken from APP/PS1 neurons at 12 and 19 days *in vitro* (DIV), and wild-type neurons at 19 DIV. Arrow indicates the β-sheet peak, which is evident only in APP/PS1 neurons at 19 DIV. Right panel: Statistical analysis of protein aggregation measured as the average of the protein aggregation ratios of 1628 cm^{-1} (β-structures) to 1656 cm^{-1} (α-structures) in AD transgenic and wild-type neurons as a function of time (days in culture).

AFM-IR

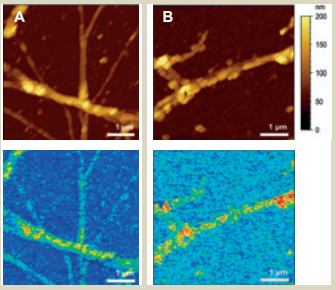

β-sheet aggregation in cultured AD transgenic primary neurons. (A): Wild type neurons, upper panel: AFM height; lower panel: infrared absorption at 1,635 cm^{-1} (β-sheet). (B) AD transgenic neurons, upper panel: AFM height; lower panel: infrared absorption at 1,635 cm^{-1}.

IR s-SNOM

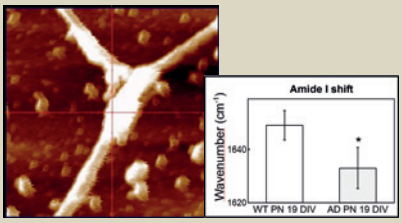

Protein misfolding in synaptic junctions of cultured AD transgenic primary neurons. Left panel: AFM image of synaptic junction in APP/PS1 neurons grown 19 days *in vitro* on AFM gold surface. Right panel: Statistical analysis of protein aggregation measured as a shift of Amide I in AD transgenic and wild-type neurons.

MATERIAL & METHODS:

To study β-sheet structures at sub-cellular level in AD neurons (APP/PS1 transgenic mouse) we used two AFM-based spectroscopic approaches AFM-IR and s-SNOM. Atomic force microscopy (AFM) provides information on the neuronal morphology while AFM-IR (atomic force microscopy infrared spectroscopy) and s-SNOM (near-field scanning optical microspectrosopy) characterise conformational changes in protein structures inside and on the surface of neurons correspondingly. Experiments were done at SOLEIL (France), Lawrence Berkeley National Laboratory (USA) and Brazilian Synchrotron Light Laboratory.

RESULTS:

Using synchrotron-based infrared micro-spectroscopy imaging (Maxlab, Lund, Sweden and NSLS, Brookhaven, USA) we have studied the secondary structure of proteins in cultured neurons at the micro level. The analysis of protein secondary structure showed a significantly higher ratio of β-sheet in AD transgenic cultured neurons expressing AD mutant APP compared to wild-type neurons, suggesting that the abnormal (β-sheet rich) protein structures occur within AD neurons. Here we show for the first time the infrared maps of β-sheet structures in AD transgenic neurons with nano-scale spatial resolution (~ 40 nm) using AFM-IR. We also demonstrate that IR s-SNOM can be used to study secondary structures of proteins in neurons.

CONCLUSIONS:

Our results show that β-sheet structures are distributed AD neurites of AD transgenic compared to wild-type neurons. The presence of β-sheet structures in synaptic junctions in AD transgenic neurons supports the conclusion that synapses are the sites where Aβ accumulates and aggregates, thereby mediating synapse dysfunction in AD brain. However, further experiments are required to understand the spread of β-sheet structures, and nano-scale AFM-based infrared spectroscopies are useful tools for this purpose.

ACKNOWLEDGEMENTS:

Structural Biology

Crosslinking mass spectrometry to explore interactions of sHsp chaperones with client proteins

Cecilia Emanuelsson[1], Gudrun Rutsdottir[1], Johan Härmark[2], Hans Hebert[2], Morten Ib Rasmussen[3], Peter Højrup[3], Philip J. B. Koeck[2], Katja Bernfur[1], Christopher A. G. Söderberg[4]

[1]Department of Biochemistry and Structural biology, Lund University, [2]School of Technology and Health, KTH Royal Institute of Technology and Department of Biosciences and Nutrition, Karolinska Institutet, Stockholm, [3]Department of Biochemistry and Molecular Biology, University of Southern Denmark,[4]Max IV Laboratory, Lund University.

1. Introduction

Small heat shock proteins (sHsps) form a first defence line against cell stress, since they can immediately respond to partially unfolded client proteins that are rescued from aggregation through kinetic competition between on one hand aggregation and on the other hand sHsp interaction. Yet the mechanism of sHsp-client recognition remains poorly understood. We address the questions: what parts of sHsps interact with client proteins? What parts of partially unfolded client proteins interact with sHsps? The transient nature of the interactions that prevent client protein aggregation rationalize to probe this interaction by crosslinking mass spectrometry (CXMS). We currently use a workflow with lysine-specific crosslinking and nanoLC-MSMS to explore the interaction between Hsp21 and two model client proteins, malate dehydrogenase and citrate synthase, both of which are thermosensitive. The identified crosslinks point at an interaction between the disordered N-terminal region of Hsp21 and presumably unfolding parts of the client proteins.

Conclusions

- Crosslinking mass spectrometry (CXMS) is used to evaluate interactions between Hsp21 and model client proteins
- The identified crosslinks point at an interaction between the disordered N-terminal region in Hsp21 and in the thermosensitive client protein the parts which presumably unfold first upon exposure to moderately increased temperature.

Schematical outline of CXMS to explore protein-protein interactions

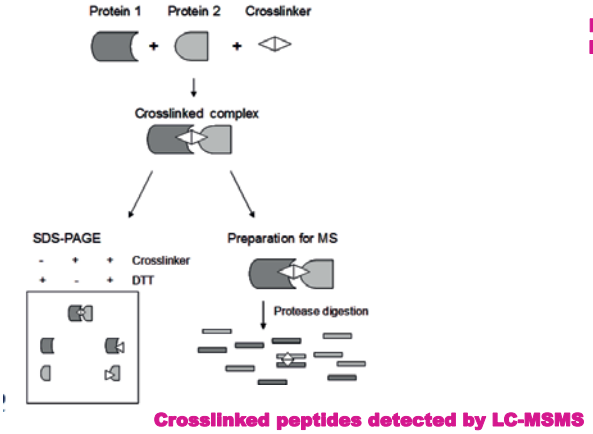

Crosslinked peptides detected by LC-MSMS

LC-MSMS processed to detect crosslinks using MassAI software http://www.massai.dk/

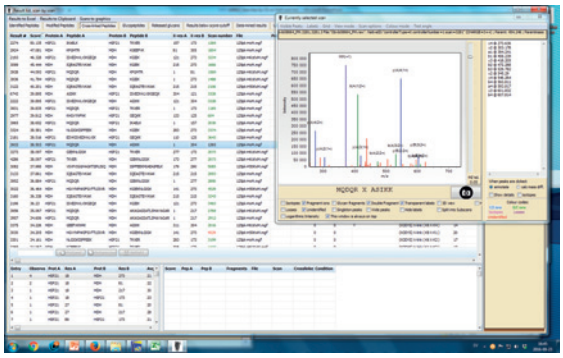

A structural model of the Hsp21 dodecamer based on cryo-EM and SAXS

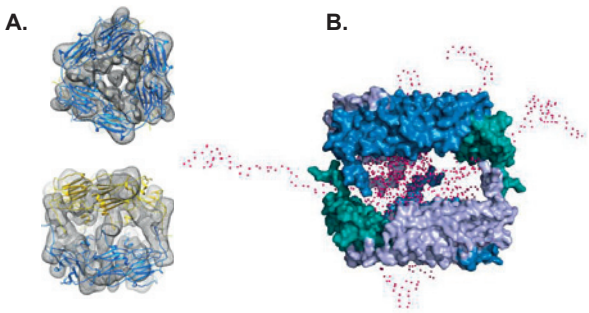

A. Structural model of the Hsp21 dodecamer obtained by homology modelling and cryo-EM. The Hsp21 dodecamer is comprised of two trimer-of-dimer hexameric discs (yellow, blue), here shown fitted into the cryo-EM density map (grey). The views are along the 3-fold axis (upper) and the 2-fold axis (lower).

B. Dynamic view of the Hsp21 dodecamer obtained by SAXS and EOM simulation. The N-terminal region is disordered and here visible as highly mobile and flexible N-terminal arms able to immediately catch and interact with unfolding client proteins.

Crosslinked lysine residues in Hsp21 and MDH

Hsp21 dimer

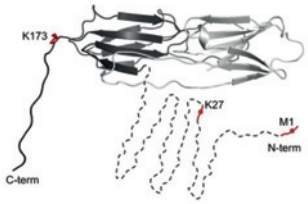

MDH dimer

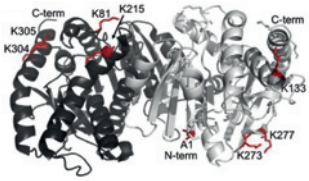

Residues involved in Hsp21-MDH crosslinks visualized in the 3D structures.

Location of the residues M1, K27, and K173, crosslinked to MDH, shown in one of the monomers in a Hsp21 dimer subunit of the Hsp21 dodecamer. Residues M1 and K27 are within a predicted disordered N-terminal region (residues 1–84, dashed).

Location of the residues crosslinked to Hsp21 shown in the MDH dimer (PDB ID 1MLD); one monomer is colored dark gray, the other light gray and residues crosslinked to Hsp21 shown as sticks. For clarity, the crosslinked residues 81, 215, 304, and 305 are only labelled in the dark gray monomer, and residues 1, 133, 273, and 277 are only labelled in the light gray monomer.

Cecilia Emanuelsson, Department of Biochemistry and Structural Biology, Center for Molecular Protein Science, Lund University, Gudrun.Rutsdottir@biochemistry.lu.se

Production optimization of human AQP10 for structural determination

Florian Schmitz, Rebecka Andersson, Jennie Sjöhamn, Richard Neutze and Kristina Hedfalk

From the Department of Chemistry/Biochemistry, University of Gothenburg, P.O. Box 462, SE-405 30 Göteborg, Sweden

Interreg Öresund-Kattegat-Skagerrak European Regional Development Fund

EUROPEAN UNION

UNIVERSITY OF GOTHENBURG

Introduction

- Human aquaporin 10 (hAQP10) is an integral membrane protein, located in the intestinal cells
- There is a lack of structural information on this aquaglyceroporin
- To increase chances for crystallization, a non-glycosylated hAQP10 mutant was created: N133Q
- Because of decreased thermostability, a more stable triple mutant (2-5 °C), named PE33, has been generated by random mutagenesis
- Purification with DDM as detergent
- Usage of LCP as crystallization method
- We aim for the first high resolution structure of a human aquaglyceroporin

General strategy

hAQP10

↓ deglycosylation

decreased thermostability → hAQP10 N133Q

↓ 3x mutant

increased thermostability → hAQP10 PE33

- Crystallization: LCP/Vapor diffusion
- Biochemical characterization: CETSA, Stopped Flow, ITC…

hAQP10 PE33 purification

Fermentor *pichia pastoris*

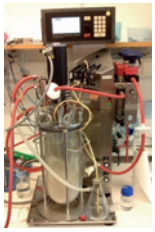

Yield: 120 g/L culture

Membrane preparation

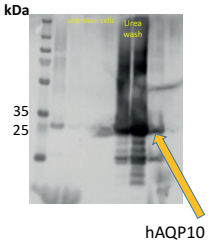

7,5 g membranes from 65 g of cells

Protein purification

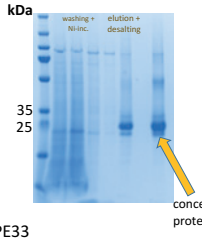

1,2 mg/L hAQ10 PE33

SEC

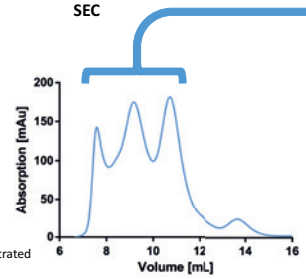

SEC SDS-gel

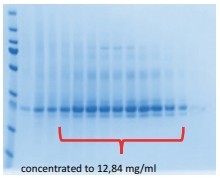

Crystallization

non-glycolysed, less thermostable hAQP10 mutant N133Q → purification with short-chain detergent OG → weak thermal stability, only small crystals by vapor diffusion. Precipitation problems!

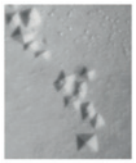

non-glycolysed, thermostable hAQP10 mutant PE33 → purification with long-chain detergent DDM

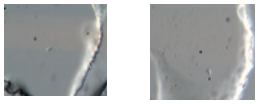

initial crystals obtained by LCP screening. Higher thermostability supports crystal development

Future plans

- purification optimization
- crystal optimization
- vapor diffusion with DDM purified mutants
- LCP for deglycolysed mutant
- screening for more mutants

References: Öberg F., 2011, Glycosylation Increases the Thermostability of Human Aquaporin 10 Protein, J Biol Chem.

Crosslinking mass spectrometry for measurement of subunit exchange in oligomeric proteins

Gudrun Rutsdottir[1], Johan Härmark[2], Yoran Weide[1], Hans Hebert[2], Morten Ib Rasmussen[3], Peter Højrup[3], Philip J. B. Koeck[2], Christopher A. G. Söderberg[4], Katja Bernfur[1] and Cecilia Emanuelsson[1]

[1]Department of Biochemistry and Structural biology, Lund University, [2]School of Technology and Health, KTH Royal Institute of Technology and Department of Biosciences and Nutrition, Karolinska Institutet, Stockholm, [3]Department of Biochemistry and Molecular Biology, University of Southern Denmark,[4]Max IV Laboratory, Lund University.

Introduction

Small heat shock proteins (sHsps) form a first defence line against cell stress, and are especially abundant in plants. The structure has been resolved to atomic resolution for only a few sHsps including a cytosolic plant protein, Hsp16.9. Crystallization is hampered by the flexible N-terminal arms, not fully visible in any of the crystal structures. Hsp21 is a chloroplast-localized sHsp crucial for stress resistance in *Arabidopsis thaliana* plants. Compared to the cytosolic Hsp16.9 it has even longer N-terminals arms with a functionally important and conserved methionine-rich motif. In this work we use crosslinking mass spectrometry (CXMS) combined with homology modelling, cryo-EM, and small angle X-ray scattering (SAXS) to gain structural information. By using CXMS on a mixture of non-labeled and ^{15}N-labeled Hsp21 we can distinguish between inter- and intra-monomeric crosslinks and measure the dynamic subunit exchange.

Conclusions

- CXMS is used to evaluate subunit exchange in Hsp21 dodecamer
- With mixed isotope crosslinking inter- and intramonomeric crosslinks can be distinguished by detection of hybrid crosslinks
- In a proposed new structure model of the Hsp21 dodecamer, the C-terminal tails appear to interact pairwisely between the discs
- Moreover, six of the 12 N-terminal arms are located between the two discs and six appear as flexible arm on the dodecamer outside

Is the crosslink inter- or intramonomeric?

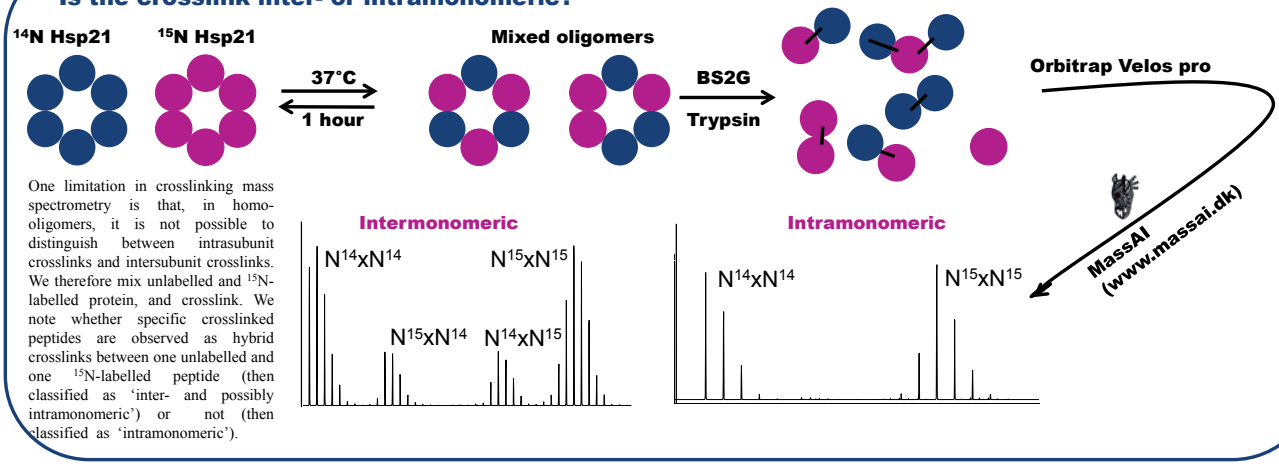

One limitation in crosslinking mass spectrometry is that, in homo-oligomers, it is not possible to distinguish between intrasubunit crosslinks and intersubunit crosslinks. We therefore mix unlabelled and ^{15}N-labelled protein, and crosslink. We note whether specific crosslinked peptides are observed as hybrid crosslinks between one unlabelled and one ^{15}N-labelled peptide (then classified as 'inter- and possibly intramonomeric') or not (then classified as 'intramonomeric').

A new structural model of the Hsp21 dodecamer obtained by cryo-EM and homology modelling

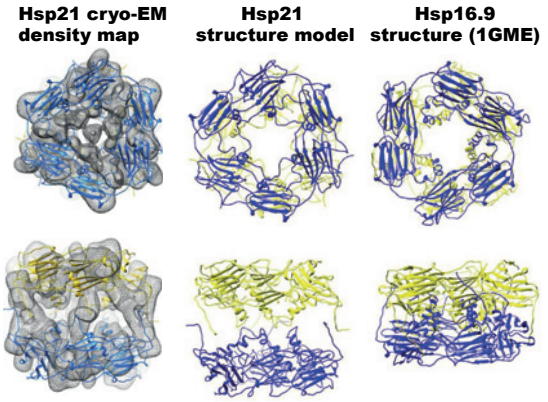

Left: The Hsp21 cryo-EM density map, into which the Hsp21 homology model is fitted, shown with partially transparent mesh surface representation at contour level 1.11. The views are along the 3-fold axis (upper) and the 2-fold axis (lower). The two discs of the Hsp21 model (in yellow and blue) were fitted separately to the map using the Fit in Map feature in Chimera. **Middle and right:** Comparing the structure model of Hsp21 (middle) with the crystal structure of Hsp16.9 (right) used as template for homology modelling, with the two hexameric discs in yellow and blue. Top views (upper) shows a relative rotation of the discs around the 3-fold axis of approximately 30° in Hsp21 compared to Hsp16.9. Side views (lower) demonstrate that the distance between the discs is extended in Hsp21. These differences in the Hsp21 model compared to Hsp16.9 template can also be described as an imaginary screw movement along the 3-fold axis.

N-terminal flexible arms appear on the dodecamer outside by SAXS-data and EOM simulation

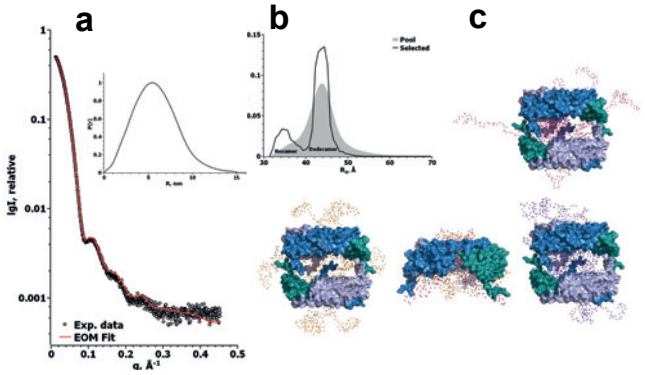

(a) Hsp21 wildtype SAXS data (circles) and the corresponding EOM fit (red line) using hexamers and dodecamers. The inset shows the Hsp21 wildtype distance distribution function calculated from the experimental SAXS data using GNOM. (b) R_g distribution for the random pool of 10 000 hexamers and 5 000 dodecamers which was used to fit the SAXS data in panel (a) is shown in the grey area. The black line shows the R_g distribution of the optimized ensemble fitting our Hsp21 wildtype SAXS data. While the selected hexamer distribution was overall compact, the selected dodecamer distribution was found at the center of the random pool. (c) Representative models from the selected pools of the hexamer and dodecamer, created by EOM. The rigid core is shown in a surface representation, where the three dimers of each disc are colored in blue, light blue and teal, respectively and the modeled flexible parts are shown as spheres.

Gudrun Rutsdottir, Department of Biochemistry and Structural Biology, Center for Molecular Protein Science, Lund University, Gudrun.Rutsdottir@biochemistry.lu.se

Trapped in the crystal: Using TrpR crystals to order proteins in a lattice

Janina Sprenger,[1] Jannette Carey,[2] Johan Unge,[3] Marjolein Thunnissen[3] & Sara Linse[1]

[1]Center for Molecular Protein Science, Lund University, SE-221 00 Lund, Sweden; [2]Chemistry Department, Princeton University, Princeton, New Jersey, 08544 USA; [3]MAX IV Laboratory, Lund University, SE-22100 Lund, Sweden

Why do we do this?

X-ray crystallography is one of the most used methods to obtain high resolution structures of proteins. Some proteins, however, do not crystallize and their structure can not be solved using this method. To overcome that limitation, we are developing an alternative crystallography-based method to obtain structural information of proteins by bringing them into solvent channels of an already existing crystal.

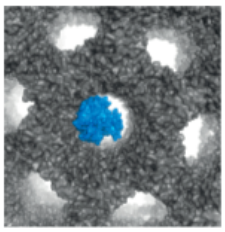

Figure 1 Solvent channels within a crystal (PDB: 1MI7, grey surface) with carbonic anhydrase (~ 30 kDa) pictured in a channel

Why do we use TrpR?

The crystal structure of tryptophan repressor protein from *E.coli* (TrpR) has been solved to 2.5 Å in spacegroup P6122 [1]. In the crystal, TrpR adopts a domain swapped conformation with large solvent channels of 60–70 Å diameter, big enough to host small proteins or biomolecules.

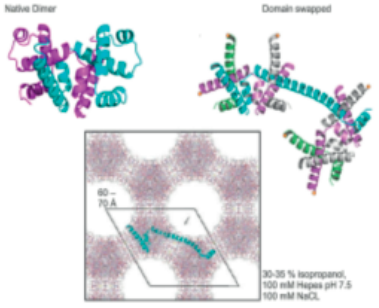

Figure 2 Packing of TrpR in the crystal, adapted from [1]

How do we get proteins in the channels?

We can simply soak the proteins of interest into the channels. Addition of lyophilized powder of cytochrome C results in slowly stained TrpR crystals. This works for proteins that can be lyophilized and do not aggregate in the crystal condition. We successfully soaked cytochrome C, calmodulin, ovalbumin and calbindin-d28k (CB).

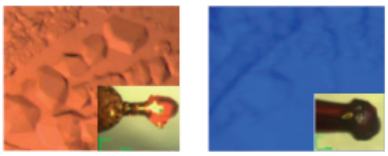

Figure 3 TrpR crystals with soaked cytochrome C (left) in the drop and in the litho.loop. Same for the figure at the right but using Alexa red- labeled calmodulin

How can we 'order' the soaked proteins?

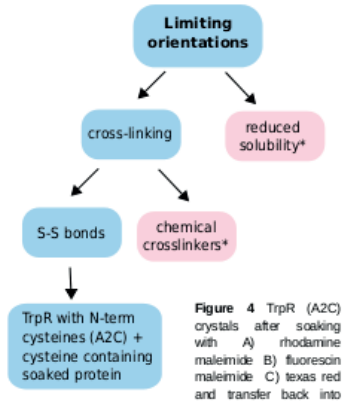

Figure 4 TrpR (A2C) crystals after soaking with A) rhodamine maleimide B) fluorescin maleimide C) texas red and transfer back into reservoir

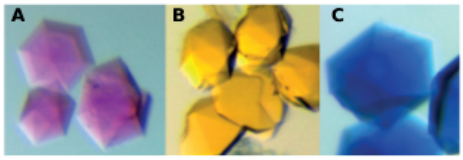

*planned work in pink boxes

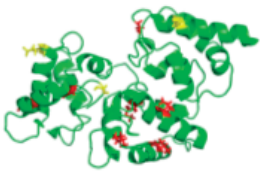

Figure 5 up: NMR structure of CB (PDB: 2G9B; green ribbon) with cysteine residues as red or yellow sticks. right: SDS-PAGE for CB (C126 mutant) and TrpR crystals soaked with the same CB construct.

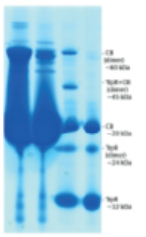

How do we solve the structures of the soaked proteins?

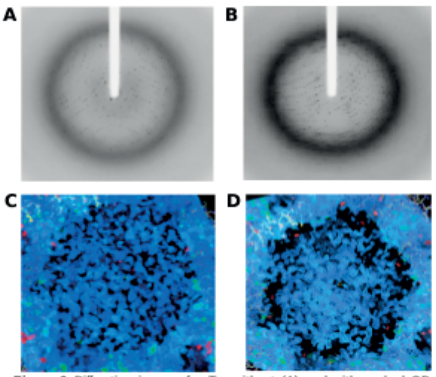

Figure 6 Diffraction images for Trp without (A) and with soaked CB cystein mutant (B). 2Fo-Fc electron density map (0.5 I/sigma) for TrpR channels without soaked protein (C) and with a CB mutant (C164, D)

We have collected several X-ray diffraction datasets (Figure 6) of TrpR with soaked proteins and are solving the structures using

1. **Molecular replacement (MR)**: TrpR structure itself can be solved but for the soaked proteins only differences in the channel electron density are visible (Figure 6).
2. **Single wavelength anomalous dispersion (SAD):** For datasets using Lanthanum containing CB the anormalous signal may be present, but is too low to find a structure solution (Figure 7).
3. **Maximum enthropy method (MEM)** [2]: Several datasets are currently tested with MEM by Prof. Takata's group (Spring-8, Japan) to obtain structural information of the soaked proteins.

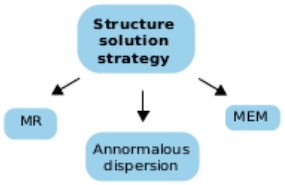

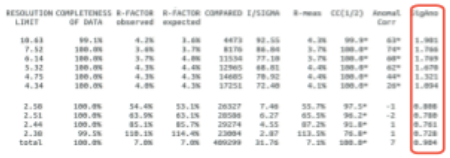

Figure 7 XDS processing, CORRECTLP output for 4000 frames (0.1° rotation) for La2+ containing CB (C25?? mutant). Spacegroup P6122 with cell dimensions a,b= 86.05; c=113.54; α,β= 90° γ=120°. Collected at DESY, Hamburg station P14, λ=1.971Å

What are the next steps?

That we cannot solve the structure of the soaked protein yet may have two main reasons: ***1. Low occupancy*** and ***2. Lack of order*** of the protein in the channels. Therefore we need to test the occupancy and order of the soaked molecules with other methods like ***MS*** and ***cryo-EM.*** Furthermore, we need to explore if other techniques like ***neutron diffraction/scattering*** are applicable to this crystal system.

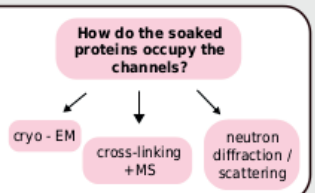

References

[1] Lawson CL, Benoff B, Berger T, Berman HM, Carey J. E. coli trp repressor forms a domain-swapped array in aqueous alcohol. Structure 2004; 12:1099

[2] Fujita D, Suzuki K, Sato S, Yagi-Utsumi M, Yamaguchi Y, Mizuno N, Kumasaka T, Takata M, Noda M, Uchiyama S, Kato K, Fujita M. Protein encapsulation with synthetic molecular hosts. Nature Communication 2012, 3, 1093

Contact: Janina.Sprenger@biochemistry.lu.se

ESS & MAX IV: Cross Border Science and Society

Interreg Öresund-Kattegat-Skagerrak European Regional Development Fund

EUROPEAN UNION

THE IMPACT OF PROTEIN-WATER INTERACTIONS ON THE STRUCTURAL PROPERTIES OF IDPs

J. HENRIQUES, L. ARLETH, K. LINDORFF-LARSEN & M. SKEPÖ

joao.henriques@teokem.lu.se

Interreg Öresund-Kattegat-Skagerrak European Regional Development Fund | EUROPEAN UNION | ESS & MAX IV: Cross Border Science and Society | LUND UNIVERSITY | UNIVERSITY OF COPENHAGEN

- Molecular dynamics simulations of Histatin 5 (24 aa IDP, FCR = 0.4, NCPR = 0.2) show that by using the popular TIP3P water model one obtains overly collapsed conformational ensembles [1, 2]. The same conclusion is drawn by other groups using different IDP models [3 - 6].
- Experimental SAXS measurements [7] show that Histatin 5 radius or gyration (Rg) is ≈ 1.38 nm. With TIP3P, $< Rg >_{sim}$ = 0.998 nm.
- Protein-water dispersion interactions are thought to be too weak, leading to water being a poor solvent. The resulting hydrophobic effect went unnoticed for years, due to the main focus of the community on folded proteins, for which it has a desirable, stabilizing effect.
- The dispersion corrected TIP4P-D and TIP4P/2005s water models have been proposed for IDPs [3, 4] (although advertised as having general application). When applied to Histatin 5, one obtains much better correspondence with experimental evidence. $< Rg >_{sim}$ = 1.372 and 1.295 nm for TIP4P-D and TIP4P/2005s, respectively (recall that Rg_{exp} ≈ 1.38 nm).
- Principal component analysis suggests that the two enhanced water models produce similar conformational ensembles, despite their different underlying differences. With TIP3P, one samples a clearly different region of phase space.
- Evaluation of the solution scattering from the simulations (using CRYSOL) shows that the contrast of hydration shell (ρ) is a critical parameter, and the default value (ρ = 0.03 e/Å^3, as commonly used for folded proteins) does not apply to Histatin 5.
- The use of a parameter-free approach (WAXSiS) [8] appears to indicate that ρ is lower for Histatin 5.

- **ARE THE TWO PREVIOUS POINTS REPRODUCIBLE FOR OTHER IDPS?**
- **HOW DIFFERENTLY DOES WATER SOLVATE FOLDED PROTEINS AND IDPS?**
- **IF THERE IS ONLY ONE "WATER MODEL" IN NATURE, WHY IS THE SAME APPARENTLY NOT POSSIBLE FOR COMPUTER SIMULATIONS?**

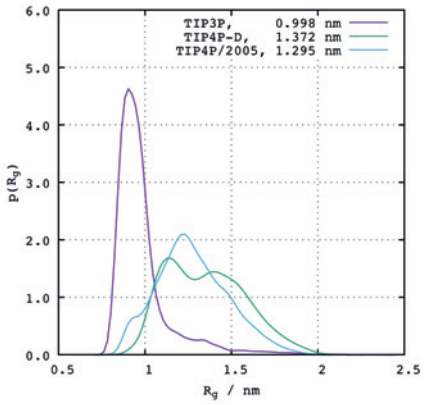

Figure 1 – Density estimates of the radius of gyration (Rg) for the three water models tested here. Values presented in the legend are relative to the computed average radii, < Rg >.

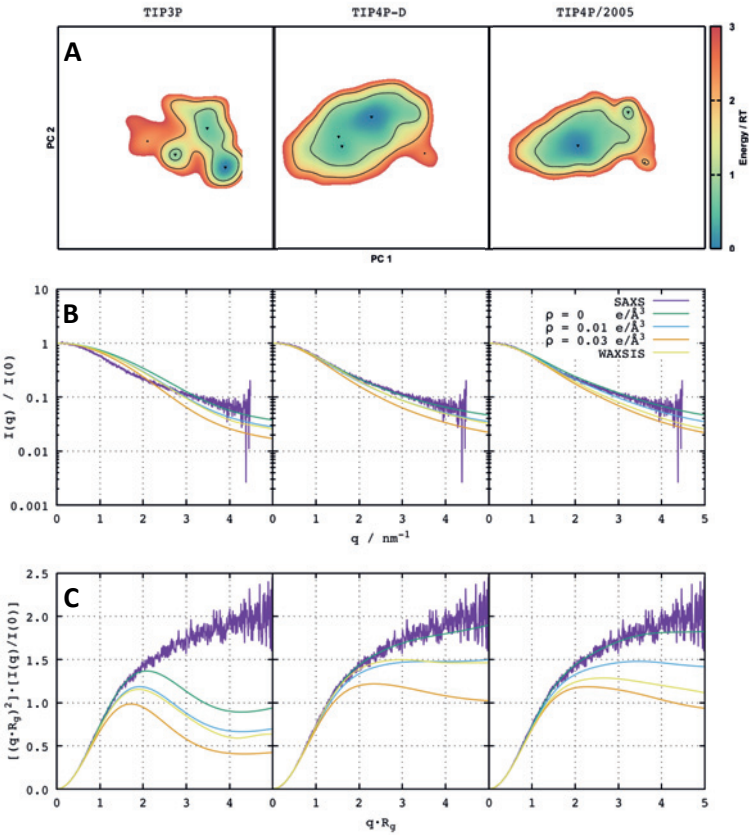

Figure 2 – **(A)** Principal component analysis for each water model simulation. Only the first two principal components are included. **(B)** Small-angle X-ray (SAXS) form factors and **(C)** corresponding Kratky plots, obtained from experiment and simulations. Color keys: **Experimental**, WAXSiS, and CRYSOL (with different ρ values).

[1] Henriques (2015) 10.1021/ct501178z
[2] Henriques (2016) 10.1021/acs.jctc.6b00429
[3] Piana (2016) 10.1021/jp508971m
[4] Best (2014) 10.1021/ct500569b
[5] Rauscher (2015) 10.1021/acs.jctc.5b00736
[6] Mercadante (2015) 10.1021/acs.jpcb.5b03440
[7] Cragnell (2016) 10.1002/prot.25025
[8] Knight (2015) 10.1093/nar/gkv309

LUNARC | SNIC

Neutron studies of new drug leads for the inhibition of cancer-related human carbonic anhydrase IX

Katarina Koruza[1*], Brian Mahon[3], Cynthia Okoh[3], Robert McKenna[3], Zoë Fisher[2*], Wolfgang Knecht[1*]

[1]Biology Department & Lund Protein Production Platform, Lund University, Sweden; [2]Scientific Activities Division, European Spallation Source, Lund, Sweden; [3]Department of Biochemistry and Molecular Biology, University of Florida, Gainesville FL, USA. (*Supported by Interreg)

BACKGROUND

There are 15 expressed carbonic anhydrases in humans. They support a vast array of physiological reactions, from general acid/base homeostasis to bone remodeling and gluconeogenesis. The expression of one of these isoforms, Human carbonic anhydrase IX (HCA IX, Fig.1), is mostly limited to cancer cells in many kinds of solid tumors. Its expression is controlled by hypoxic conditions and it is seen as an important mechanism for the promotion of cancer metastasis. it has also been observed that the presence of HCA IX in cancer cells strongly correlates poor cancer patient prognosis, making HCA IX an interesting therapeutic target.

Efforts to develop specific inhibitors for HCA IX are complicated by the presence of the 14 other HCA isoforms. This family of enzymes share a similar fold and have high sequence identity. Existing drugs bind to many other HCAs, causing low efficacy and side effects. It has been well established that ligand (inhibitor) binding to a target protein is mediated through numerous interactions that may include: H-bonding directly and/or through intervening waters, electrostatic interactions with charged or polar amino acid side chains, metal coordination, energetic changes through water displacement, aromatic stacking, or other hydrophobic interactions.

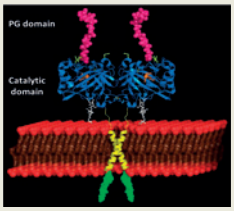

Fig.1. Model of human carbonic anhydrase II as a dimeric membrane protein. From: Alterio et al. (2009) PNAS 106 (38), p.16233.

Our goal is to apply neutron crystallography to the HCA IX system in order to obtain more information on drug binding interactions.

Saccharin was recently identified as a promising inhibitor in that it demonstrates some HCA IX specificity compared to widespread HCA II (Ki of 0.1 μM vs. 5.9 μM). Comparing neutron crystal structures of apo and inhibitor-bound HCA IX provides a unique opportunity to directly investigate how saccharin binds through H-bonding, the role of water displacement, and can give clues as to how the making/breaking of H-bonds modulates binding and isoform specificity. Ultimately we aim to enable isoform-specific drug development against HCA IX for cancer diagnosis, disease staging, imaging, and possibly therapy.

METHODS

Neutrons required large single crystals in the ~1 mm^3 range, making it unfeasible to work with native HCA IX (Fig. 1). As such we constructed soluble HCA IX mimic, using HCA II as a scaffold and introducing 7 mutations to precisely reconstruct the HCA IX active site.

The HCA IX mimic was expressed as recombinant protein in BL21(DE3) *E.coli* cells and purified with a two-step process that involves affinity chromatography and gel filtration (Fig. 2). Crystals of HCA IX were formed in sitting-drops with 1.2 M sodium citrate, 50 mM Tris pH 8.5. Large single crystals were mounted in quartz capillaries and subjected to vapor H/D exchange prior to neutron and X-ray data collection.

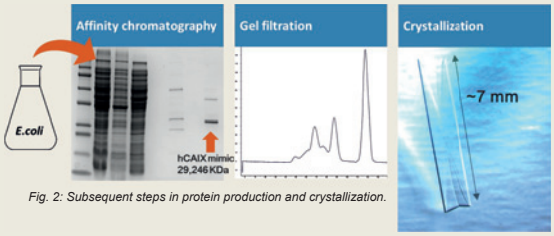

Fig. 2: Subsequent steps in protein production and crystallization.

RESULTS

The X-ray crystal structure refinement for each crystal type were completed first, followed by joint refinement in Phenix against both X-ray and neutron data sets.

Data collection and processing	Apo – X ray	Apo - Neutrons	Sac – X ray	Sac - Neutrons
Diffraction source	Beamline I911-2, Max lab	ILL, Grenoble	Beamline I911-3, Max lab	FRM-II nuclear research reactor
Wavelength (Å)	1.04	3.0-3.98	1.00	2.67
Temperature (K)	293	293	293	293
Detector	165 mm MAR Mosaic CCD	Cylindrical neutron image-plate detector	165 mm MAR Mosaic CCD	Cylindrical neutron image-plate detector
Rotation range per image (°)	1°	/	0.5°	/
Total number of images	135	28	140	284
Exposure time per image	30 sec	5.8 h	30 sec	45 min
Space group	4, P2 (1)	4, P2 (1)	4, P2 (1)	4, P2 (1)
Unit-cell parameters (Å, °)	a = 42.50, b = 41.80, c = 72.90 α = 90.0 β = 104.1 γ = 90	a = 41.78, b = 41.00, c = 71.71 α = 90.0 β = 104.06 γ = 90.0	a = 42.5, b = 41.8, c = 72.7 α = 90.0 β = 104.0 γ = 90.0	a = 42.6, b = 41.9, c = 72.8 α = 90.0 β = 104.1 γ = 90.0
Mosaicity (°)	0.1	/	0.1	1.0
Resolution range (Å)	29.0 - 1.60 (1.70- 1.60)	40-2.0 (2.11-2.00)	35.0 – 1.20 (1.23 – 1.20)	50.0 – 2.0 (2.07 – 2.00)
Total No. of reflections	91 479	49256	214 938	34 024
No. of unique reflections	31 782 (5015)	11763 (1344)	74 523 (5233)	15 763 (1644)
Redundancy	2.8 (2.8)	4.2 (4.1)	2.9 (2.7)	2.2 (1.7)
Completeness (%)	96.1 (94.3)	73.6 (58.0)	95.7 (91.2)	92.2 (86.1)
(I/σ(I))	17.8 (5.7)	8.5 (6.7)	13.4 (3.2)	3.7 (1.6)
R_{merge} (%)	4.1 (19.6)	0.137 (0.193)	5.1 (43.4)	17.0 (47.1)

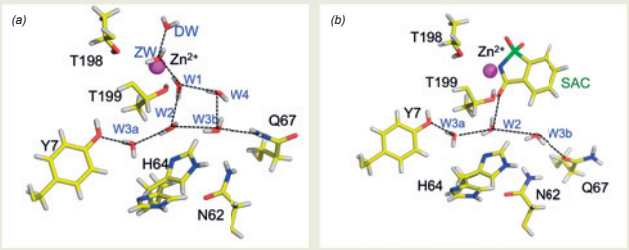

Fig.3. Neutron crystal structures of (a) apo HCA IX mimic, and (b) saccharin HCA IX mimic complex. Shown are the active sites: residues, metal, ligand, and solvent as labeled. H-bonds are shown as dashed lines.

DISCUSSION

- *The apo and saccharin complex neutron crystal structures are, as expected, homologous to the previously determined X-ray structures (PDB ID 4riv & 4zao).*
- *Fig.3 shows observed H-bonds as dashed lines. The H-bonds shown in Fig.3 can be directly observed due to the strong scattering from D atoms found in hydrophilic amino acid residues and exchanged water molecules.*
- *H64, the proton shuttling residue, is seen in two conformations, known as "in" and "out". (The "in" is slightly favoured in apo and refined to an occupancy of ~60%, this reversed in the saccharin complex where "in" occupancy is ~40%).*
- *4 water molecules are displaced in the saccharin complex (DW, ZN, W1, W4) leading to a net loss of 4 H-bonds (Fig.3-4). However, 5 H-bonds are retained "as is" or through some re-organization of solvent to accommodate saccharin. E.g., the H-bond that was between W3b and W4 is retained with W3b flipping and making H-bonds to Q67.*
- *The Q67 (N67 in HCA II) side chain has moved compared to its position in the apo structure with W3b re-orienting and maintaining the H-bond, but as a H-bond donor (Fig. 3b and 4).*

CONCLUSION

Neutron data provides a highly detailed view of drug binding that can be exploited in energy and docking calculations. These details also inform studies on regions of interest in the target as well as which areas of the inhibitor to derivatize for improved drug design. We are currently working on perdeuterated HCA IX mimic and hydrogenous native HCA IX (both the full length construct and the soluble CA domain). We are expanding our knowledge by pursuing neutron structures of HCA IX complexes with two new CA inhibitors (Fig. 5).

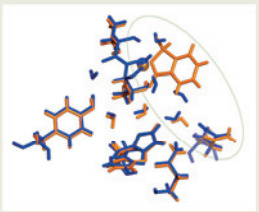

Fig.4. Overlay of the apo (blue) and saccharin (orange) complex neutron crystal structures. Circled is the area around saccharin where changes upon saccharin binding can be seen.

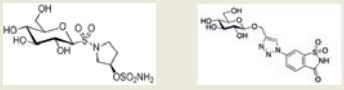

Fig.5. Sulfonamide- and saccharin-conjugated inhibitors that are being complexed to HCA IX for neutron studies

Now we are also developing methods for expression of perdeuterated protein (Fig. 6) which will enable us to collect high resolution neutron data .

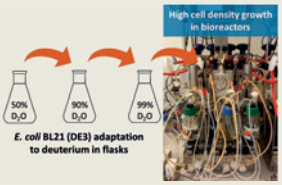

Fig 6: Development of effective methods for perdeuteration: adaptation of E. coli to deuterium and high cell density production for high-yield of perdeuterated proteins.

Interreg
Öresund-Kattegat-Skagerrak
European Regional Development Fund
EUROPEAN UNION

Acknowledgements: Beamline staff at MAX lab, ILL, and MLZ for help in collecting and processing X-ray and neutron diffraction data. Funding provided by : Interreg (MAX4ESSFUN) LU-008, SINE2020 WP6; The Crafoord Foundation 20160528, Fysiografen, & Lund University.

Optimization of species specific pyrimidine synthesis inhibitors using structural biology

Mikael Andersson[1], Parveen Goyal[1], Hans-Petter Hersleth[2], Salam Al-Karadaghi[3], Ulf Nilsson[4], Rosmarie Friemann[1]

[1] Department of Chemistry and Molecular biology, University of Gothenburg, Sweden
[2] Department of Biosciences, University of Oslo, Norway
[3] Department of Biochemistry and Structural biology, Lund University, Sweden
[4] Department of Chemistry, Lund University, Sweden

See separate box for full list of contributing collaborators.

Summary. Pyrimidine is the molecular base for 3 out of four nucleic acids, making it a critical compound for cell proliferation. Targeting the de novo synthesis of pyrimidines is a good way to downregulate cell proliferation.[1]

Malaria is a severe and common infectious disease caused by parasitic protozoans, most notably *P.falciparum* and *P.vivax*.[2] The parasitic protozoans responsible for Malaria completely relies on de novo synthesis of pyrimidines.[3] Thus, inhibition *pf*DHODH/*pv*DHODH prevents their replication.[1,3] Though human and protozoan DHODH are largely similar and catalyze the same reaction, they bind the necessary quinone cofactor differently. This make it possible to design potent DHODH inhibitors with species specific inhibition profiles.

The evolutionarily preserved importance of pyrimidine synthesis also make DHODH a suitable drug target for antiproliferative drugs primarily targeting autoimmune diseases.[1]

In this project we use iterative cycles of inhibitor design and structural determination of DHODH-inhibitor interactions to 1. develop potent species specific inhibitors of pfDHODH and pvDHODH to act as antimalarials, 2. develop potent inhibitors of *hs*DHODH to act as immunosuppressants and various other antiproliferative rolses.

Importance of pyrimidine synthesis

Pyrimidine is a molecule which serve as the base for three out of the four nucleic acids in the cell. This makes pyrimidine a limiting compound for rapidly dividing cells as it is needed for both DNA and RNA replication. For cells there are generally two strategies for obtaining pyrimidines, de novo generation of pyrimidines and the scavenging of pyrimidines from the environment. For most non rapidly dividing cells DHODH scavenging is sufficient for maintaining normal cellular function.

Pyrimidine synthesis and DHODH

The enzyme dihydroorotate dehydrogenase (DHODH) that catalyzes the fourth step in the de novo pyrimidine biosynthesis is a key enzyme critical for pyrimidine formation. Specifically, DHODH catalyzes the conversion of dihydroorotate to orotate. The reaction generates two electrons, which in the case of human and plasmodium are shuttled via flavin mononucleotide to quinone. Due to binding both dihydroorotate and quinone DHODH has two substrate binding pockets. Though the dihydroorotate binding pocket shows great structural conservation between species the quinone pocket is less conserved between species, opening up the possibility of species specific DHODH inhibitors.

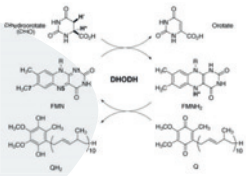

Malarial drug potential

Global health impact

Spread via mosquitos, Malaria is an infectious disease caused by parasitic protozoan parasites of the Plasmodium genus. The two most dangerous Plasmodium species are *P.falciparum* and *P.vivax*. Malaria constitutes a major disease burden world wide, with 3.2 billion people at risk if infection. For 2015 the there was an estimated 214 million cases of malaria world wide, resulting in a total of 438 000 deaths.[2]

Resistance and drug potential for DHODH inhibitors.

A proliferating resistance towards traditional antimalarial drugs such as chloroquine, sulfadoxine-pyrimethamine and artemisinin continue to hamper efforts in combating this disease.[2] Thus new antimalarial drugs are sorely needed to supplement and supplant traditional drugs.

In contrast to higher eukaryotes such as humans, Plasmodium lacks pyrimidine scavenging pathways and relies fully on de novo synthesis of pyrimidine to satiate its need for pyrimidines.[3] Coupled with a species to species variability within the quinone binding pocket of DHODH, this make pyrimidine synthesis and DHODH a prime target for anti malarial drugs.

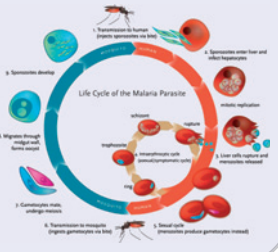

Plasmodium lifecycle

Picture source; Klein, E.Y. Antimalarial drug resistance: a review of the biology and strategies to delay emergence and spread, International Journal of Antimicrobial Agents , Volume 41 , Issue 4 , 311 – 317.

pfDHODH inhibitors based on 4-aminopyranone and 4-aminopyranopyrrolone show high species specificity and low cytotoxicity.

4-aminopyranone

Compound	IC_{50} ± SE[a] (μM) PfDHODH	IC_{50} ± SE[a] (μM) hDHODH	EC_{50} ± SE[a] (μM) P. falciparum 3D7
12	>100	n.d.[b]	n.d.[b]
13	69 ± 3.8	>100	n.d.[b]
14	2.9 ± 0.10	>100	0.85 ± 0.01(2)
15[c]	3.1 ± 0.20	>100	46 ± 19(3)

4-aminopyranopyrrolone

Compound	IC_{50} ± SE[a] (μM) PfDHODH	IC_{50} ± SE[a] (μM) hDHODH	EC_{50} ± SE[a] (μM) P. falciparum 3D7
16	>30	>100	n.d.[b]
17[d]	1.7 ± 0.13	>100	11 ± 1(2)
18[d]	12 ± 2.5	>100	n.d.[b]
19	0.74 ± 0.038	>100	6.2 ± 0.1(2)
20	43 ± 5.8	>100	47 ± 14(2)
21	16 ± 1.4	>100	n.d.[b]
22[d]	9.2 ± 1.0	>100	n.d.[b]
23[d]	0.26 ± 0.018	57 ± 1.6	n.d.[b]

[a]Data represent mean of triplicate samples run twice, presented as IC_{50} ± standard error.
[b]Not determinated.
[c]Number in parenthesis represents number of determinations.
[d]Crystal structures obtained

***pf*DHODH Inhibitor design**

Targeting the quinone binding pocket, *pf*DHODH selective inhibitors with pyranopyrrolone-, 4-aminopyranone-, and 4-aminocoumarine-based backbones were constructed and characterized. Starting with poor to medium inhibitors based on a pyranopyrrolone scaffold, further refinements of these structures let to the construction of sets of inhibitors based on 4-aminopyranone and 4-aminocoumarine backbones.

High resolution structures of these inhibitors bound to DHODH have been produced to aid in further rounds of DHODH inhibitor optimization.

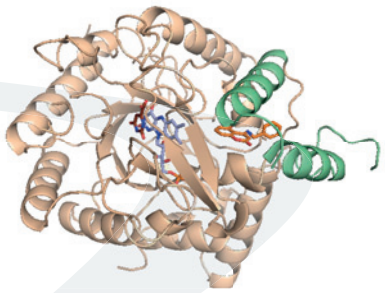

pfDHODH assumes an α/β-barrel fold. The dihydroorotate-binding site lies within the barrel. **Dihydroorotate** (brown) stacks against the internal **Flavin** (blue). The quinone-binding site is formed at the interface of the **N-terminal helices** (green) and the core barrel. An **inhibitor** (orange) located in quinone-binding at the interface of the **N-terminal helices** (green) and the core barrel is shown in orange.

Other drug potential of DHODH inhibitors

In humans fast replicating cells such as activated lymphocytes are repressed by pyrimidine synthesis inhibition. DHODH inhibition has been shown to be an effective way to combat various autoimmune diseases such as rheumatoid arthritis and multiple sclerosis.[1] All currently used inhibitors of *hs*DHODH binds the ubiquinone binding site. The antiproliferative effects of DHODH inhibition also makes DHODH an interesting drug target for cancer and proliferative skin diseases.[1].

DHODH inhibitors currently on the market displays severe side effect and new drugs are needed.[1] Potent *hs*DHODH inhibitors with low cytotoxicity and whose design is based upon known DHODH inhibitor Brequinar, has recently been created by the group of Marco Lolli. Our group has also crystalized and solved the structure for these inhibitors.

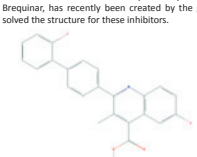

Brequinar

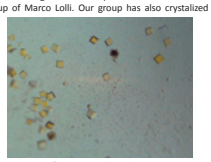

Crystals of *hs*DHODH, yellow color comes from the bound flavin

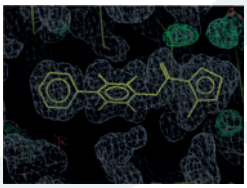

Brequinar derived inhibitor bound to ubiquinone binding pocket of *hs*DHODH

Full list of contributors

Ingela Fritzson[1], Henrik Johansson[1], Paul T. P. Bedingfield[1], Rhawnie Caing-Carlsson[2], Anders P. Sundin[3], Glenn McConkey[3], Stefano Sainas[4], Agnese C. Pippione[4], Marta Giorgis[4], Stefano Mensa[4], Cristina Ramondetti[5], Barbara Buccinnà[5], Rodolpho C. Braga[6,7], Carolina H. Andrade[7], Ann-Christin Moritzer[8], Elisa Lupino[4], Marco Piccinini[4], Donatella Boschi3 and Marco L. Lolli[4]

1. Organic Chemistry, Lund University, PO Box 124, 221 00 Lund, Sweden
2. Department of Chemistry and Molecular Biology, PO Box 462, 405 30 Gothenburg, Sweden
3. Faculty of Biological Sciences, University of Leeds, Leeds, England LS2 9JT, UK
4. Department of Science and Drug Technology, University of Torino, via Pietro Giuria 9, 10125 Torino, Italy.
5. Stephenson Institute for Renewable Energy, Department of Chemistry, University of Liverpool, L69 7ZF Liverpool, UK.
6. Department of Oncology, University of Torino, via Michelangelo 27/b, 10126 Torino, Italy.
7. LabMol, Faculty of Pharmacy, Federal University of Goias, 74605-170 Goiania, Brazil.
8. Department of Chemistry, Biochemistry, University of Bielefeld, Universitätsstraße 25, 33615 Bielefeld, Germany, 7

References

1. Munier-Lehmann H et al. *On dihydroorotate dehydrogenases and their inhibitors and uses.* J Med Chem. 2013, 56, 3148-3167.
2. World Health Organization. "World Malaria Report 2015. WHO, Geneva." (2015).
3. Baldwin, Jeffrey et al. Malarial Dihydroorotate Dehydrogenase, J Biological Chemistry. 2002, 277 (44), 41827-41834
4. Klein, E.Y. Antimalarial drug resistance: a review of the biology and strategies to delay emergence and spread, International Journal of Antimicrobial Agents , Volume 41 , Issue 4 , 311 – 317

Interreg
Öresund-Kattegat-Skagerrak
European Regional Development Fund

EUROPEAN UNION

Faculty of Science

UNIVERSITY OF GOTHENBURG

PROTEIN-PROTEIN INTERACTIONS STUDIED USING A LEVITATED DROP

Pernille Sønderby[a], Christopher Söderberg[b], Jens T. Bukrinski[c], Günther H. Peters[a], Tomás Plivelic[b] and Pernille Harris[a]

[a]*Department of Chemistry, Technical University of Denmark, Kemitorvet 207, DK-2800 Kgs. Lyngby, Denmark, pers@kemi.dtu.dk*
[b]*MAX IV Synchrotron, Lund University, Sweden*
[c]*CMC assist ApS, Copenhagen, Denmark*

Introduction

Characterization of proteins at high concentration is both time consuming due to sample preparation and costly due to the high sample amount needed. Additionally, high concentrated samples can be viscous and contamination of the sample chamber walls by protein aggregation can be a source of error. These challenges can potentially be overcome by the use of a contactless sample holder such as ultrasonic levitation.

SAXS studies of protein-protein interactions in levitating droplets are limited. The combination of SAXS and levitation for structural studies has been illustrated using apoferritin [1,2]. Protein studies with levitation have been used in trying to characterize the freeze-drying process of proteins and here a recent paper has applied the combination with SAXS in trying to follow the process [3].

In this study we wish to determine if levitation combined with SAXS can be used as a tool to investigate protein samples at higher concentration. The levitation process ensures an automated up-concentration of the sample, ensuring the use of only small amounts of sample.

Albumedix™ Recombumin®, recombinant human serum albumin, has been used as a model system.. Recombumin® has earlier been characterized extensively by our group at concentrations up to ~250 mg/mL, which provides a background for comparison.

SETUP

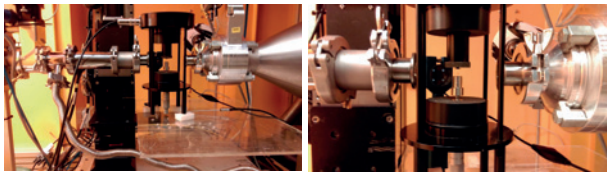

The measurements were performed at MAXIV laboratories, beamline I911-SAXS. The levitator was placed up-side down in the hutch and the beam and droplet position adjusted for each measurement. The droplet is positioned in the lower node of the acoustic wave and water in the sample will slowly evaporate thereby increasing the concentration of the protein. Convection around the droplet ensures mixing in the droplet during evaporation.

Droplet size determination and Evaporation behaviour

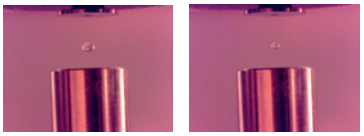

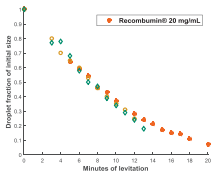

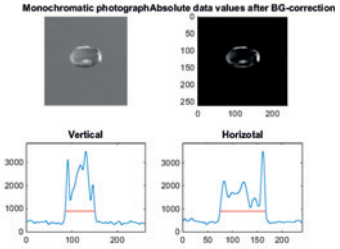

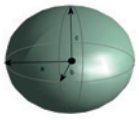

To determine the concentration for each SAXS measurement, a picture was taken of the droplet at each acquisition. The evaporation rate can then be monitored and an concentration determined from the decrease in droplet volume. The volume was determined in Matlab by estimating the dimensions of the droplet and calculating the volume assuming a droplet shape as an ellipsoid.

Method

SAXS measurements were performed at MAXIV I911-SAXS. Sample size: 1-2 µL was applied using a hamilton syringe in a 100 MHz Levitator from Tec5. Wavelength: 0.9100 Å, Detector: Pilatus 1M. Sample – detector distance: 1921 mm, 285K. Data analysis: PyQtFAI, Primus.
Recombumin® from Albumedix A/S (Buffer: 145 mM NaCl, 8 mM octanoate, 0.05 g/L Tween 80, pH~7).

Challenges

We observe a discrepancy between protein concentration determined from droplet size and from I(0) as seen in the plot to the right.

The decreasing size of the droplet poses an issue when the droplet size reaches that of the beam size. This is illustrated in the figures below.

The intensity is normalized to the transmission, thereby taking the change in path length into account. It is, however, seen to the right that when the droplet becomes smaller than the beam, the smaller volume affects the signal.

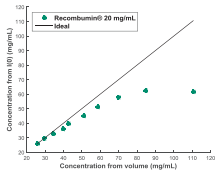

Ideal **Droplet < Beam**

Red lines: beam size, Black lines: scattering, Green lines: unwanted reflection

SAXS results

Data were collected on Recombumin® at different starting concentrations and volumes. Different exposure and delay times were evaluated as well.
An increase in concentration followed by repulsive behaviour is observed (figure below – left).
The obtained data were compared to data collected in a traditional flow-cell. At 50 mg/mL we see that the two scattering curves have the same profile but that the interaction potential is changed (figure below – right). This is probably due to the fact that the buffer also gets more concentrated during levitation.

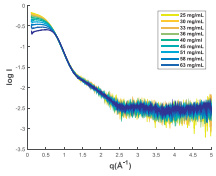

Initial concentration of 20 mg/mL. 12 minutes levitation result in up-concentrated to ~60 mg/mL. Exposure 30 sec, delay 30 sec.

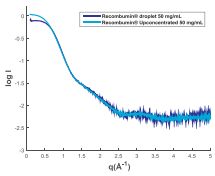

Recombumin® up-concentrated (exposure 3*60 sec, and averaged) compared to droplet data (dark blue).

Conclusion and perspective

- Evaporation profiles are reproductive
- Concentration determination from I(0) do not correspond to volume estimates from droplet size
- Scattering data show good agreement with previously collected data though the interaction potential seem affected

The methodology is promising for characterizing the effects of up-concentration of proteins. We find a few challenges that have not been mentioned in previous work which need to be solved. Additionally the effect of buffer and its components during the evaporation procedure will be evaluated by investigation of other systems.

Acknowledgements

Albumedix A/S for providing the Recombumin®
Interreg Öresund-Kattegat-Skagerrak and Danscatt for funding

Albumedix and Recombumin® are trademarks of the ALBUMEDIX Group.

References

[1] F. Deißen *et al.* (2008) "Agglomeration of proteins in acoustically levitated droplets" *Anal. Bioanal. Chem, 392, 161-165*
[2] J. Leiterer *et al.* (2008) "Structure analysis using acoustically levitated droplets" *Anal. Bioanal. Chem, 391, 1221-1228*
[3] V. Cristiglio *et al.*(2016) " Combination of acoustic levitation with small angle X-ray scattering techniques and synchrotron radiation circular dichroism. Application to the study of protein solutions" *Biochim. Biophys. Acta (Article in Press)*

XAS on Metalloproteins – BALDER Beamline

Ulf Molich*, **Kajsa G. V. Sigfridsson Clauss§**, **Christian G. Frankær#**, **Kenny Ståhl***, **Pernille Harris***

*Department of Chemistry, Technical University of Denmark §MAX IV Laboratory #Department of Chemistry, University of Copenhagen

Metalloproteins are essential for living organisms, and their functions are often related to redox processes. An accurate description of the local structure of the redox center in the different oxidation states is a key to understand the mechanisms of such proteins and could also be useful in rational drug design involving metalloproteins.

Why use XAS on Metalloproteins ?

- Provides information about the metal sites; including number and identities of neighbors, distances and coordination geometry
- Oxidation state of metal ions can be resolved
- Does not depend on physical state of sample
- Photoreduction and radiation damage can be monitored and controlled

Objective

To improve the use of XAS in analyzing metalloproteins.

Previous methods required cryocooling of protein samples to avoid radiation damage. This puts the protein in unnatural conditions, and prohibits *in situ* investigation of redox reactions.

Previous flow cell required large sample volume, which prevented studies of hard to obtain proteins.

X-ray Absorption Spectroscopy (XAS)

Principle

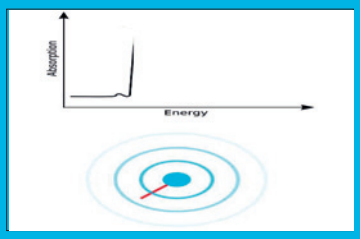

XANES fitting

The XANES region gives information about the local geometry. In principle, theoretical spectra are calculated as functions of geometric parameters, that are linearly fitted to the observed data.

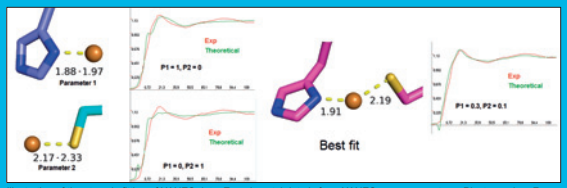

Illustration of the steps in fitting of XANES data. Experimental data is from XANES measurements on Plastocyanine. From left to right: Parameters are defined, theoretical spectra are calculated, best fit to experimental data is found.

Acknowledgements

Thanks to Interreg Öresund-Kattegat-Skagerrak for providing funding for the project.
Thanks to Nicolai Wenceslaus Kriesz for assistance in making the video.

Balder Beamline at MAX IV

Specifications

- Energy 2.4 – 40 keV (= Sulfur to Lanthanum K-edge)
- Flux 10^{12} - 10^{13} photons/sec
- Beam size 100µm x 100µm (focused)

Development of a Flow Cell System

The flow cell will provide fresh sample to the X-ray beam, and biocatalytic reactions can be studied.

Schematics of the flow cell design, a microfluidic chip for X-ray spectroscopy:

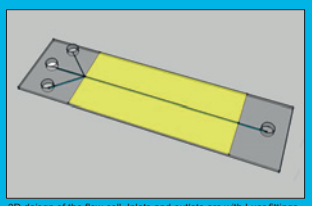

3D deisgn of the flow cell. Inlets and outlets are with Luer fittings to allow easy compatibility with flow systems. The yellow area is without a surface layer, and will be covered with Kapton foil.

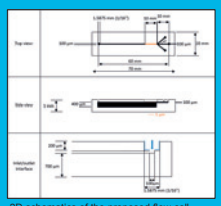

2D schematics of the proposed flow cell design.

Advantages of microfluidics

- Lower sample consumption, allowing studies of proteins that are hard to purify
- A controlled flow of sample to avoid radiation damage, allowing experiments at **room temperature**
- The laminar flow presents a homogenous sample to the X-ray beam, and through precise flow control and rapid mixing can reactions be followed by measurements at different positions on the flow channel

Flow cell at beamline I811, MAX II

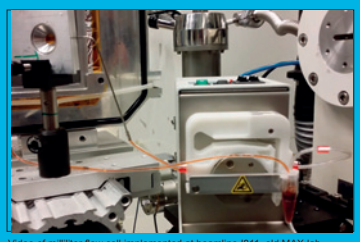

Video of milliliter flow cell implemented at beamline I811, old MAX-lab.

Neutron crystal structure determination of triosephosphate isomerase

Vinardas Kelpsas[1], Esko Oksanen[2] and Claes von Wachenfeldt[1]

[1] Department of Biology, Lund University Sölvegatan 35, 223 62 Lund, Sweden

[2] European Spallation Source ERIC, Tunavägen 24, 221 00 Lund, Sweden

Introduction. Hydrogen atoms play a crucial role in enzyme catalysis, protein-ligand and protein-drug interactions. Neutron macromolecular crystallography (NMX) offers a unique approach for locating individual atoms by leveraging the neutron scattering properties of the hydrogen isotope deuterium (D). NMX can provide information on protonation states of active site residues in enzymes, H-bonding networks and orientation of solvent molecules. In this project we will use NMX to collect neutron diffraction data and determine crystal structure of triose phosphate isomerase (TIM) of the protozoan parasite *Leishmania mexicana*. Large volume crystals are required for NMX and is often a limiting factor for this technique.

Figure 1. X –ray structure of TIM with PGH (in color). PDB 2XVN

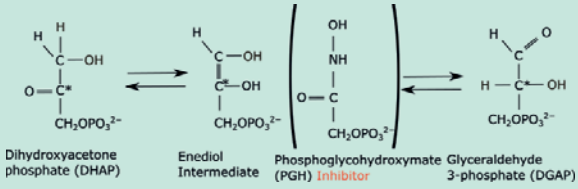

Figure 2. Reaction catalyzed by TIM. * marks the chiral center of DGAP. During catalysis the intermediate, enediol, is present. To study the protonation state of the intermediate, NMX of TIM in complex with the reaction intermediate analog PGH will be done.

Production of perdeuterated protein

- To increase signal to noise ratio hydrogens are exchanged for deuterium, by producing the protein in deuterated growth media.
- Deuterated growth media are expensive, impairs growth and protein yield.
- Cost-effective methods for perdeuteration are needed.
- We have optimised expression conditions to obtain uniformly deuterium-labeled TIM for NMX.

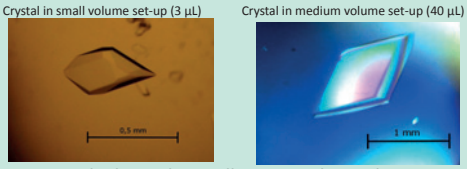

Figure 4. Crystals obtained in small versus medium volume set-up

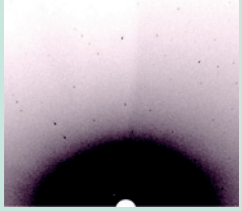

Figure 5. A part of a quasi-Laue diffraction image from LADI showing diffraction spots to the top edge of the detector

Triosephosphate isomerase

- TIM is a key enzyme in glycolysis.
- Interconverts DHAP and GAP (Figure 2).
- Catalysis is driven by proton abstraction but the reaction mechanism is not fully resolved.
- Ultra-high resolution X-ray structure (0.82 Å), did not give conclusive information about protonation state of the reaction intermediate and the active site hydrogen-bonding network.
- PGH, a reaction intermediate analog, is used to address the protonation state of the reaction intermediate.

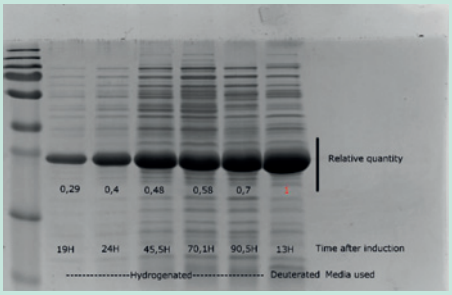

Figure 3. TIM expression in *Escherichia coli* in deuterated (D-M9) and hydrogenated (H-M9) media.

Crystalization of TIM

- Large volyme crystals (>1 mm^3) are required.
- Crystallization in deuterated buffer could reduce size of crystals.
- Neutron Laue measurements to a nominal resolution of 2.1 Å of a small crystal (~0.1 mm^3) has been recorded.
- By increasing the drop size in crystalization from 3 µl to 40 µl we were able to obtain several crystals at least 3 times larger (> 0.3 mm^3) than the tested one.
- Further optimizations are carried out to increase drop size to 200 µL, to obtain even larger crystals.

Vinardas Kelpsas, Department of Biology, Sölvegatan 35, 223 62 Lund, Sweden vinardas.kelpsas@biol.lu.se

Material Sciences

Tracking the photo-isomerization stages of Ruthenium based complexes for energy storage

Amal el Nahhas[1], T. Harlang[2], A. Fossati[1], K. Kjaer[1], T. Brandt van Driel[2], A. Lennartsson[3], K. Moth-Poulsen[3], K. Haldrup[2], and J. Uhlig[1]

[1] Department of chemical physics, Lund University, Sweden
[2] Department of physics, Technical University of Denmark
[3] Department of chemical and biological engineering, Chalmers University of Technology, Gothenburg

Introduction

With the shrinkage of fossil natural resources like oil, coal or natural gas, finding ways to store energy has become a priority challenge task for our modern society. One approach for covering the world energy need is to exploit the sun's great potential and convert the solar energy to either electricity by photovoltaics technologies or heat by solar thermal ones [1]. In this context we are interested in the photochemistry of diruthenium fulvalene tetracarbonyl $Ru_2Fv(CO)_4$ systems where Fv = $(\eta^5\text{-Cp})_2$ and Cp = C_5H_5. These are capable of storing solar energy in the form of chemical bonds and then releasing it "on demand" [2-4]. Mechanistically this is achieved by photoconverting the "parent" molecular (cis-configuration) to a stable higher energy "photoisomer" (trans-configuration). The latter then releases its energy in form of heat upon excitation and achieves high turnover number. An increase of the yield was obtained when adding sterical constraints in the Fv part. In order to get a better understanding of the chemical reactions and scientific insights into the parameters responsible for the performance of these new compounds we have performed optical pump-probe together with time resolved X-ray diffuse scattering (XDS) experiments. The latter technique being an efficient tool to determine the geometric structure allows us to generate a scheme of the different stages of the photoisomerization process, necessary to control it.

Results

Proposed photoisomerization mechanism

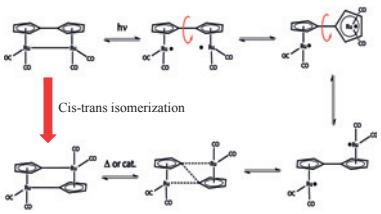

Investigated systems

Time resolved Xray Diffuse Scattering (XDS) experiments

- Performed at ID09b beamline at ESRF synchrotron
- Ru_2Me_4Fv in THF and toluene
- 400 nm excitation
- Images at different time delays after laser excitation

XDS signals at different time delays

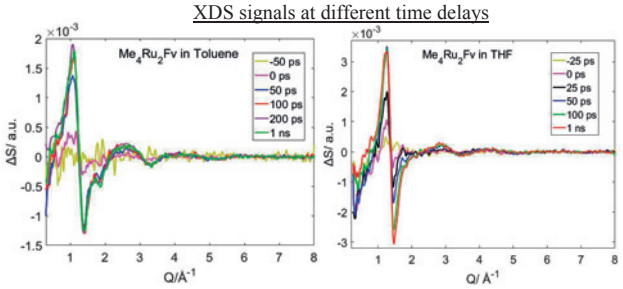

Solvents/Viscosity

ACN	0.37 cP
THF	0.46 cP
Toluene	0.56 cP
DMSO	2 cP

Transient absorption (TA): 400 nm pump, white light probe

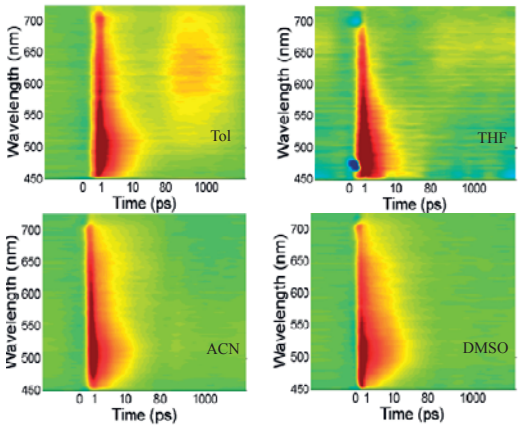

Solute/solvent signals difference vs simulation

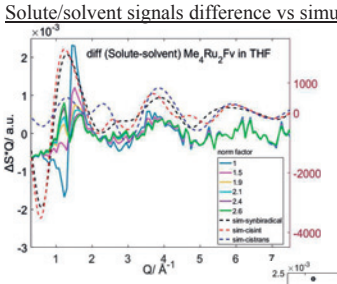

Non structural parameter fit

- Me_4 in THF at 25 ps

structure	chi^2
synbir	$5.43*10^{-5}$
cisInt	$5.9*10^{-5}$
cistrans	$9.02*10^{-5}$

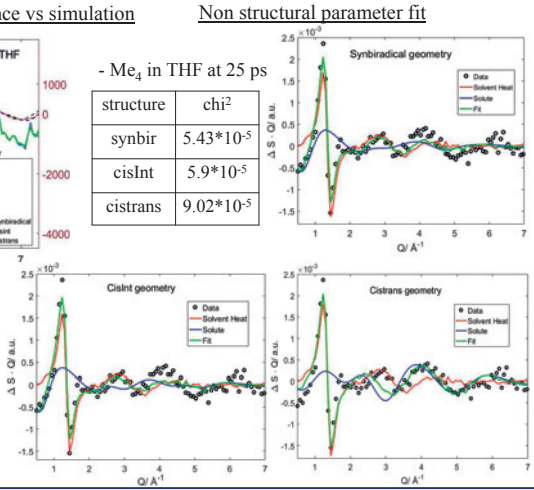

Obtained decay times

t_1 ~1 ps: substitutions and solvents independent
t_2 ~ 10 ps: increasing when increasing the methylation from Me_3 to Me_4
t_3 ~ ns: substitutions and solvents dependent
t_4 : rising component in high viscosity solvents:
~50 ps (Me_3 and Me_4) in Toluene and 3.3 ns unsubstituted in DMSO

Conclusion

- Solvent and substitutions affect strongly the relaxation process and the decay times.
- t_1 and t_2 same species, similar species associated spectra
- ns different state => different geometry.
- Similarly to related systems, we assign the obtained states to the syn biradical singlet and triplet ones.
- Cistrans structure => better fit at Q>3.2 $Å^{-1}$.
- CisInt/synbiradical structures => better fit at Q<3.2 $Å^{-1}$.
- Mixture of the cistrans and cisInt/synbiradical structures.
- The fit result of the solute non structural parameter matches the decay behavior obtained by TA.

Proposed Relaxation diagram

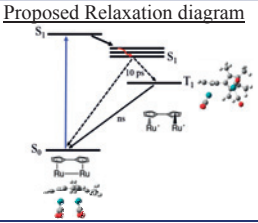

References: [1] MacKay, D.JC., in Numbers, not adjectives in Sustainable Energy – without the hot air, Ed. UIT Cambridge, 2008. [2] Boese, R. et al., J. Am. Chem. Soc., 119, 6757-6773, 1997, [3] Moth-Poulsen, K. et al., Energ. Environ. Sci., 5, 8534-8537, 2012, [4] Harpham, M. R. et al., Angewandte Chemie, 51, 7692–7696, 2012.

DTU Mechanical Engineering
Department of Mechanical Engineering

Interreg Öresund-Kattegat-Skagerrak European Regional Development Fund
EUROPEAN UNION
DTU

Monitoring microstructural evolution during reversed deformation by high-resolution reciprocal space mapping

Annika M. Diederichs[1], Dmytro Orlov[2], Wolfgang Pantleon[1]

[1] Department of Mechanical Engineering, Materials and Surface Engineering, Technical University of Denmark, 2800 Kgs. Lyngby, Denmark
[2] Department of Mechanical Engineering, Materials Engineering, Lund University, 221 00 Lund, Sweden

Fatigue-related damage due to cyclic deformation in metals is still one of the major failure reasons in structural materials. Internal structures are known to influence the material lifetime, but the understanding of the interaction between grains and subgrains on the microscale is still insufficent. Recently developed synchroton techniques such as High Resolution Reciprocal Space Mapping can help to establish microstructural models based on in-situ investigations. The MAX4ESSFun Project DTU-007 provided knowledge exchange in synchrotron techniques and supported interregional collaboration on structurally similiar materials as cyclically deformed aluminium and harmonically structured nickel.

Cyclic deformation in fcc metals

Plastic deformation of metals is accomplished by dislocation motion. Dislocations self-organize during cyclic deformation into ordered dislocation structures, consisting of dislocation-rich walls and dislocation-poor cells or subgrains with different mechanical properties as described in Mughrabi's composite model.

Two differently processed materials are investigated:

1. Commercially pure aluminium AA1050 after rolling to 1mm thickness and annealing are monitored during cyclic deformation
2. Pure nickel with harmonic structure consisting of sintered particles with fine-grained shells and coarse-grained cores, which makes their composite structure comparable to organized dislocation structures.

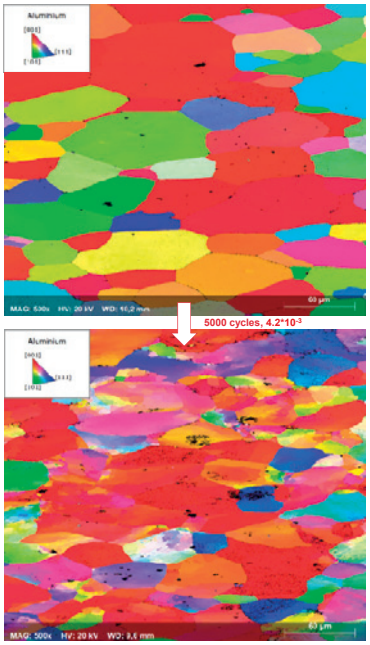

Fig.1: Orientation map obtained by EBSD and colored according to crystallographic direction of the tensile axis (see inset) showing the development of subgrain structures during cyclic deformation in polycrystalline aluminium; top: undeformed aluminium after annealing, no orientation differences within the grains are visible, bottom: 2% predeformed and cyclically deformed aluminium (after 5000 tension compression cycles, fracture at approx. 12000 cycles) showing distinct intragranular orientation differences and subgrain formation within the grains. Stepsize 250 nm. Black spots are non-indexed points due to sample preparation.

High Resolution Reciprocal Space Mapping (P07 at PETRA or 1-ID at APS)

Due to their deep penetration, high energy x-rays are suitable for non-destructive investigations on bulk material. Reflections of single grains (about 30 µm for full illumination by the planar focussed beam) can be selected in the used set-up (cf. Fig.3). In this way, structural features can be identified due to their orientation contrast (cf. Fig.4). By specifically constructed load frames, the specimen can be deformed in-situ and, hence, the microstructural evolution of single grains can be followed under load.

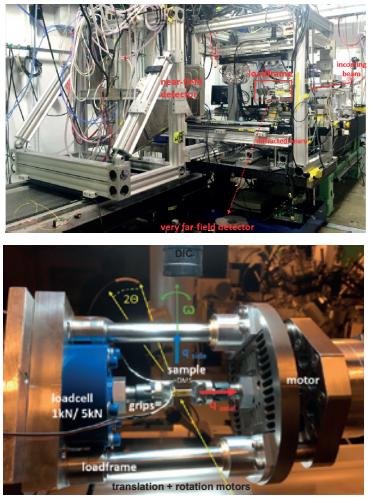

Fig. 2: Experimental set-up at APS 1-ID-E; top: Image of the set-up showing a near-field GE-Detector on horizontal translation, which is used for finding grains. A mar165 is positioned as very-far field detector (not in image) at approx. 4.7 m behind the loadframe to image selected (400 parallel to tensile axis) Al reflections with high angular resolution during rocking of the sample. bottom: Loadframe and diffraction geometry for HR Reciprocal Space Mapping. The bone-shaped sample (with two strain gages) is mounted in a horizontal loadframe positioned in the rotation axis on top of rotation and translation stages. The rotation axis is perpendicular to the scattering plane (rocking).

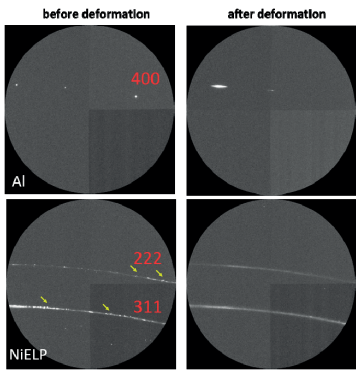

Fig. 3: Images from very far field detector showing part of the diffraction rings of aluminium (2Θ(400,53keV)=13.3°) and harmonic nickel (2Θ(311,222,53keV)=12.65°,13.22°) before and after deformation. The harmonic Ni structures show interesting diffraction features indicating strain already before deformation; peak broadening is clearly visible after deformation.

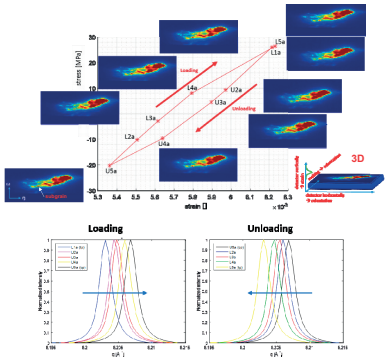

Fig. 4: Azimuthal maps (top) and radial profiles (bottom) aquired during one full tension-compression loadcycle at APS 1-ID-E. Azimuthal maps are projections of the intensity distribution along the scattering vector made from a 3D stack, representing the grain structure and basis for the identification of individual subgrains (high-intensity peaks). Radial profiles are projections of the intensity distribution onto the radial direction and provide strain information. Here they show that the peak positions shifts during loading and unloading. Peak profiles for tension points (L1a, L5a) overlap.

EUROPEAN SPALLATION SOURCE

DETECTOR GROUP

Interreg Öresund-Kattegat-Skagerrak European Regional Development Fund

EUROPEAN UNION

BUILDING A BORON-10 NEUTRON DETECTOR

IRINA STEFANESCU
EMIL ROFORS

PRINCIPLE

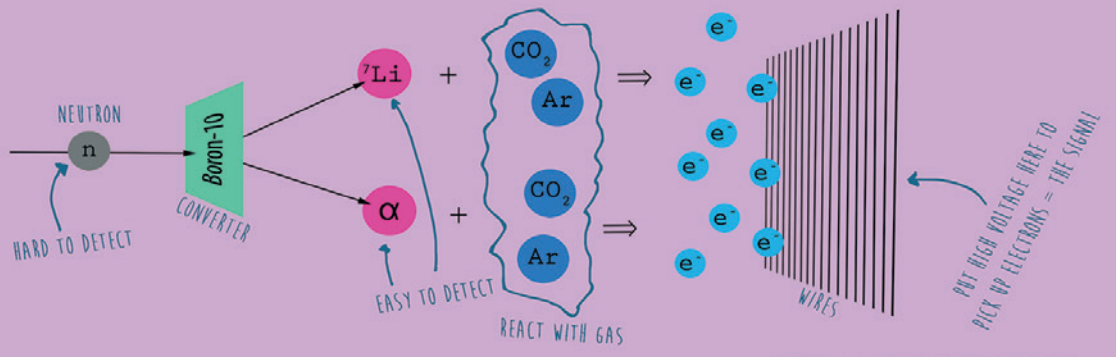

BUILDING

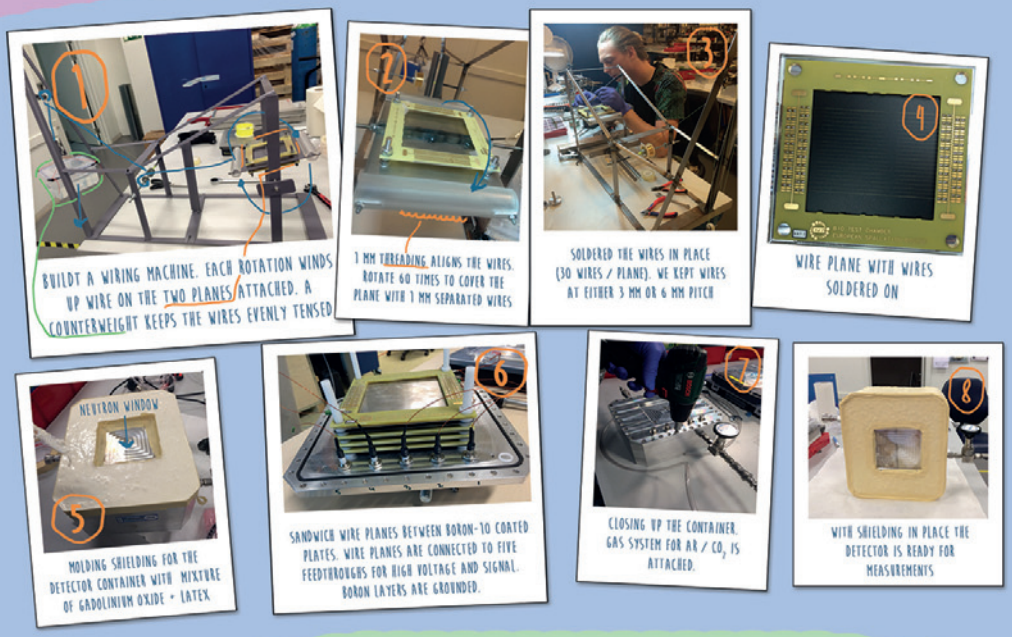

TESTING

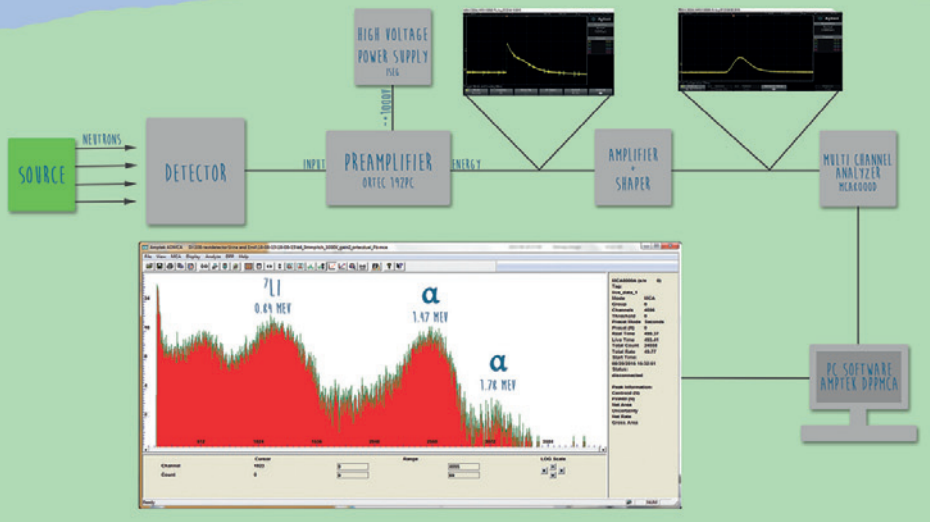

$RuAs_2$ - A promissing thermoelectric material

Karl F. F. Fischer*, Hazel Reardon, Lasse R. Jørgensen, and Bo B. Iversen

Center for Materials Crystallography, Department of Chemistry and iNANO, Aarhus University, Aarhus, Denmark

*Karl@chem.au.dk

Motivation

The reported band gap and Seebeck coefficient of ~0.8 eV and -350 µV/K, respectively, makes $RuAs_2$ a promising thermoelectric material.[1] However, these data have been criticized for lack of structural and compositional analysis.[2] $RuAs_2$ is structurally related to many naturally occurring minerals, giving reason to believe that it is very stable.

Structure and synthesis

$RuAs_2$, like most other transition-metal di-pnictides, has the marcasite structure (distorted pyrite). It consists of anionic pnictide dimers and octahedrally coordinated metal cations.

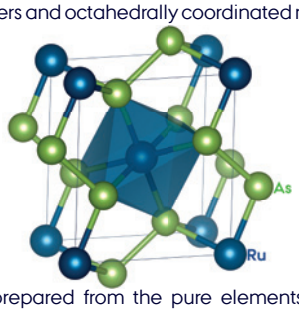

$RuAs_2$ was prepared from the pure elements in a sealed ampoule. The resulting powder was then pressed in a Spark Plasma Sintering (SPS) press. Compositional and structural analysis of the powder and pellet was done using X-ray powder diffraction measured at the SPring-8 synchrotron.

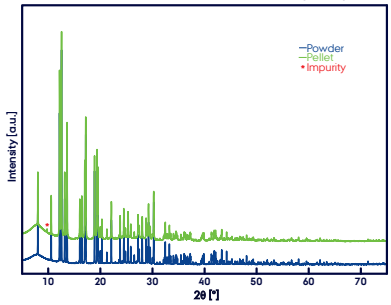

A comparison of the diffraction patterns shows the formation of an unidentified impurity during SPS pressing. Refinement of the diffraction data measured at SPring-8 shows a minor loss of arsenic during sintering.

References

[1] F. Hulliger, Nature 198, 1081 (1963)
[2] H. Holseth, A. Kjekshus, A.F. Andresen, and W.B. Pearson, Acta Chem. Scand. 22, 3273 (1968)

Physical properties

The electrical resistivity and Seebeck coefficient were measured on homebuilt instruments, while the thermal conductivity was measured using a commercial laser flash. An Arrhenius type fit of the resistivity data yields two band gaps, the larger consistent with the reported data, the smaller could stem from either the arsenic vacancies or the impurity. While the Seebeck coefficient is promising, the high thermal conductivity and electrical resistivity result in a very low zT.

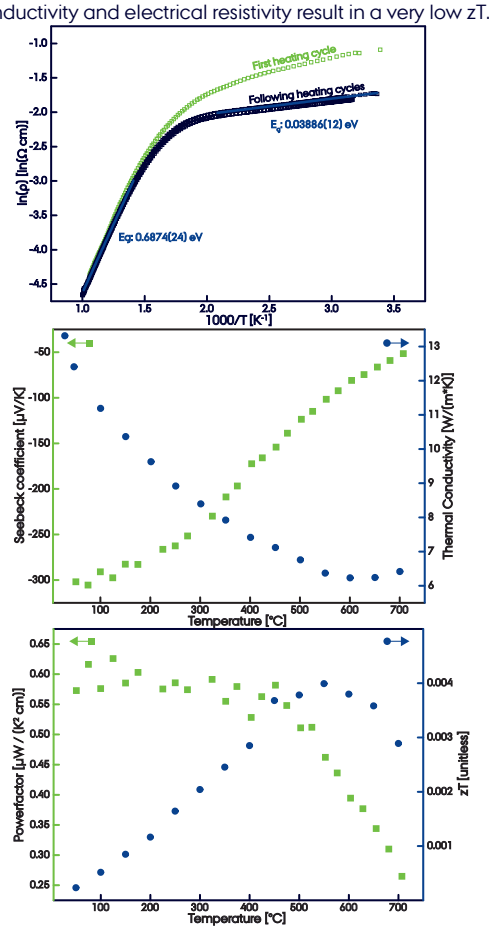

Conclusion and outlook

Identifying the impurity and limiting arsenic loss during pressing could improve performance. These issues would not have been identified without high quality X-ray diffraction.

Danmarks Grundforskningsfond
Danish National Research Foundation
CMC
iNANO
Interreg
Öresund-Kattegat-Skagerrak
European Regional Development Fund
EUROPEAN UNION
DanScatt

OPPOSITELY CHARGED POLYELECTROLYTES: SYNTHESIS AND STUDIES OF THE KINETIC PATHWAYS OF NANOPARTICLE FORMATION USING TR-SAXS

Jakob Stensgaard Diget[1,*], Bo Nyström[1], Theyencheri Narayanan[2], Jan Skov Pedersen[3] and Reidar Lund[1,*]

[1]*Department of Chemistry, University of Oslo, P.O. Box 1033, Blindern, N-0315 Oslo, Norway.*

[2]*ESRF - European Synchrotron, 71 Avenue des Martyrs, F-38043, Grenoble, France.*

[3]*Interdisciplinary Nanoscience Center (iNANO) and Department of Chemistry, Aarhus University, Gustav Wieds Vej 14, DK-8000 Aarhus C, Denmark*

[*]*E-mail: j.s.diget@kjemi.uio.no, reidar.lund@kjemi.uio.no*

Summary

Block copolymers with one hydrophilic block and a charged polyelectrolyte block that are mixed with oppositely charged homopolymers can form nano-sized micelle-like aggregates. Due to the electrostatic interactions, rearrangement requires cooperative movements of the blocks and the kinetics of formation is very different from that of conventional micelles possibly with several barriers involved.

In this study, (vinylbenzyl)trimethylammonium chloride has, to our best knowledge, been polymerized for the first time by using Atom Transfer Radical Polymerization (ATRP) to yield well-defined positively charged (block) co-polyelectrolytes. Various ATRP approaches were employed and the kinetics were investigated thoroughly to gain a firm understanding of the polymerization mechanism. Homo-polyelectrolytes were synthesized employing EBiB as initiator and block co-polyelectrolytes were synthesized using a PEG-macroinitiator.

Mixing the positively charged block polyelectrolyte with a negatively charged counter-polyelectrolyte, poly(sodium styrene sulfonate), resulted in stable complexes. The kinetic pathway of aggregate/micelle formation was investigated using synchrotron SAXS with millisecond time resolution. Using TR-SAXS we are able to follow the whole transition from initial nuclei, metastable clusters to the equilibrium state.

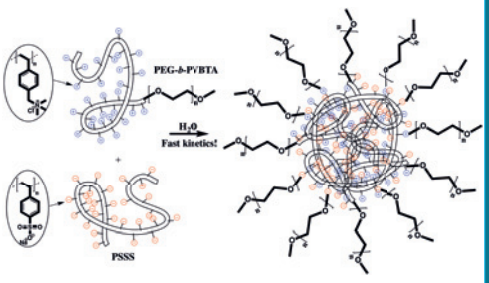

Idealized PEG-stabilized polyelectrolyte aggregate

Synthesis, ATRP

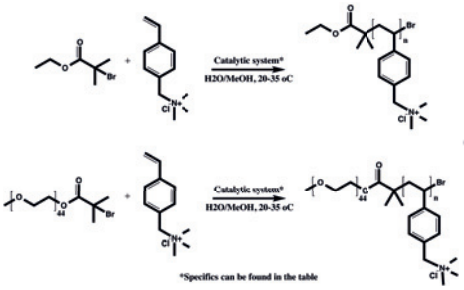

Precipitation, dialysis, freeze-drying, 1 and 2D NMR, AF_4

PVBTA	Catalytic system	T(°C)	Reaction(hrs)	M_n(NMR)	Charged units	$M_n(AF_4)$	PDI(AF_4)
D53	CuBr, CuBr2, bpy, NaAsc*	35	39.5	11150	51.8	13010	1.08
D54	CuBr, CuBr2, bpy, NaAsc	35	47	10420	48.3	11600	1.11
D55	CuBr, CuBr2, bpy	35	47	6410	29.3	6820	1.11
D56	CuCl, CuCl2, bpy	35	47	6230	28.5	7240	1.05
D57	CuBr, CuBr2, bpy	RT	145	7500	34.5	8070	1.06
D58	CuCl, CuCl2, bpy	RT	145	6630	30.4	6820	1.05
D59	4,4'-Azobis(4-cyanovaleric acid)	70	17	N/A	N/A	461300	2.08
D61	CuBr, CuBr2, Me6TREN	RT	0.75	11500	53.4	87890	3.42
PEG-b-PVBTA							
D60	CuBr, CuBr2, bpy	35	47	4560	11.9	5080	1.05
D62	CuBr, CuBr2, Me6TREN	35	1	47990	217.0	527900	2.47
D63	CuBr, CuBr2, bpy, NaAsc	35	67.5	8380	30.0	10650	1.04
D64a	CuBr, CuBr2, bpy, NaAsc	35	3	3200	5.5	4200	1.07
D64b	CuBr, CuBr2, bpy, NaAsc	35	5	3620	7.5	4590	1.05
D64c	CuBr, CuBr2, bpy, NaAsc	35	21	6010	18.7	7470	1.05
D65	CuBr, CuBr2, bpy, NaAsc	35	1	2590	2.6	3810	1.01

*Freeze-Pump-Thaws were used to remove oxygen

Analysis of polymerization kinetics using ^{1}H NMR

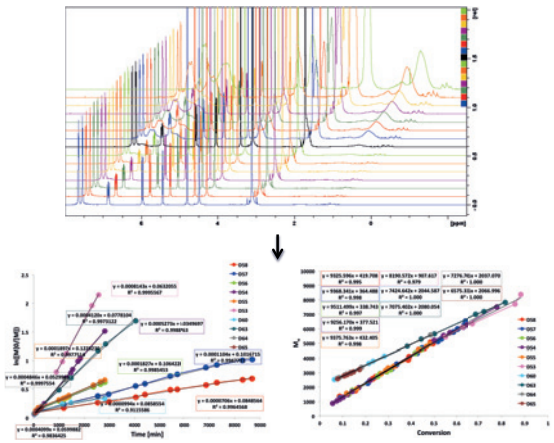

The control of reaction was proven by the linear evolution of M_n(conversion), the low PDIs and by the linear progression of ln([M]0/[M]), proving that the polymerization followed first order kinetics. The apparent rate constant was isolated as the slope.

For four comparable ATRPs (same concentrations and CuBr and CuBr2 used for all) the following kapp's [×10-6/sec] were isolated

$k_{app,\ PVBTA5}$ = 314 (T = 35 °C, Me6TREN as ligand)

$k_{app,\ PVBTA7}$ = 8.79 (T = 35 °C, bpy as ligand, NaAsc as reducing agent)

$k_{app,\ PVBTA2}$ = 3.18 (T = 35 °C, bpy as ligand)

$k_{app,\ PVBTA1}$ = 2.01 (T = RT, bpy as ligand)

The k_{app}'s followed the expected trend:

$k_{app,\ PVBTA5} > k_{app,\ PVBTA7} > k_{app,\ PVBTA2} > k_{app,\ PVBTA1}$

Preliminary results from time-resolved SAXS

Charge balanced nanoparticles (1:1 cations:anions) were formed. mPEG-b-PVBTA was mixed with PSSS (PDI = 1.2) using a Stopped Flow Apparatus (SFA) coupled directly to the ID02 SAXS instrument at the ESRF as shown in the figure below. As expected, short polymers rearrange much faster than large polymers.

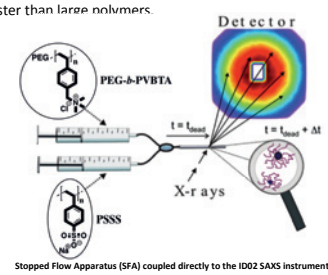

Stopped Flow Apparatus (SFA) coupled directly to the ID02 SAXS instrument

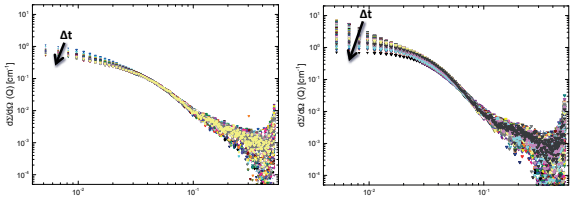

SAXS data for D65 (3 positive charges) + PSSS (30 negative charges)

SAXS data for D60 (12 positive charges) + PSSS (19.5 negative charges)

Acknowledgement

The authors greatly appreciate the financial support of the European Union through the NanoS3 project (GrantNo. 290251) of the FP7-PEOPLE-2011-ITN call and the MAX4ESSFUN, which is part of the EU project 'ESS & MAX IV: Cross Border Science and Society. We are grateful for the European Synchriotron Radiation Facility (ESRF) for allocation of beamtime.

In operando scanning X-ray diffraction microscopy of nanowire devices

Jesper Wallentin[1,2], Markus Osterhoff[2], Tim Salditt[2]

[1] Synchrotron Radiation Research, Lund University, Sweden. Email: jesper.wallentin@sljus.lu.se
[2] Institut für Röntgenphysik, University of Göttingen, Germany

Motivation and Methods

Nanodevices in operation are exposed to high temperatures, electric fields and currents. Electron beam-based characterization methods require destructive sample preparation techniques. Focused hard X-rays can penetrate deep into solids, and are therefore ideally suited for *in operando* studies. In this project, we investigate focused X-rays for *in operando* studies of nanowire devices.

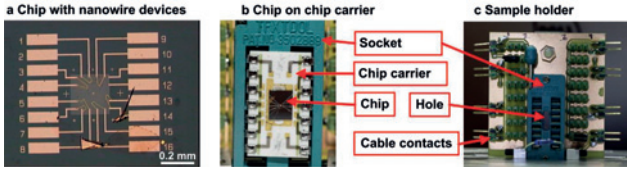

Figure 1: Sample and sample holder. ***a****, Microscope picture of chip with 8 devices.* ***b****, Photo of chip (black) glued and wedge bonded onto a chip carrier (white), mounted in socket (green).* ***c****, Photo of sample holder, seen along the X-ray beam direction: Socket (green), printed circuit board (copper). Note hole for X-ray beam.*

- Special sample holder developed, allowing simultaneous electrical and X-ray characterization of single nanodevices. Hole for X-rays to pass through.
- 100 nm-diameter InP nanowire device investigated at ID-11, ESRF.
- Rocking curves, i.e. small changes in rotation around the Bragg condition, performed at points with 100 nm distance along the nanowire axis (*z*).
- Bragg scattering collected on Maxipix pixel detector, and the direction of the scattering vector, ***q*****(*z*),** was calculated.

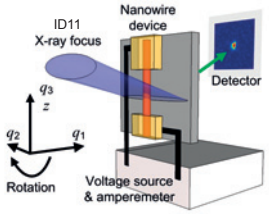

Figure 2: Experimental setup for in operando X-ray nanodiffraction of a single nanowire device at ID 11 beamline, ESRF synchrotron. *Drawing of experiment, with coordinate system for scattering vector,* ***q****. According to the Laue condition for crystals,* ***q*** *is locally equal to* ***G****, the reciprocal lattice vector.*

Nano-XRD on static device [1]

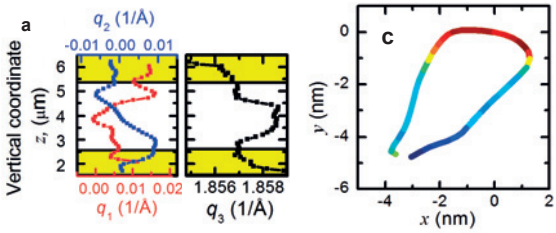

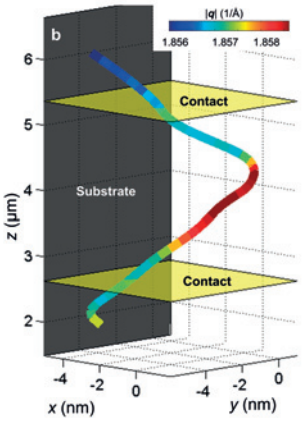

Figure 3: As-processed device. ***a****, Coordinates of* ***q****, defined in Fig. 2, vs. vertical real-space coordinate, z. Yellow boxes indicate regions which were covered by the metal contacts (determined by Au X-ray fluorescence).* ***b****, 3D reconstruction of bending of nanowire, with* $|\boldsymbol{q}|$ *used for color.* ***c****, Top view*

- The q_3 curve indicates strain in the middle of the nanowire, but is here due to a higher zincblende fraction
- The q_1 and q_2 shifts show the nanowire was bent, but are difficult to interpret.
- The nanowire is single-crystal with the (111) lattice planes orthogonal to the long axis. Since ***q*** is orthogonal to the lattice, it is tangent to the nanowire.
- The shape of the nanowire at a point *N* can be reconstructed by integration: $\boldsymbol{r}_N = \boldsymbol{r}_{N-1} + (\boldsymbol{q}(z)/|\boldsymbol{q}|)dz$
- The reconstruction shows that the nanowire made an arch above the substrate, about 7 nm high.

Nano-XRD with bias voltage [1]

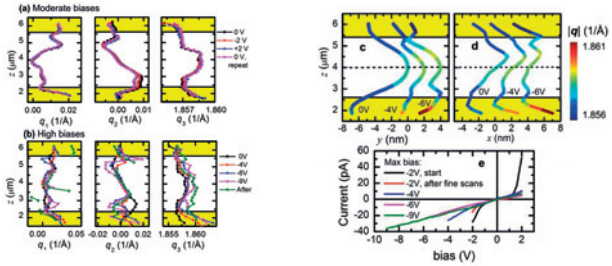

Figure 4: Structural changes correlated with changes in conductance. ***a****,* ***b****, The coordinates of* ***q*****(*z*)***, at different bias voltages.* ***c****,* ***d****, Projections along x and y, respectively, of the real-space shape reconstruction of the nanowire, as in Fig. 3, at three different biases. The -4 and -6V curves were horizontally displaced by 2 and 4 nm, respectively.* ***e****, Current vs. bias voltage, acquired after scans at different biases.*

- Measurements were then done with electrical bias (Fig. 4), which was increased in steps of 1 V until the device was destroyed at -10V.
- The reconstructions show that the arch gradually disappeared and instead bending developed in the contact regions. Strain developed in lower contact, possibly due to interfacial reactions with the metal. The middle region was relatively unchanged
- The electrical conductance decreased.

X-ray detection with nanowire [2]

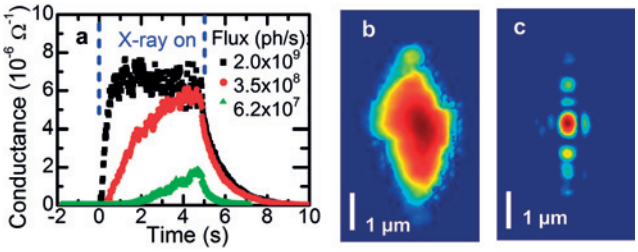

Figure 5: ***a****, Conductance of a nanowire device (different from previous figs) as a function of time, for three different X-ray fluxes. The X-ray beam was turned on at t = 0 s and turned off at t = 4.9 s.* ***b****, Image of X-ray nanofocus at P10, PETRA III, acquired by measuring current in device as function of position in a 2D raster scan.* ***c****, Ptychographic reconstruction of the same focus.*[3]

- Experiment at the P10 beamline at PETRA-III. The conductance of a nanowire device increased 5 orders of magnitude when exposed to an X-ray focus.
- By 2D scanning the device orthogonal to the beam, the nanowire device could be used as a miniature hard X-ray detector.[2]

References

[1] J. Wallentin, M. Osterhoff, and T. Salditt, "*In operando X-ray diffraction reveals electrically induced strain and bending in single nanowire device*" Advanced Materials 28 (9), 1788 (2016)
[2] J. Wallentin, M. Osterhoff, R. N. Wilke, K.-M. Persson, L.-E. Wernersson, M. Sprung, and T. Salditt, "*Hard X-ray detection using a single 100 nm-diameter nanowire*" Nano Lett. 14 (12), 7071 (2014)
[3] R. N. Wilke, J. Wallentin, M. Osterhoff, D. Pennicard, A. Zozulya, M. Sprung, and T. Salditt, "*High-flux ptychographic imaging using the new 55 mm pixel detector Lambda based on the Medipix3 readout chip*" Acta Crystallogr. Sect. A A70 (6), 552 (2014)

Acknowledgements

All nanowires were supplied by the groups of Magnus Borgström, Lars Samuelson and Lars-Erik Wernersson at Lund University, Sweden. We thank Jon Wright, ID11, ESRF, and Michael Sprung, P10, Petra-III, for excellent support, and Claes Thelander for chip carriers. Financial support by the K.A. Wallenberg Foundation and Sonderforschungsbereich (SFB) 755 'Nanoscale Photonic Imaging' of the Deutsche Forschungsgemeinschaft is gratefully acknowledged.

LU-ESS-MAXIV Collaboration on material mechanics and small-angle x-ray and neutron scattering

Jonas Engqvist[1], Matti Ristinmaa[1], Andrew Jackson[2], Tomás Plivelic[3] and Stephen Hall[1]
[1]Division of Solid Mechanics, Lund University, PO Box 118, 221 00 Lund, Sweden
[2]European Spallation Source AB, PO Box 176, 221 00 Lund, Sweden
[3]MAX IV Laboratory, Lund University, PO Box 118, 221 00 Lund, Sweden
e-mail: jonas.engqvist@solid.lth.se

Project summary

The project will establish collaboration between researchers in Solid Mechanics, at Lund University, and in Small Angle X-Ray/Neutron Scattering (SAXS/SANS) at ESS and MAXIV with a focus on increasing the knowledge of the multi-scale deformation behavior of polymeric materials. Furthermore, the collaboration will establish a foundation for the development of future joint research between the partners using SAXS and SANS at MAXIV and ESS to study the mechanics of materials.

Project goal

The central goal of the project is to establish and/or strengthen collaboration around material mechanics and small-angle scattering with x-rays and neutrons between researchers at ESS, MAXIV and Lund University.

The scientific objective of this project is to gain new insight into the nano- and micro-structural evolution of nano-structured polymers, during heterogeneous deformation. As a tool for analysing previously acquired data, the software SasView is used. Within this project, new or more detailed models will be implemented in SasView and the goal is to be able to do 2D data fitting. The polymer used during the project is a linear triblock copolymer based on polystyrene and poly(ethylene-co-butylene) (SEBS) with varying styrene/rubber content. SEBS is a well-known thermoplastic elastomer, used as e.g. dielectric actuators [1].

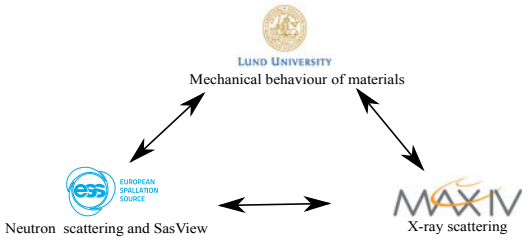

Experimental setup

Multi-scale deformation experiments has been conducted on the I911-SAXS beamline at the MAX IV Laboratory. The experiments involved continuous uniaxial loading of polymer specimen in-situ during SAXS or WAXS measurements. During the experiments, the mesoscopic deformation of the specimen was measured using 3D-surface digital image correlation (DIC) calibrated for stereo vision. The same experimental setup has previously been successfully used to study the multi-scale behaviour of glassy polycarbonate [2,3] .

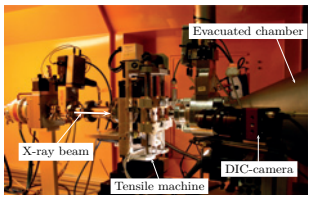

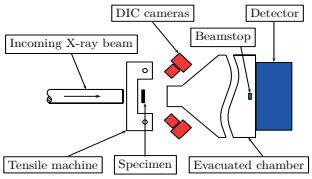

X-ray scattering

Small angle X-ray scattering (SAXS) measurements were carried out using a wavelength of 0.91 Å and an approximate q-range of 0.08 to 4 nm^{-1}. The local scattering from the sample was mapped at several points along the centreline of the specimen. The scattered X-rays were recorded using a Pilatus 1 M (Dectris) 2D hybrid pixel detector and analysed using an in-house developed program. 1D radial profiles (I(q) vs q) were extracted from the 2D scattering patterns. These 1D radial profiles were then analysed using SasView.

Macroscopic load curve

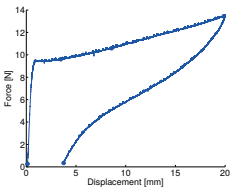

Increasing macroscopic load

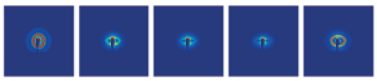

Cylinder model

A model describing the scattering intensity from cylindrical objects in a hexagonal lattice structure, described in [4], was implemented in SasView. The model takes into account particle size (radius R and length L) distributions and lattice point deviations (a), domain size ($D=2\pi/\delta$) and peak shape (L_{hkl}). The current model does not take into account any orientation of the scattering intensity, this will however be considered in the future. Some of the key equations of the model are summarised below.

Scattering intensity:

$$I(q) = I_0 P(q) S(q)$$

Form factor:

$$P(q) = \langle F_{d\|}^2(L,q)\rangle \langle F_{d\perp}^2(R,q)\rangle$$

Structure factor:

$$S(q) = 1 + \beta(q)(Z(q) - 1)G(q)$$

$$\beta(q) = \frac{\langle F_{d\perp}(R,q)\rangle^2}{\langle F_{d\perp}^2(R,q)\rangle}$$

Lattice factor:

$$Z(q) = \frac{(2\pi)^{d-1} c}{n v_d \Omega_d q^{d-1}} \sum_{\{hkl\}} m_{hkl} f_{hkl}^2 L_{hkl}(q)$$

Peak shape:

$$L_{hkl}(q) = \begin{cases} \dfrac{1}{\pi} \dfrac{\delta/2}{(q - q_{hkl})^2 + (\delta/2)^2} & \text{(Lorentzian)} \\ \dfrac{2}{\pi\delta} \exp\left[-\dfrac{4(q - q_{hkl})^2}{\pi\delta}\right] & \text{(Gaussian)} \end{cases}$$

Debye-Waller factor:

$$G(q) = \exp\left[-\sigma_a^2 a^2 q^2\right]$$

SasView will be extended with models for lamellae and cubic phase structure, as time permits.

SasView

SasView is a Small Angle Scattering Analysis Software Package, originally developed as part of the NSF DANSE project under the name SansView, now managed by an international collaboration of facilities. The aim of the SasView project is to provide open source, collaboratively developed software for the analysis of small angle scattering data [5]. The model describing hexagonally packed cylinders described above was implemented as a custom model in SasView. The model fitting and the interpretation of the results are in progress.

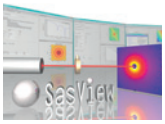

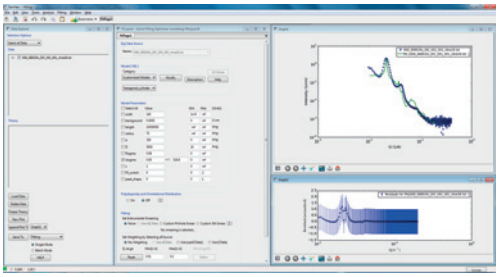

References

[1] Helal, E., Demarquette, N.R., Amurin L.G., David, E., Carastan, D.J., Fréchette, M., Polymer, 64, 139-152, 2015.
[2] Engqvist, J., Hall, S., Wallin, M., Ristinmaa, M. and Plivelic, T., Experimental Mechanics, 54, 1371–1383, 2014.
[3] Engqvist, J., Hall, S., Wallin, M., Ristinmaa, M. and Plivelic, T., Polymer, 82, 190-197, 2016.
[4] Förster, A. et al., Journal of Physical Chemistry B, 109, 1347-1360, 2005
[5] SasView for Small Angle Scattering Analysis, September 2016, URL http://http://www.sasview.org/

Acknowledgement

The financial support from the European Regional Development Fund Interreg Öresund-Kattegat-Skagerrak, reference number LU-003, is greatly acknowledged. We also acknowledge the MAX IV Laboratory for providing the beamtime (proposal 20140486) and Gerson Mantovani and Danilo Carastan from the Federal University of ABC, SP-Brazil for providing us with the SEBS samples.

Size dependent two-photon absorption cross-section of $CsPbBr_3$ perovskite quantum dots

Junsheng Chen[1,], Pavel Chábera[1], Maria E. Messing[2], Kaibo Zheng[1], Tõnu Pullerits[1]*

[1] Chemical Physics and NanoLund, Lund University, P.O. Box 124, 22100 Lund, Sweden

[2] Solid State Physics and NanoLund, Lund University, Box 118, 22100 Lund, Sweden

**junsheng.chen@chemphys.lu.se*

NANO LUND
AT THE FOREFRONT OF NANOSCIENCE

LUND UNIVERSITY

1. Introduction

Recently perovskite $CsPbBr_3$ quantum dots (QDs) have been reported as an attractive two-photon induced emission material, which can be used for two-photon-pumped lasing, three-dimensional material micro-fabrication, information technology and bio-imaging. Large two-photon absorption (TPA) cross-section is a critical parameter for the application of this QDs. However, recently reported TPA cross-sections of $CsPbBr_3$ QDs differ by over one order of magnitude for the same material. Such difference can stem from various reasons. It might be ascribed to differences in one photon linear absorption (OPLA) cross-sections or the size of QDs. In this work, we report an in-depth study of the two photon absorption (TPA) properties of $CsPbBr_3$ QDs with mean size *d* ranging from 4.6 nm to 11.4 nm by using femtosecond transient absorption (TA) spectroscopy.

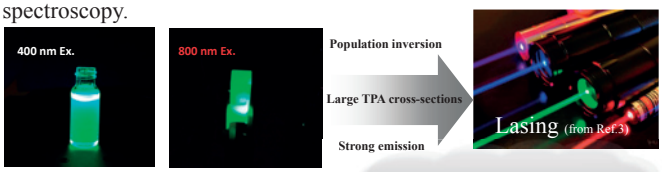

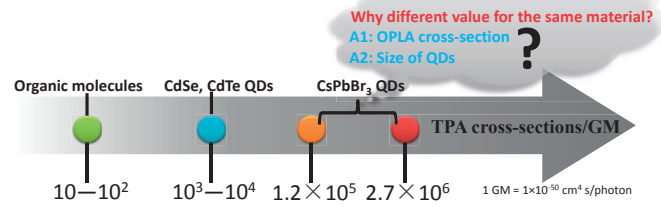

2. Experiment

QDs preparation:

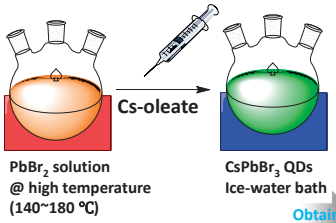

Transient Absorption Spectroscopy

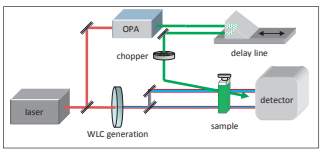

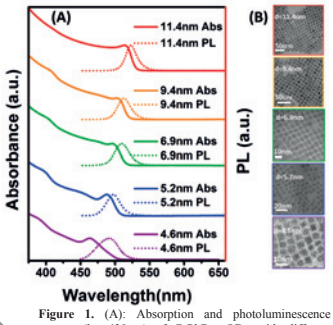

Figure 1. (A): Absorption and photoluminescence spectra (λ_{ex}=430nm) of $CsPbBr_3$ QDs with different sizes. (B) High-resolution transmission electron microscopy (TEM) images.

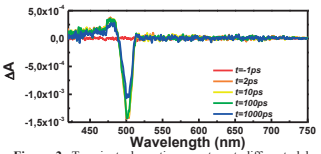

Figure 2. Transient absorption spectra at different delay time of $CsPbBr_3$ with average size 9.4 nm, excitation intensity: 0.74×10^{12} photons/cm² per pulse, excitation wavelength: 400nm.

3. Results

OPLA cross-section $\sigma^{(1)}$

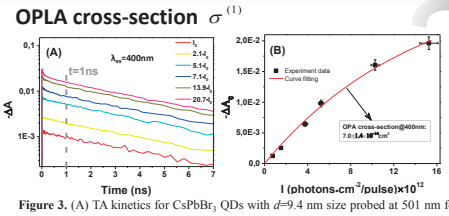

Figure 3. (A) TA kinetics for $CsPbBr_3$ QDs with *d*=9.4 nm size probed at 501 nm for the seven pump intensities, I_0=0.74×10¹² photons/cm² per pulse. (B) TA signal ΔA_0(I) rescaled from t≥1ns (see Figure 3A) as a function of excitation intensity.

Agree with analytic expression:

$$\varepsilon_{335} \approx (0.052 \pm 0.002)\times 10^{-6} d^3$$

$$[\varepsilon_{335}] : cm^{-1}M^{-1}$$

d: QDs size in nm

TPA cross-section $\sigma^{(2)}$

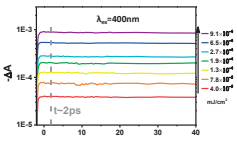

Figure 4. TA kinetics for $CsPbBr_3$ QDs with d=9.4 nm size probed at 501 nm for the seven excitation fluences.

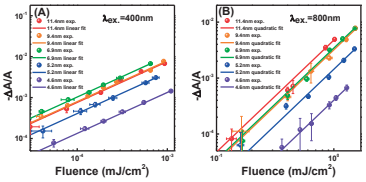

Figure 5. Excitation fluence dependent ground state bleaching (GSB) signal for $CsPbBr_3$ QDs with different size (log-log scale). GSB signals have been taken from early-time (t~2ps). A: 400nm excitation; B: 800nm excitation.

Figure 5. (a): Plot of $\sigma^{(2)}$ (1 GM= 10^{-50} cm⁴ s/photon) versus QDs size *d* (average of length and width of QDs) in a log-log scale. (b) Schematic diagram of the mechanism of TPA in $CsPbBr_3$ QDs.

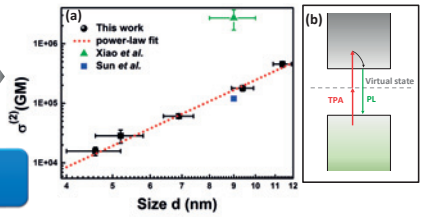

4. Conclusion

- Divergence of reported TPA cross section might emerge from uncertainty in OPLA cross-section.
- TPA process in $CsPbBr_3$ QDs proceeds through a virtual level and the final state is an exciton band state and not a defect state.

Further Experiment plan

- Revealing conformation of the organic cations in organometal halide perovskite nanoparticles by neutron-diffraction.

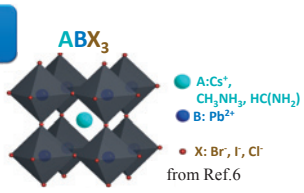

from Ref.6

- Revealing the formation process of perovskite nanoparticles by in-suit EXAFS and in-suit XRD.

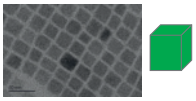

- Understanding the photo-degradation process of perovskite nanoparticles by in-suit EXAFS and in-suit XRD.

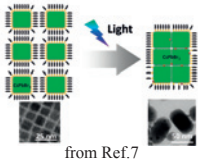

from Ref.7

Acknowledgement:

ESS & MAX IV: Cross Border Science and Society

Reference:

[1] Xiao, M., et al. (2016). Journal of the American Chemical Society 138(11): 3761-3768.
[2] Sun H. D., et al. (2016). Nano Letters 16(1): 448-453.
[3] http://titaniumphysicists.brachiolopemedia.com/2015/04/01/episode-55-laser-laser-laser-laser-laser-laser-with-aaron-fischer/
[4] Chris Xu and Watt W. Webb. (1996). J. Opt. Soc. Am. B/Vol. 13, No. 3/March 1996.
[5] Dakovski, G. L. and J. Shan (2013). Journal of Applied Physics 114(1).
[6] Zhang, W., et al. (2016). Advanced Materials 28(21): 4040-4046.
[7] Chen, J. S., et al. (2016). Science China Materials: DOI: 10.1007/s40843-016-5123-1.

Effects of Bile Salt Sodium Glycodeoxycholate on the Self-Assembly of PEO-PPO-PEO Triblock Copolymer P123 in Aqueous Solution

Solmaz Bayati, Luciano Galantini*, Kenneth D. Knudsen & Karin Schillén**

Division of Physical Chemistry, Department of Chemistry, Lund University, P.O. Box 124, SE-221 00 Lund, Sweden
* Department of Chemistry, "Sapienza" University of Rome, P. le A. Moro 5, 00185 Rome, Italy
** Institute for Energy Technology, P.O. Box 40, NO-2027 Kjeller, Norway

Introduction

Bile acid diarrhea is caused by the malabsorption of bile acids at the end part of the small intestine in human body. The aim of this study is to investigate the possibility of using a group of nonionic triblock copolymers, Pluronics instead of present sequestrants in the treatment of this disease. Pluronics have been widely used in biomedical applications due to their tunable phase behavior in aqueous solutions, biocompatibility and non-toxicity. In this work we studied the effects of a bile salt sodium glycodeoxycholate (NaGDC) on the association behavior of P123 ($EO_{20}PO_{68}EO_{20}$) in aqueous solution by means of dynamic and static light scattering (DLS/SLS), small angle X-ray and neutron scattering (SAXS/SANS) and differential scanning calorimetry (DSC).

Materials

NaGDC
Sodium glycodeoxycholate

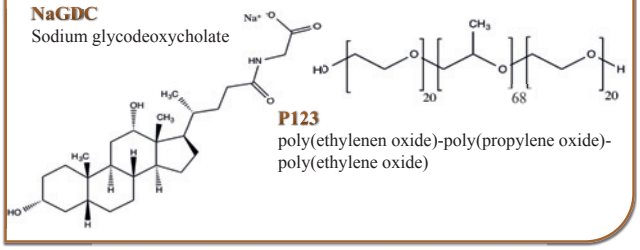

P123
poly(ethylenen oxide)-poly(propylene oxide)-poly(ethylene oxide)

Dynamic & Static Light Scattering (DLS/SLS)

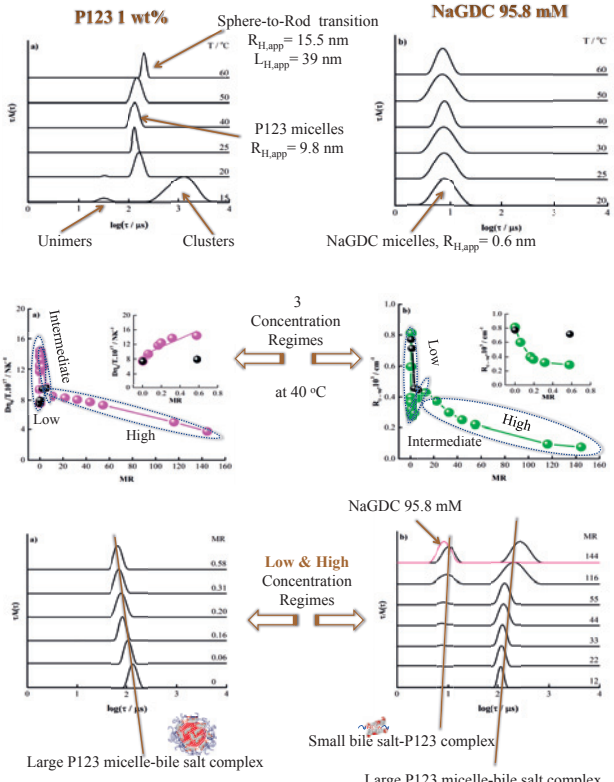

Differential Scanning Calorimetry (DSC)

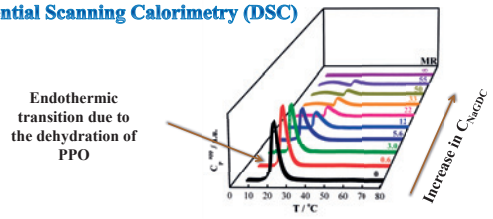

C_{NaGDC} / mM	C_{P123} / mM	MR	T_{onset} / °C	T_m / °C	ΔH_m / kJ mol^{-1}
0	1.74	0	17.6	20.7	426
1.02	1.74	0.6	17.6	20.2	420
5.14	1.74	3.0	17.8	19.3	336
9.80	1.74	5.6	19.5	20.4	270
21.5	1.74	12	21.5	23.6	171
38.9	1.73	22	24.1	25.8	102
57.5	1.74	33	25.7	27.8	78
87.1	1.73	50	27.7	29.9	50
95.2	1.74	55	28.5	30.5	41
200	1.72	116	32.2	34.8	18
250	1.73	144	32.9	35.1	4.5

By addition of NaGDC to the P123 solution:

- P123 micelles form at higher temperatures
- Ethalpy of micelle formation decreases
- P123 micelles start to decompose

Small Angle X-Ray & Neutron Scattering (SAXS/SANS)

P(q): Spherical Core-Shell Model
S(q): Hayter-Penfold Model

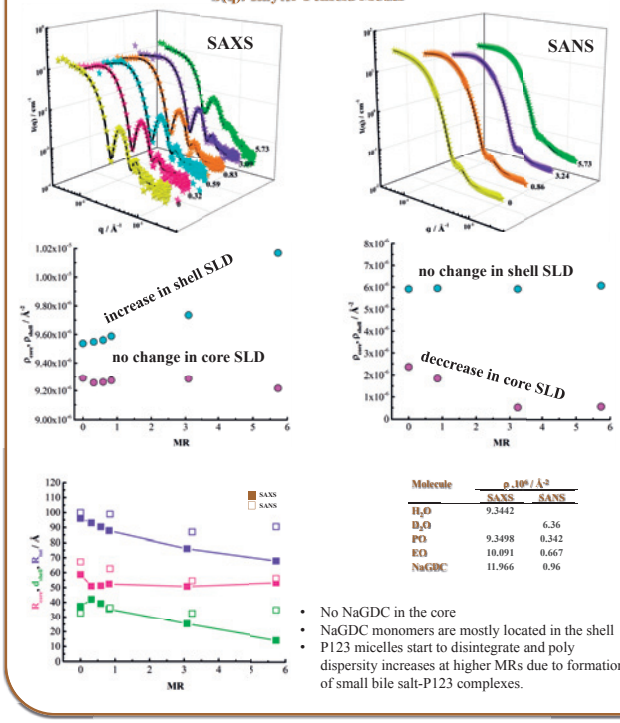

Molecule	$\rho \cdot 10^6$ / Å^{-2} SAXS	SANS
H_2O	9.3442	
D_2O		6.36
PO	9.3498	0.342
EO	10.091	0.667
NaGDC	11.966	0.96

- No NaGDC in the core
- NaGDC monomers are mostly located in the shell
- P123 micelles start to disintegrate and poly dispersity increases at higher MRs due to formation of small bile salt-P123 complexes.

Conclusion

- DLS/SLS, SAXS/SANS & DSC measurements confirm the interaction of bile salt with the P123
- At 40 °C:
  at low MRs: larger P123 micelle-bile salt complexes
  bile salt monomers occupy the shell
  at high MRs : coexistance of larger P123 micelle-bile salt complexes & bile salt-P123 complexes with one or several P123 chains.

Acknowledgement

Gerd Olofsson (1936-2014) , Caroline Anderberg Haglund & Hanna Bergenholtz, Lund University, Sweden.
The Swedish research Council, The Linnaeus Grant Organizing Molecular Matter, Knute and Alice Wallenberg Foundation.

References

1. Schmolka, i. R., *J. biomed. Mater. Res. 1972, 6, 571-582.*
2. Malmsten, M., Eds. Elsevier science SV: Amsterdam, 2000; p 319.
3. Batrakova, E. V., Kabanov, A. V., *J. Control Release 2008, 130, 98-106.*
4. Bayati, S., Galantini, L., Knudsen, K. D., Schéllen, K., *submitted.*

NcNeutron – Norwegian Center for Neutron Research

Magnus H. Sørby [a], Stefano Deledda [a], Christoph Frommen [a], Geir Helgesen [a], Isabel Llamas-Jansa [a,b] Kenneth Knudsen [a], and Bjørn C. Hauback [a]

[a] Institute for Energy Technology, Physics Department, P.O. Box 40, NO-2027, Kjeller, Norway

[b] European Spallation Source ESS AB - Box 176, 22100 Lund, Sweden

The JEEP II reactor

The JEEP II reactor (2 MW thermal power) at the Institute for Energy Technology (IFE) in Kjeller (Norway) is presently the only neutron source in the Nordic Countries. A national infrastructure project to upgrade the neutron scattering facilities, ***NcNeutron***, is currently running (2016-2020). The neutron lab currently consist of 3 powder diffractometer (PUS, DIFF and ODIN; the latter in final stage of construction), small angle neutron scattering (SANS), a test station for ESS and a neutron radiography setup. The upgrade will include an *improved cold moderator*, construction of a *neutron reflectometer*, improved instrumentation for *neutron radiography* and rebuilding the PUS diffractometer for *residual stress measurements*.

Powder Diffractometer PUS (operational)

Main Application

Complex inorganic materials (hydrogen storage materials, oxides, ...)

Specifications

Take-off angle	55° - 98°, typical 90°
Wavelengths	0.732 – 2.575 Å, typical 1.55 Å
α_1-collimation	15'
Total 2θ-range	2° - 132° (corresponding to 0.88 – 44.1 Å @ 1.55 Å)
Monochromator	vertically focusing, 16' mosaicity horizontally Germanium, cut parallel to (5 1 1) plane
Flux at sample	2.5×10^4 n/(cm²s) (90° take-off)
Detector	2 detector banks with 7 ^{3}He, each covering 20°
Resolution	$\Delta d/d = 3 \times 10^{-3}$ for d = 1 Å

Sample Environment

Temperature	9 – 1300 K
Pressure	up to 8 bar

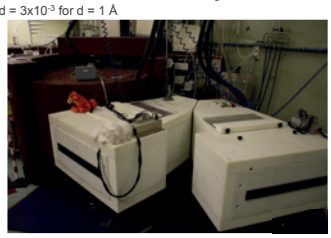

SANS (operational)

Main Applications

Polymer systems and layered silicates (clays)

Specifications

Wavelength range	4.7 - 11.5 Å (Max. flux at 5.1 Å)
Momentum transfer Q	0.008 - 0.25 $Å^{-1}$ (corresp. d-value 25 - 780 Å)
Beam size at sample	Between 4.9 - 9.3 mm diameter.
Flux at sample	Maximum flux is 8.4×10^5 n/(cm²s)
Secondary flight path	Evacuated tank containing the detector
Detector	^{3}He-filled 60 cm area detector

Sample Environment

Standard: 10mm wide cuvettes, temp. control by water (0-90°C) or Silicon oil (>100°C)

Non-standard: High-T chamber (300 °C), high-pressure CO_2 cell

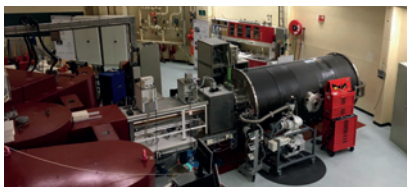

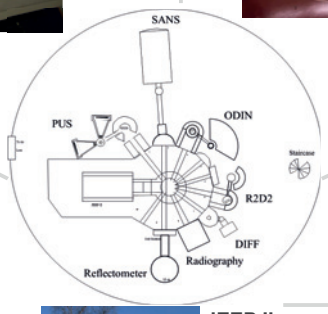

R2D2 (re-designed for detector testing)

Main Application

Detector testing (ESS); provides a monochromatic beam and floor space

Specifications

Take-off angle	90°
Wavelengths	1.121,1.540, 2.413 Å
α_1-collimation	15' and no collimation (49')
Monochromator	vertically focusing, 16' horizontal mosaicity germanium cut parallel to (5 1 1) plane
Flux at sample	1.5×10^5 n/(cm²s) (no α_1-collimation, simulated)

JEEP II reactor at IFE, 2 MW, cold source

Reflectometer (design stage)

Applications

Low-wetting or low-friction surfaces, non-corrosive material coatings, energy collecting surface layers, (components of) cell membranes

Concept

White beam «Rainbow» concept devoloped at ILL.

Full operation from mid-2020.

Radiography (design stage)

Applications

Fuel cells, hydrogen storage systems, Li-ion battereis, weldings.

Specifications

Beam size .	220 mm x 30 mm
Detector system	Scintillaotor/CCD

Full operation from end 2019.

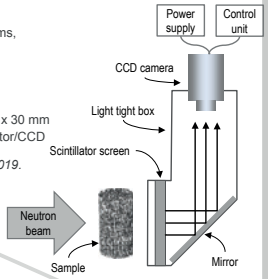

Amorphous materials diffractometer DIFF (operational)

Main Application

Liquid-like and disordered materials

Specifications

Take-off angle	25.6°
Wavelength used	1.55 Å
Filter	sapphire
Total 2θ-range	10° - 120°
Monochromator	Double focusing, pyrolytic graphite 1.25° effective mosaicity
Flux at sample	~5×10^6 n/(cm²s)
Detector	position sensitive
Resolution	low (built for high intensity)
Sample Environment	as for PUS

High-Resolution Powder Diffractometer ODIN (under construction)

Main Applications

In-situ measurements, complex inorganic materials)

Specifications

Take-off angles	75° - 120° (continuously, typical 105°)
Wavelengths	1.051 – 2.248 Å, typical 1.52 Å
α_1-collimation	12', 18' and no collimation (about 2°)
Total 2θ-range	5.6° - 146° (corresponding to 0.795 – 15.6 Å @ 1.52 Å)
Monochromator	double focusing, 16' mosaicity vertically, germanium, cut parallel to (5 3 1) plane
Flux at sample	5.4×10^5 n/(cm²s) (75° take-off, 18' α_1-collimation, simulated)
Detector	4 area detectors of 500 x 800 mm², horizontal resolution 3.8 mm
Resolution	$\Delta d/d = 1.3 \times 10^{-3}$ for d = 0.9 Å, 120°, 12' (simulated)

Simulations

Instrument optimized using analytical calculations (L. Cussen), Monte Carlo simulations (McStas and VITESS) and numerical optimization (VOP of VITESS)

Funding

NANOMAT program of the Research Council of Norway (University of Oslo and IFE)

Contact: magnus.sorby@ife.no

Silk – MnO_2 hybrid catalysts

Manish Singh,*[1] Raul Garcia,[2] Christian Gollwitzer,[2] Estera S. Dey,[1] Michael Krumey,[2] Tomas Plivelic,[3] Cedric Dicko[1]
[1]Division of Pure and Applied Biochemistry, Chemical Center, Lund University, Sweden
[2]PTB, BESSY Synchrotron, Helmoltz Centrum, Berlin, Germany
[3]MAX IV Laboratory, Lund, Sweden
*manish.singh@tbiokem.lth.se

Abstract

The production of enzyme mimic using hybrid materials of silk and metal oxides is now possible using a simple one step method. Although promising those hybrids materials, and others, suffer from lack of understanding of the organic-inorganic interface and long lasting catalytic activity. In this work, we characterize and investigate the interplay between the organic matrix of Bombyx and Tasar silks and the inorganic nanoparticles (MnO_2) by combining small angle X-ray scattering (SAXS), anomalous small angle X-ray scattering (ASAXS) and near edge X-ray absorption fine structure (NEXAFS). The selection of the tested varieties were based on previous studies (manuscript submitted).

Introduction

New multi-functional properties can be added to silk by *in situ* formation of nanoparticles using different nano-incorporation techniques. Sonication is one such technique which allows for direct synthesis and deposition of metal oxide nanoparticles in/onto textile substrate in one step.

However, such hybrid lack understanding of the organic-inorganic interface and how it mediates particle formation. The use of X-ray structural and spectroscopic methods such as SAXS, ASAXS and NEXAFS provide us with the silk fibers structural integrity (SAXS), the average size of the metal oxides (SAXS), the environment and distribution of the metal oxides (ASAXS) and the metal ion oxidation state (NEXAFS).

Fabrication of silk – MnO_x hybrid

Schematic diagram of hybrid MnO_2–Silk formation

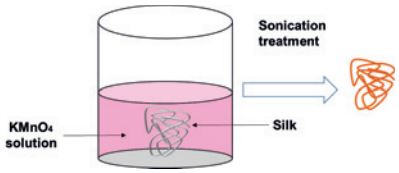

Results – SAXS of silk fiber MnO_x particle formation

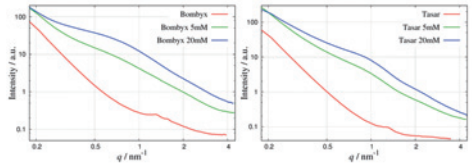

Features around q = 1 nm^{-1} shows the formation of small MnO_x particles of MnO_2 supported Bombyx and Tasar. Further, these feature increases with increase concentration of $KMnO_4$.

Oxidation state and size at the Mn-edge

Results – NEXAFS-Metal ion oxidation state

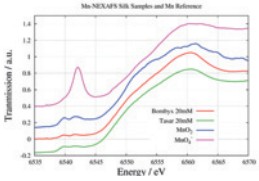

Pre-peak position of MnO_2 supported silk fibers matches with standard MnO_2. The main peak of MnO_2 supported silk fibers lies around 6560 eV and matches with the standard MnO_2.

Results – ASAXS-Size distribution of the MnO_x particle

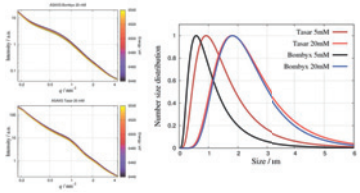

MnO_x particle feature around q = 1 nm^{-1} decreases with increase of energy for both MnO_2 supported fibers of Bombyx and Tasar.

Oxidative properties

Results – Successive oxidations of methylene blue (MB)

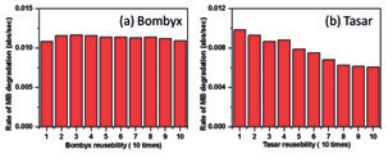

Re-usability of silk-MnO_2 hybrid: a) Bombyx mori, b) Tasar for 10 consecutive catalysis. The MB degradation rate of MnO_2 supported Bombyx and Tasar stayed relatively constant with the number of cycles.

Conclusions

- SAXS confirms the growth of MnO_x particle on Bombyx and Tasar silks.
- NEXAFS (pre-peak and main peak) confirms the formation of Mn(IV) oxide.
- ASAXS shows the decrease of MnO_x particle feature with increase in energy for MnO_2 supported Tasar and Bombyx.
- The MnO_2 -Silk fiber was successfully used and re-used (10 times) for the degradation of methylene blue.

Materials and Methods

Approximately 0.1 g of silk yarn (Bombyx, Tasar) was submerged in 10 ml of $KMnO_4$ solution (5 mM, 20 mM) in a 20 mL glass vial. Without delay the reaction mixture was irradiated with ultrasound waves for 45 min. Treated silk fibers were further characterized using SAXS, ASAXS and NEXAFS.

Acknowledgments

The research was supported by the Swedish Research Council (VR-UForsk 348-2013-6218) and Interreg MAXIVESSFUN (LU-018).

Cellulose in tetrabutylammonium acetate: from the dissolution state to spun fibers

Marta Gubitosi[a], Alexander Idström[b], Carina Olsson[b], Tobias Köhnke[c], Luigi Gentile[a], Erik Wernersson[c], BjörnStenqvist[c], Mikael Lund[c], Ulf Olsson[a].

[a] Division of Physical Chemistry, Lund University, Sweden, [b] Swerea IVF, Mölndal, Sweden, [c] Division of Theoretical Chemistry, Lund University, Sweden.

E-mail: marta.gubitosi@fkem1.lu.se

Introduction

Cellulose, the most abundant biopolymer on Earth [1], is the key material in wood, paper and textile industries. To be used as a textile fiber, cellulose has to undergo a process of dissolution in suitable solvents followed by regeneration through spinning, and the improvement of these strategies constitutes an increasingly active research field. Dissolving cellulose is however a challenge, as it is interestingly insoluble in water and in common organic solvents. Recently, solvents based on ionic liquids are attracting increasing attention [2]. Their chemical and thermal stability, low vapor pressure and recyclability have indeed made them desirable green solvents for cellulose. One recent example is tetrabutylammonium acetate (TBAAc) diluted with dimethyl sulfoxide (DMSO) in weight ratio 2:7 [3]. An insight in the dissolution state of cellulose is crucial for the evaluation of existing solvents and the development of the next generation ones. Moreover, a characterization of the structural properties of the spun fibers is needed for a better understanding of their mechanical properties.

Dissolution

Microcrystalline cellulose (MCC) has been dissolved in 2:7 TBAAc/DMSO in the concentration range 1-10 wt%. High resolution NMR and small-angle X-ray scattering (SAXS) experiments show the presence of a solvation shell around the cellulose chain of Ac^- due to hydrogen bonding and TBA^+ electrostatically bound to the anion. Molecular Dynamics simulations confirm these findings.

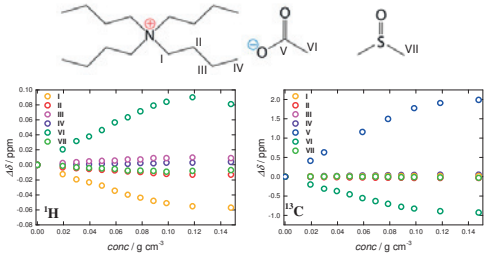

Molecular structure of TBAAc/DMSO solvent, and ^1H and ^{13}C NMR chemical shift changes with increasing cellulose concentration.

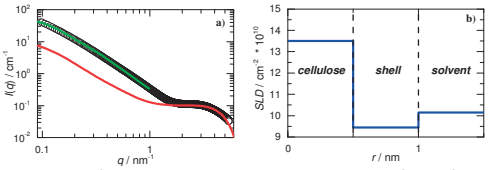

a) SAXS profile in absolute intensity and calculated curves for the form factor of a single semi-flexible cellulose chain (red) and of a fractal cluster (green) for of 10 wt% MCC in 2:7 TBAAc/DMSO. b) Scattering length density (SLD) radial profile used for the calculation of the form factor of the single chain.

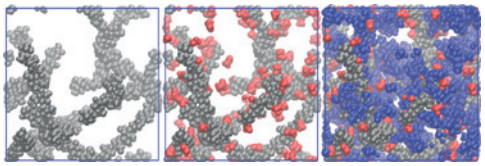

Visualization of one frame of the simulation trajectory the 2:7 TBAAc/DMSO solvent with 10 wt% cellulose. From left to right: cellulose (grey); cellulose and acetate (red); and cellulose, acetate, and TBA^+ (blue).

Spinning of fibers

Fibers have been spun from 2:7 TBAAc/DMSO solutions and coagulated in water bath. Different draw ratios (DR = 1.0, 1.2, 1.4, 1.6) have been analyzed via light microscopy and wide-angle X-ray scattering (WAXS).

1) **Dimension of the fibers**: 5-6 μm.

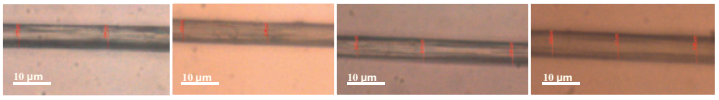

2) **Crystal structure** from **WAXS: Cellulose II**.

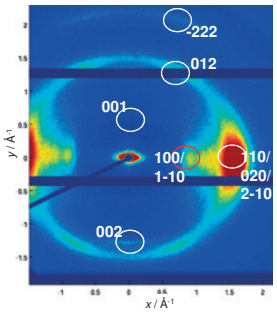

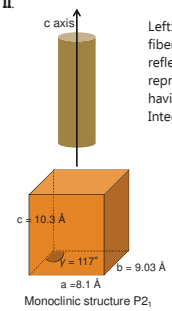

Left: diffraction pattern of regenerated cellulose fibers. The assignment of all the visible reflections is shown. Right: schematic representation of the unit cell of Cellulose II, having a monoclinic structure $P2_1$. Bottom: Integration of the diffraction patterns.

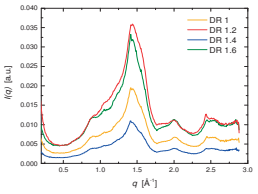

3) **Crystal orientation** from **WAXS**: order parameter $f_c \approx 0.75$ (misorientation of 15 degrees).

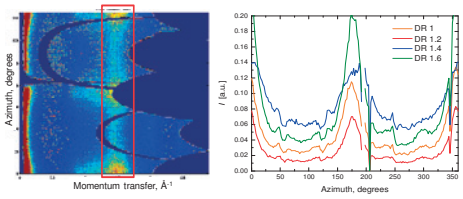

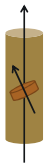

$$\langle \cos^2\varphi \rangle = \frac{\int_0^{\pi/2} I(\varphi)\cos^2\varphi \sin\varphi d\varphi}{\int_0^{\pi/2} I(\varphi)\sin\varphi\, d\varphi}$$

$$0 < f_c = \frac{3\langle \cos^2\varphi \rangle - 1}{2} < 1$$

4) **Crystal dimensions** from **WAXS**:

Scherrer equation gives the average number of planes per crystallite. The 002 reflection was selected.

$$< N > = \frac{q_{max}}{\Delta q}$$

The crystallites were found to be from 11 to 25 nm long.

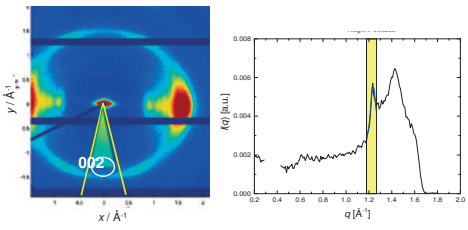

References

[1] D. Klemm, B. Heublein, H. P. Fink, A. Bohn, *Angew. Chem. Int. Ed. Eng.*, **2005**, *44*, 3358.
[2] R. P. Swatloski, S. K. Spear, J. D. Holbrey, R. D. Rogers, *J. Am. Chem. Soc.*, **2002**, *124*, 4974.
[3] J. Miao, H. Sun, Y. Yu, X. Song, L. Zhang, *RSC Adv.*, **2014**, *4*, 36721.

Characterization of cation ordering, oxygen vacancy distribution, and proton sites in *hexagonal* and *cubic* $BaTi_{1-x}Sc_xO_{3-\delta}$

N. Torino[1], P. F. Henry[2], S. M. H. Rahman[1], C. S. Knee[1], S. G. Eriksson[1], S. T. Norberg[1], T. S. Bjørheim[3], R. Haugsrud[3], S. Callear[4], R. Smith[4]

[1]Chalmers University of Technology, Gothenburg, Sweden
[2]European Spallation Source ERIC, Lund, Sweden
[3]University of Oslo, Norway
[4]Science and Technology Facilities Council, Didcot, UK

Interreg Öresund-Kattegat-Skagerrak European Regional Development Fund
EUROPEAN UNION

Over 30 years of research indicate that perovskite (and perovskite-like) materials are a valid choice for developing solid-state protonic conductors

- *cubic ones provide a regular framework of oxide ions*
- *wide choice of potential systems*
- *ability to tune properties with appropriate doping strategies*

BCY and BZY are considered the most promising materials

- *enhanced performance via densification and mixed compositions*

still looking for novel phases!

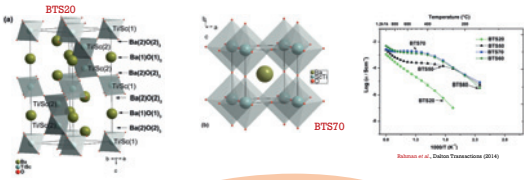

Background: barium titanate systems

$Ba_2(In_{1-x}Ti_x)_2O_{5+x}\square_{1-x}$ phase

- structural transitions with increasing x: brownmillerite to tetragonal, to disordered cubic perovskite for $0.15 < x < 0.75$
  Jayaraman et al., Solid State Ionics 170 (2004) 17
- significant proton conductivity levels, for $x = 0.2$, $\sigma = 10^{-3}$ S/cm at 450°C, under wet N_2
  Queres et al., J of Power Sources 195 (2010) 1136

$BaTi_{0.5}In_{0.5}O_{3-\delta}$

- increased acceptor dopant concentration does not mean higher conductivity, hydration levels remain low
  Rahman et al., Int J of Hydrogen Energy 37 (2012) 7975
- RMC suggests regular InO_6, and distorted TiO_6, with off-centred Ti^{4+}, impacting on proton mobility
  Norberg et al., J of Phys: Condens Matter 23 (2011) 435214

$BaTi_{0.5}Sc_{0.5}O_{3-\delta}$ *Rahman et al., Solid State Ionics 225 (2014) 140*

- cubic Pm-3m perovskite
- close to unitary t_{H^+} for T < 500°C, $\sigma_{tot} > 10^{-4}$ S/cm in T range 400-800°C
- wide IR band suggests a range of hydrogen bond strengths

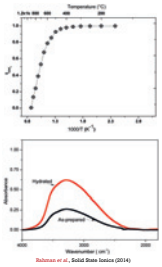

Rahman et al., Solid State Ionics (2014)

$BaTi_{1-x}Sc_xO_{3-\delta}$ $(0.1 \leq x \leq 0.8)$ *Rahman et al., Dalton Transactions 43 (2014) 15055*

- polymorphic solid solution: hexagonal *6H* perovskite for $x \leq 0.2$, cubic *Pm-3m* perovskite for $0.5 \leq x \leq 0.8$
- remarkable difference in conductivity for hexagonal and cubic samples
- XRD suggests different oxygen vacancy ordering

unsolved questions

- Any oxygen vacancies and/or cations ordering?
- When hydrated, where are the protons?
- Why a structural transition, as Sc content increases?
- Can the poorer protonic conduction for the 6H be explained?

Neutron Powder Diffraction! at 5K and RT

D2B - Institut Laue Langevin, Grenoble

- Single large batches of $BaTi_{1-x}Sc_xO_{3-\delta}$ synthesised (with x = 0.2, BTS20; and x = 0.7, BTS70)
  - Solid state reaction
- Each batch split into 3 sub-batches for NPD
  - Vacuum dried
  - Hydrated with water
  - Hydrated with deuterated water
- Precharacterised with X-ray (+ synch. X-ray), TGA

results

BTS70 vacuum dried

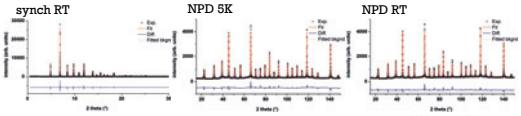

- Synchrotron X-ray confirms cubic *Pm-3m* – no lower symmetry
- Vacuum dried sample – no phase transition on cooling
- no obvious long range Sc/Ti site ordering
- Single O site – no obvious oxygen vacancy long range ordering

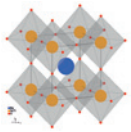

BTS20 vacuum dried

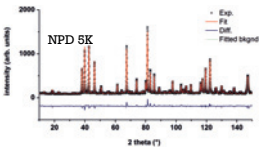

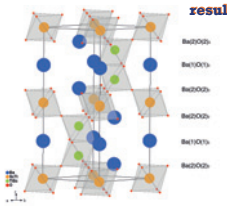

results

- Synchrotron X-ray confirms 6H type ($P6_3/mmc$) – no lower symmetry
- Vacuum dried sample – no phase transition on cooling
- Clear Sc/Ti site ordering (>95% Sc on *2a* site)
- Clear oxygen vacancy preference for O1 (the face sharing Oh site, *6h*)
  - agrees with *Sinclair et al., J Mater Chem 9 (1999) 1327*

protons are more localised in 6H structure!

protonic defect prefers O in face-sharing polyhedra by 80 kJ/mol

Bjørheim et al., Inorg Chem 54 (2015) 2858
more favourable hydration thermodynamics with increasing Sc content (cubic phase)
$\Delta_{hyd}H^0 = -83 \pm 2$ kJ/mol BTS70

retention of protonic defects at high T for hexagonal phase
$\Delta_{hyd}H^0 = -108 \pm 2$ kJ/mol BTS20

BTS70 hydrated

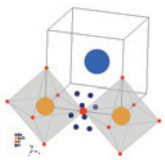

- H site located on *24k* site
- O site occupancy factor > 95%
- Structure is disordered
- Clear evidence of diffuse scattering

H position in agreement with DFT!
also *Ahmed et al., J of Alloys and Compounds 450 (2008) 103*

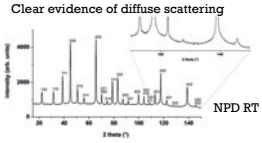

BTS20 hydrated

- O1 occupancy increases upon hydration
- H site located on *12j* site, adjacent to O1 site
- Sc/Ti cations are ordered
  - Sc and Ti share *2a* sites
  - Ti is found in *4f* sites

Sc/Ti ordering, O vacancy, and H position from experiment agree with DFT!

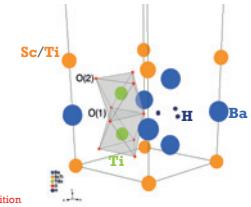

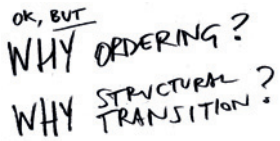

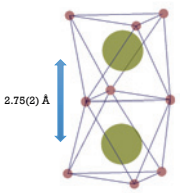

Sc does not adopt such a dimeric arrangement!

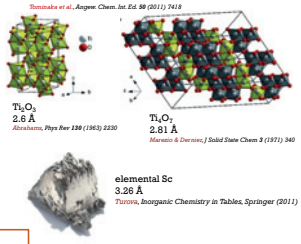

The testbeamline of the European Spallation Source

R. Woracek[1], M. Wedel[1], J. Taylor[1], K. Habicht[2], K. Andersen[1], M. Strobl[1]

[1]European Spallation Source, ESS ERIC, Lund, Sweden, [2]Helmholtz Zentrum Berlin, Germany

Introduction

- ESS operate s a testbeamline (TBL) and the BERII research reactor at Helmholtz Zentrum Berlin
- The TBL provides the **ESS pulse structure** (14Hz, 2.86ms) and option of pulse shaping by **W**avelength **F**rame **M**ultiplication (WFM)

Chopper mimics the ESS time structure

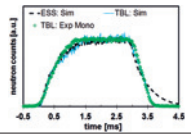

Goals:

- Experimental test case for "long pulse"-instrumentation with **flexible setup**
- Develop/establish procedures and data reduction before ESS is built: **Integrate** and test **software** (control software, data streaming, data reduction, data analysis,…) and **hardware** components (detectors, polarizers, choppers, collimators, …)
- **Method/concept development:** Tailored to exploit ESS time structure, e.g. WFM diffraction, WFM imaging, Larmor encoding in time-of-flight operation, MIEZE, Multi-SANS, Modulated-Intensity-SANS, TOF imaging, …
- Support projects with ESS involvement (such as Interreg) with experimental data (provide 'user feedback' for e.g. software development at the same time)

Setup

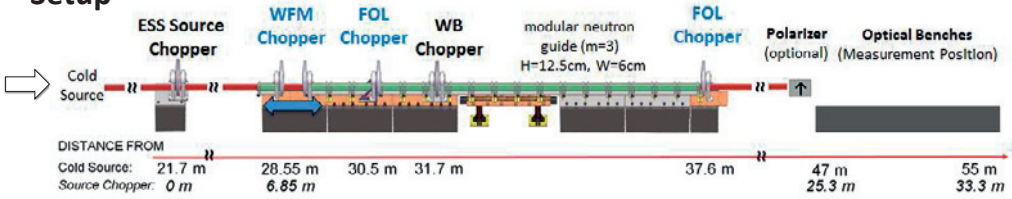

Available Detectors:

- ^{3}He Beam Monitors, ^{3}He multi-tube detector
- ^{3}He 2D-ToF detector (30cm x 30cm; 2mm spatial resolution)
- CCD imaging camera
- Availability of MCP based ToF imaging devices based on collaborations (55µm pixel)

Miscellaneous:

- Polarized beam (2Å - 10Å)
- Motorized slits, positioning systems, power supplies, I/O controls

2 main modes

Single Pulsed mode
2 double choppers
low resolution
(4%-20%)

WFM mode
2 double choppers
4 single disc choppers
high resolution
(0.5%-2%)

ToF to wavelength conversion using WFM

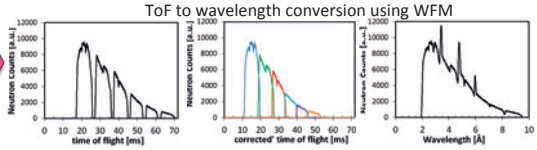

Examples of Method Development

WFM Diffraction

- WFM is fundamental to several ESS instruments: Experimental setup and data reduction require development that is being performed at the TBL
- WFM diffraction is being used to study Ti-6Al-4V alloys produced by additive manufacturing as part of Interreg project (MAH-003)

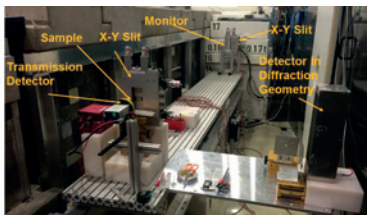

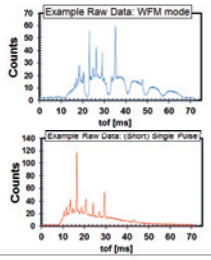

Spin Echo Modulated Small Angle Neutron Scattering

SEMSANS is a new technique to measure small angle scattering with beam modulated through spin-echo approach, providing 2D images

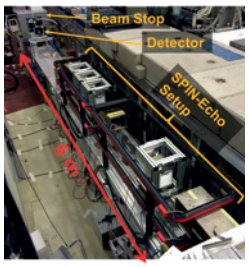

- Takes advantage of ToF
- Initial results obtained at TBL reveal differences across metallic welds

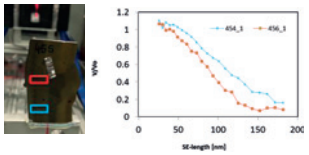

Reference: R. Woracek, T. Hofmann, M. Bulat, M. Sales, K. Habicht, K. Andersen, M. Strobl, *The testbeamline of the European Spallation Source – instrumentation development and wavelength frame multiplication*, Nucl. Instr. Meth. Phys. Res. A, (2016), Available online 17 September 2016

ACCESS CONTACT: Dr. Robin Woracek
E-mail: robin.woracek@esss.se
Mobile (Germany): +49 (0) 176 4735 9833
Mobile (Sweden): +46 (0) 721 79 23 26

europeanspallationsource.se

Relation between Faults, Residual Stresses and Microstructure in Railway Switches and Crossings

Somrita Dhar
DTU Wind Energy

Hilmar K. Danielsen
DTU Wind Energy

Johan Ahlstrøm
Chalmers Railway Mechanics

Background

Switches and crossings are an integral part of any railway network. Wear, plastic deformation and rolling contact fatigue due to repeated passage of trains cause severe damage to the rail crossing nose. Rolling contact fatigue causes surface and sub-surface cracks on the rails which finally result in rail failure. Residual stresses play a vital role in the growth rate of cracks. The knowledge of internal stress distribution can help to better understand the crack propagation rate and prevent catastrophic rail failures.

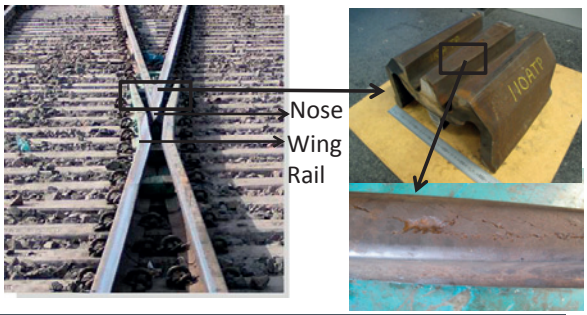

Scope of Work

The present study is a cooperation between DTU, Chalmers and BaneDanmark which aims to find the residual stress distribution at different locations by synchrotron radiation as well as laboratory X-ray measurements. A 2D stress mapping on the transverse surface of the rail and its effect on work hardening will be studied. From the nature of the stresses obtained, a study on the crack propagation path can be made.

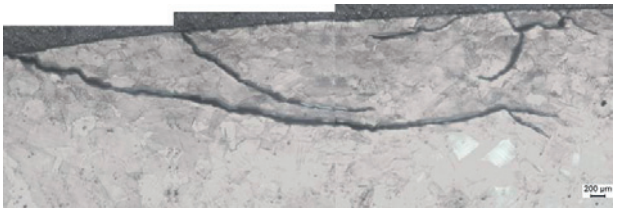

Microstructure and Hardness

The running surface of the nose experiences severe plastic deformation and work hardening. A work hardened gradient is formed with extreme high hardness on the surface of around 600 Hv which gradually decreases to a base hardness of around 220 Hv along a depth of 8mm. Most of the surface cracks observed in the microstructure were in the high hardened top layer.

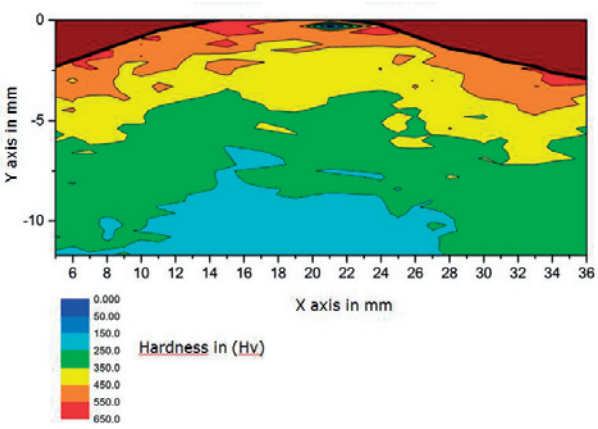

Residual Stress Measurements

Laboratory X-Ray stress measurements made on the running surface of the nose on two different locations (near the crack and gauge corner) clearly indicate a difference in stress distributions at these two points which may have affected the formation as well as propagation of the crack.

Location	Surface head	Gauge corner
Sigma 11 (MPa)	3,62	-76,42
Sigma 22 (MPa)	-174,46	-107,59
Angle(Phi)	-54	-10

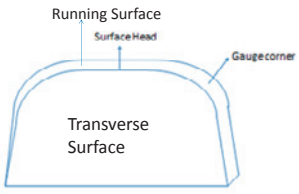

Synchrotron Measurements

Synchrotron radiation stress measurements were made on the transverse section at different depths. Tensile stresses were obtained in the direction normal to the transverse face, unlike compressive in-plane stresses as in case of the running surface .

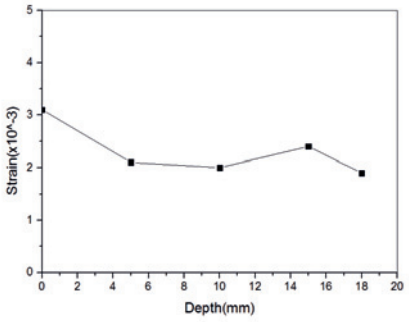

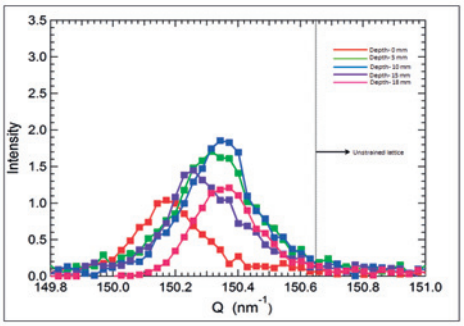

Femtosecond tracking of structure and spin

T. Harlang[1,2], K. Kjær[1,2,3], D. Leshchev[4], J. Uhlig[2], K. Haldrup[1], K. Gaffney[3], M. Wulff[4], P. Persson[2], K. Wärnmark[5], V. Sundström[2], M. Nielsen[1] et al.

[1]Department of Physics, Technical University of Denmark, Fysikvej 307, DK-2800 Kongens Lyngby, Denmark
[2]Department of Chemical Physics, Lund University, P.O. Box 12 4, 22100 Lund, Sweden
[3]PULSE Institute, SLAC National Accelerator Laboratory, Menlo Park, California 94025, USA
[4]European Synchrotron Radiation Facility, Grenoble Cedex 38043, France
[5]Centre for Analysis and Synthesis, Department of Chemistry, Lund University, Box 124, Lund SE-22100, Sweden

Summary

Molecular reactions are dependent on nuclear motions which occur on the femtosecond timescale. In pump/probe experiments, a molecular process is initiated by one light pulse, and probed by another. By probing with x-rays, information about the electronic configuration can be gained from the emission signal and structural information can be extracted from the scattering. These techniques can be used in parallel at synchrotrons and x-ray free electron lasers to study the dynamics of molecules in solution, as shown here.

X-ray emission spectroscopy

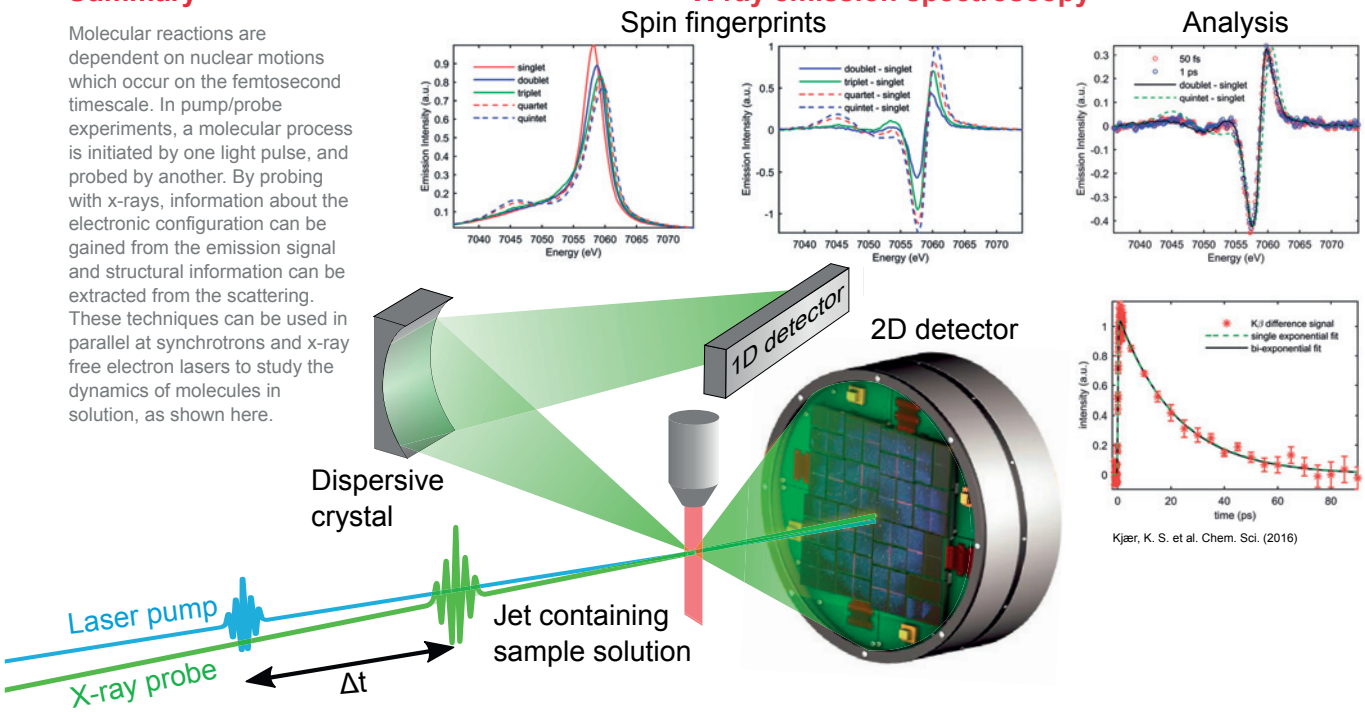

Kjær, K. S. et al. Chem. Sci. (2016)

Application - increasing light-harvesting performance

The first step in light-harvesting is the conversion of sunlight to electrical energy, which can then be transferred to an acceptor. Abundant elements like iron suffer from shortlived charge transfer (MLCT) states, making electron extraction inefficient. By introducing strongly interacting ligands that destabilize lower lying states, the lifetimes of the MLCT states can be extended. X-ray emission spectroscopy and scattering can be used to probe the lifetimes, spin states and structure of the excited states and guide the design more efficient light-harvesting complexes.

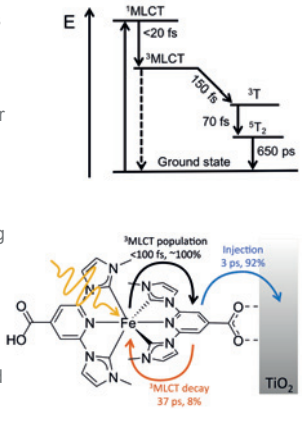

Harlang, T. C. B. et al. Nat. Chem. 7, 883–889 (2015)

X-ray diffuse scattering

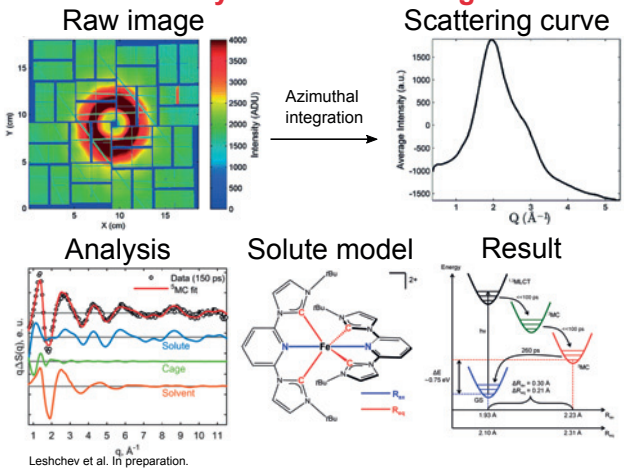

Leshchev et al. In preparation.

Tobias C. B. Harlang
Postdoc, DTU/LU
tcbh@fysik.dtu.dk

Residual stress and hydrogen effect on Ti-6Al-4V alloys produced by additive manufacturing

T. Maimaitiyili[1], R. Woracek[2], C. Bjerken[1], M. Strobl[2]
[1]Malmö University, Malmö, Sweden and [2]ESS AB, Lund, Sweden

Objective

- Better understanding the relation between additive manufacturing (AM) process parameters and material microstructure.
- Residual stress and hydrogen effect on additive manufactured Ti-6Al-4V alloys.
- Hydrogen related degradation of Ti-6Al-4V.

Background

Need for affordable, personalized implants and complex designed, light weight but strong structural parts in aerospace and automation industry made titanium based materials and additive manufacturing very interesting [1-3]. It is known that the properties and performance of additively manufactured materials are strongly effected by processing parameters of AM [1-3]. However, the relation between the AM process parameters, microstructural development, defect formation, grain growth, residual stress, hydride formation and hydride phase transformation are not well understood.

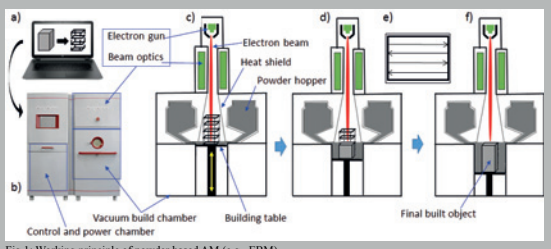

Fig.1: Working principle of powder based AM (e.g., EBM).

Experimental procedure

Materials

- Commercial grade Ti6Al4V powder is used for AM.
- EBM scanning speed, beam current and build size are investigated.
- The high temperature, gas loading setup is used for hydrogenation.
- Charged at 300 °C.
- Ti6Al4V produced by scanning laser melting (SLM) and laser metal deposition (LMD) going to be investigated.

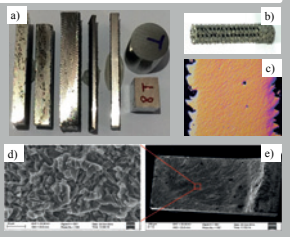

Fig.2: a) Cross-section of selected EBM built material; b) Scafold structure; c) Optical micrograph; d) & e) SEM image of fracture surface of hydrogenated sample.

Table1: Selected Sample processing parameters.

Samples	S. [mm/s]	Current [mA]
s2x1	180/650	8./9
s2y2	180/651	8./9
s2y3	180/652	8./9
s3y3	180/575	8./9
s4y3	180/650	8./9

Diffraction experiments

- The I12 beam line (Fig.3) at Diamond and ESS test beam line at HZB are used for investigation.
- The in-situ heating and mechanical loading experiments on hydrogenated and as built materials are planned.
- Texture analysis, grain and defect mapping will be carried out.

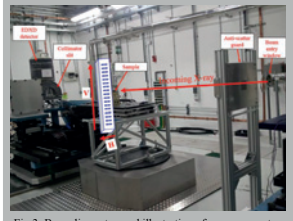

Fig.3: Beam line setup and illustration of measurements.

Results

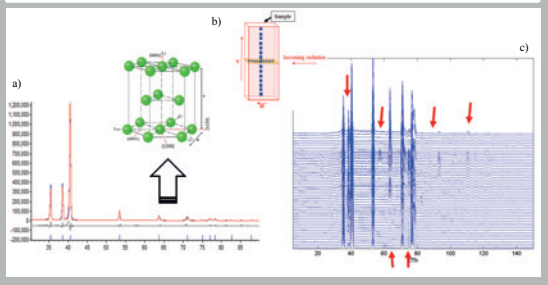

Fig.4: a) Typical Rietveld fit of the Ti6Al4V (at 25 °C), b) Illustration of measurements, c) assembled diffraction patterns of one of the hydrogenated EBM Ti6Al4V.

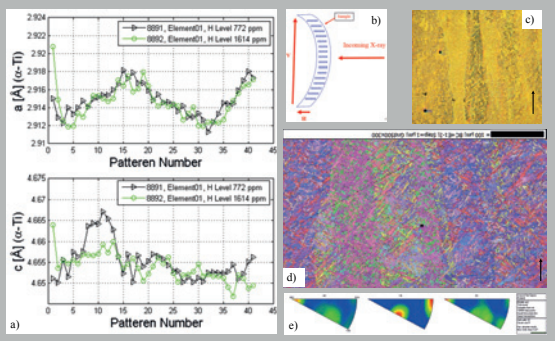

Fig.5: a) Lattice parameters of α-Ti respect to loading; b) illustration of sample loading and measurments; c) optical micrograph of EBM Ti6Al4V along build direction; d) EBSD pattern from upper part of the built and e) corresponding pole figure.

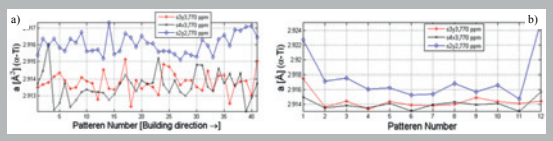

Fig.6: The lattice parameters of α-Ti a) along build direction and b) at build plane obtained by Rietveld fitting procedure.

Table 2: The refined crystal structure parameters of common phases in hydrogenated EBM built Ti6Al4V at room temperatures.

Phase	Structure	Space group	a(Å)	c(Å)
α(Ti)	HCP	P63/mmc	2.95111	4.68433
β(Ti)	BCC	Im-3m	3.27651	3.27651
δ(TiH_x)	FCC	Fm-3m	4.454	4.454

Conclusions

- The present study has demonstrated the potential use of neutron and synchrotron X-ray diffraction on studies of additive manufactured titanium alloys.
- The high temperature gas loading procedure is an effective way to produce hydride samples for investigation of Ti-hydrides.
- The influence of EBM processing parameters to residual stress and hydride precipitation are not significant.
- The stress formation trend at both building plane and building direction were not observed.
- The material build size, such as sample thickness showed stronger effect than beam current and beam size.
- Thicker sample produced higher residual stress.
- High hydrogen concentration increase the stress level but the difference between 700 and 1400 PPM is not so significant.
- EBM built material showed different texture and phase distribution respect to build height.

References

1. G. Lutjering and J.C. Williams. Titanium. Springer, 2007. 9783540713975.
2. D. Herzog, V. Seyda, E. Wycisk, C. Emmelmann. Acta Materialia 2016;117-371.
3. L.E. Murr, 2009, Materials Characterization, ss. 96-105

Corresponding author: tuerdi.maimaitiyili@mah.se

Acknowledgements: InterReg ESS & MaxIV: Cross Border Science and Society financially support the project (MAH-003). Diamond light source (EE7858) and HZB are provided beam time. Norbert Schäfer, J. Blomqvist, M.S. Blackmur, Axel Steuwer and Michael Drakopoulos helped us to collect EBSD and synchrotron data.

Molecular Exchange in Micelles with Partly Crystallised Cores

UiO : Department of Chemistry
University of Oslo

T. Zinn[1], L. Willner[2] , V. Pipich[2] , D. Richter[2] and R. Lund[1]

[1] Department of Chemistry, University of Oslo, Postboks 1033 Blindern, 0315 Oslo. Norway
[2] Jülich Centre for Neutron Science (JCNS), Forschungszentrum Jülich GmbH, 52428 Jülich, Germany

Motivation

To understand the basic properties of biological membranes require a detailed knowledge of its properties i.e. structure and in particular the kinetic pathway of unimer expulsion **[1]**.

We show by combining calorimetric, volumetric and structural measurements that micelles act like confined systems following a Gibbs-Thomson behavior **[2]**. As by Using kinetic contrast variation and time-resolved small-angle neutron scattering (TR-SANS) we investigate the role of crystallisation on the molecular exchange kinetics. We show that there are entropic and enthalpies contributions to the free energy of the kinetic process **[3]** and experimentally verify theoretical predictions **[4]**.

Time-Resolved SANS Technique

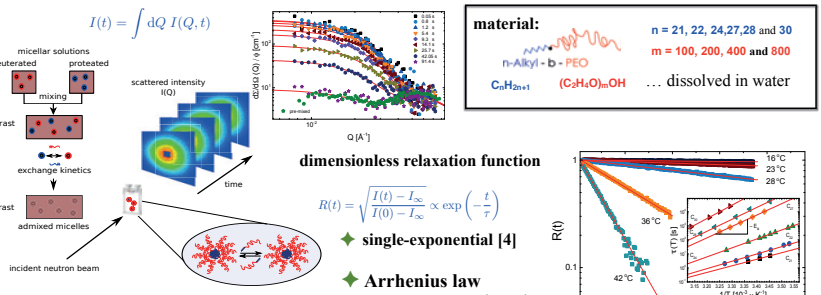

dimensionless relaxation function

$$R(t) = \sqrt{\frac{I(t) - I_\infty}{I(0) - I_\infty}} \propto \exp\left(-\frac{t}{\tau}\right)$$

✦ **single-exponential [4]**

✦ **Arrhenius law**

$$\tau = \tau_0 \cdot \exp\left(\frac{E_a}{k_B T}\right)$$

molecular (single unimer) exchange

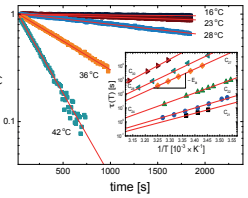

Fig.1: R(t,T) of C_{30}-PEO5 and Arrhenius-plot for C_n-PEO5 (inset).

Gibbs-Thomson Behaviour

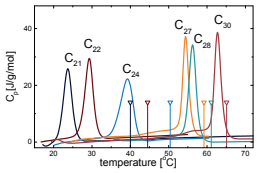

Fig.2: nano-DSC thermograms of C_n-PEO5 micellar solutions (heating rate 2 K/min) and melting point of alkane C_nH_{2n+2}.

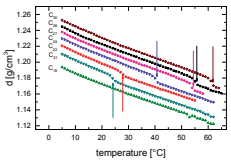

Fig.3: Apparent density as a function of temperature and n-alkyl chain length

✦ **first-order phase transition**
✦ **melting point depression**

Molecular Exchange I - core size

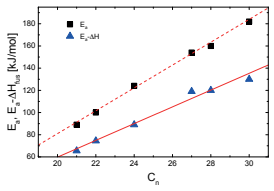

Fig.5: Activation energies E_a as a function of hydrophobic sticker chain length *n* and E_a corrected by ΔH_{fus}.

corrected activation energy

$$E_a^0 = E_a - \Delta H_{fus} \propto n^\beta$$

chain conformation [1]

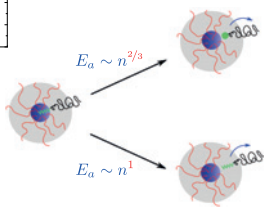

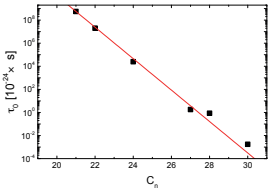

Fig.6: $\ln\tau_0$ vs. n demonstrating a significant contribution of conformational entropy.

… **pre-exponential factor** reflects the **entropic** contribution

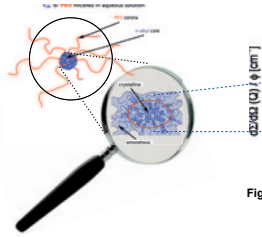

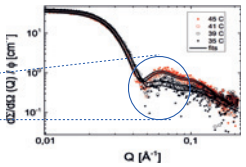

Fig.4: SAXS scattering profile C_{24}-PEO5.

✦ **melting point depression of n-alkane confined in micelles** follow **Gibbs-Thomson behaviour [2]**

$$\Delta T_m \propto \gamma / R_{core}$$

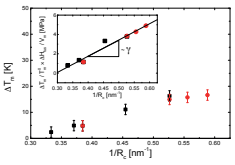

✦ **relaxation time**

$$\tau = \tau_0^\dagger \, e^{-\Delta S^\ddagger / R} \, e^{\Delta H^\ddagger / RT}$$

Eyring equation **[3, 5]**

$$\left\{ \begin{array}{ll} \Delta H^\ddagger = E_a & \tau_0 = \tau_0^\dagger \, e^{-\Delta S^\ddagger / k_B} \\ \textbf{enthalpic} & \textbf{entropic} \end{array} \right\}$$

✦ **conformational entropy**

$$\left\{ \begin{array}{l} \ln \tau_0 \propto n \quad \Delta S_{fus} \propto n \\ \Delta S^\ddagger = \Delta S_{fus} + \Delta S_{ex} \end{array} \right\} \Delta S_{ex} \propto n$$

… conformational degree of freedom within the micellar core is very limited compared to free n-alkane chains in solution

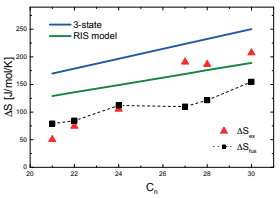

Fig.7: Experimentally conformational entropy and the individual components i.e. ΔS_{fus} and ΔS_{ex} in comparison to theoretical calculations: *3-state model* and *RIS model*.

Molecular Exchange II - corona size [6]

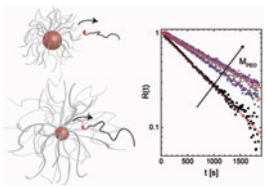

Fig.8: R(t) for C_{27}-PEOx with increasing molecular weight of the PEO corona block.

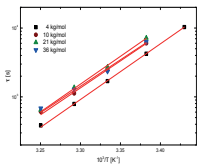

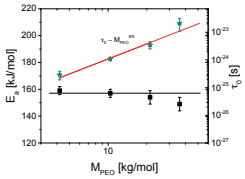

✦ **constant activation energy and slower diffusion in corona**

✦ **kinetics slowing down as predicted [4] :** $\tau(T) \sim M_{corona}^{9/5} \cdot \exp\left(\frac{E_a(n)}{k_B T}\right)$

References

[1] R. Lund, L. Willner, D. Richter, Adv. Polym. Sci. (2013), **204**, 51

[2] T. Zinn, L. Willner, R. Lund, Phys. Rev. Lett. (2014), **113**, 238305

[3] T. Zinn, L. Willner, V. Pipich, D. Richter, R. Lund, ACS Macro Lett. (2015), **4**, 661

[4] A. Halperin, S. Alexander, Macromolecules (1989), **22**, 2403

[5] E. G. Aniansson, S. N. Wall, M. Almgren, H. Hoffmann, I. Kielmann, W. Ulbrich, R. Zana, J. Lang, C. Tondre, J. Phys. Chem. (1976), **80**, 905

[6] T. Zinn, L. Willen, V. Popich, D. Richter, R. Lund ACS Macro Lett. (2016), **5**, 884

Acknowledgements: Forskningsrådet SYNKNOYT program (218411 and 228573)

Contact: thomas.zinn@kjemi.uio.no

Interreg Öresund-Kattegat-Skagerrak European Regional Development Fund
EUROPEAN UNION
ESS & MAX IV: Cross Border Science and Society

List of participants

Registered participants MAX4ESSFUN annual meeting 2016

Name	Institution	Email
Gregers Rom Andersen	Aarhus University	gra@mbg.au.dk
Hazel Reardon	Aarhus University	hazel@inano.au.dk
Jacob Becker	Aarhus University	jbecker@chem.au.dk
Joachim Pold Vilstrup	Aarhus University	jpv@mbg.au.dk
Kristian Stødkilde-Jørgensen	Aarhus University	kst@biomed.au.dk
Marlene Uglebjerg Sørensen	Aarhus University	marlene.soerensen@mbg.au.dk
Poul Nissen	Aarhus University	pn@mbg.au.dk
Søren Thirup	Aarhus University	sth@mbg.au.dk
Johan Ahlström	Chalmers	johan.ahlstrom@chalmers.se
Nico Torino	Chalmers	torino@chalmers.se
Olle Windelius	Chalmers	wiolle@chalmers.se
Esko Oksanen	ESS	esko.oksanen@esss.se
Marcus Strobl	ESS	Markus.strobl@esss.se
Pascale Deen	ESS	pascale.deen@esss.se
Robin Woracek	ESS	robin.woracek@esss.se
Zoë Fisher	ESS	zoe.fisher@esss.se
Madhuri Nagabhushanam	Industry	madhuri.nagabhushanam@gmail.com
Vivek Chaturvedi	Industry	vivekjeechaturvedi@gmail.com
Magnus Helgerud Sørby	IET, Kjeller	magnuss@ife.no
Amal el Nahhas	Lund University	amal.el_nahhas@chemphys.lu.se
Anders Mikkelsen	Lund University	anders.mikkelsen@sljus.lu.se
Bansi Koul	Lund University	bansi.koul@med.lu.se
Bernardo M. S. Oliveira	Lund University	dok14bmo@student.lu.se
Cecilia Emanuelsson	Lund University	Cecilia.Emanuelsson@biochemistry.lu.se
Cedric Dicko	Lund University	cedric.dicko@tbiokem.lth.se
Charlotte J. Sparrenbom	Lund University	charlotte.sparrenbom@geol.lu.se
Christos Levcopoulos	Lund University	Christos.Levcopoulos@cs.lth.se
Claes von Wachenfeldt	Lund University	claes.von_wachenfeldt@biol.lu.se
Claudio Verdozzi	Lund University	claudio.verdozzi@teorfys.lu.se
Derek Logan	Lund University	derek.logan@biochemistry.lu.se
Dmytro Orlov	Lund University	dmytro.orlov@material.lth.se
Emil Rofors	Lund University	emil.rofors@nuclear.lu.se
Emily Baird	Lund University	emily.baird@biol.lu.se
Enamul Mojumdar	Lund University	enamul.mojumdar@fkem1.lu.se
Ferdi Aryasetiawan	Lund University	ferdi.aryasetiawan@teorfys.lu.se
Fredrik Nilsson	Lund University	fredrik.nilsson@teorfys.lu.se
Gavin Taylor	Lund University	gavin.taylor@biol.lu.se
Gry Lyngsie	Lund University	gry.lyngsie@cec.lu.se
Gudrun Rutsdottir	Lund University	gudrun.rutsdottir@biochemistry.lu.se
Guilherme Ferreira	Lund University	guilhermeferreyra@gmail.com
Helena Filipsson	Lund University	helena.filipsson@geol.lu.se
Hossein Sina	Lund University	hossein.sina@material.lu.se
Håkan Arheden	Lund University	hakan.arheden@med.lu.se

Janina Sprenger	Lund University	Janina.Sprenger@biochemistry.lu.se
Jens Uhlig	Lund University	jens.uhlig@chemphys.lu.se
Jesper Wallentin	Lund University	jesper.wallentin@sljus.lu.se
João Henriques	Lund University	joao.henriques@teokem.lu.se
Jonas Engqvist	Lund University	jonas.engqvist@solid.lth.se
Junsheng Chen	Lund University	junsheng.chen@chemphys.lu.se
Kajsa M. Paulsson	Lund University	kajsa_m.paulsson@med.lu.se
Karin Lindkvist	Lund University	Karin.Lindkvist@med.lu.se
Karin Schillén	Lund University	Karin.Schillen@fkem1.lu.se
Katarina Koruza	Lund University	katarina.koruza@biol.lu.se
Lennart Piculell	Lund University	lennart.piculell@fkem1.lu.se
Malin Elvén	Lund University	malin.elven@med.lu.se
Malin Zackrisson Oskolkova	Lund University	malin.zackrisson@fkem1.lu.se
Manish Singh	Lund University	manish.singh@tbiokem.lth.se
Marie Skepö	Lund University	marie.skepo@teokem.lu.se
Marta Gubitosi	Lund University	marta.gubitosi@fkem1.lu.se
Martin Bech	Lund University	martin.bech@med.lu.se
Martin Stankovski	Lund University	martin.stankovski@fsi.lu.se
Matti Ristinmaa	Lund University	matti.ristinmaa@solid.lth.se
Miroslav Hopjan	Lund University	miroslav.hopjan@teorfys.lu.se
Nadine Quintana Krupinski	Lund University	nadine.krupinski@geol.lu.se
Nicholai Mauritzson	Lund University	nat13nma@student.lu.se
Nina Ahlbeck	Lund University	nina.ahlbeck@luopen.lu.se
Oxana Klementieva	Lund University	oxana.klementieva@med.lu.se
Per Persson	Lund University	per.persson@biol.lu.se
Per Åke Malmqvist	Lund University	Per-Ake.Malmqvist@teokem.lu.se
Peter Schurtenberger	Lund University	peter.schurtenberger@fkem1.lu.se
Quoc Dat Pham	Lund University	dat.pham@fkem1.lu.se
Rainer Timm	Lund University	rainer.timm@sljus.lu.se
Raminta Venskutonyte	Lund University	raminta.venskutonyte@med.lu.se
Reine Wallenberg	Lund University	reine.wallenberg@chem.lu.se
Sara Johansson	Lund University	sara.johansson@tg.lth.se
Silke Engelholm	Lund University	silke.engelholm@skane.se
Stacey Sörensen	Lund University	stacey.sorensen@sljus.lu.se
Stefan Kuczera	Lund University	stefan.kuczera@fkem1.lu.se
Stephen Hall	Lund University	Stephen.alexander.hall@gmail.com
Susanna Horsefield	Lund University	susanna.horsefield@biochemistry.lu.se
Ulf Olsson	Lund University	ulf.olsson@fkem1.lu.se
Valera Veryazov	Lund University	valera.veryazov@teokem.lu.se
Vinardas Kelpsas	Lund University	vinardas.kelpsas@biol.lu.se
Wolfgang Knecht	Lund University	wolfgang.knecht@biol.lu.se
Celina Wierzbicka	Malmö University	celina.wierzbicka@mah.se
Christina Bjerkén	Malmö University	christina.bjerken@mah.se
Haddel Ali Shoker	Malmö University	haddelshoker@gmail.com
Marite Cardenas	Malmö University	marite.cardenas@mah.se
Tuerdi Maimaityili	Malmö University	tuerdi.maimaitiyili@mah.se

Anders Engdahl	MAX IV	anders.engdahl@maxiv.lu.se
Ann Terry	MAX IV	ann.terry@maxiv.lu.se
Chris Ward	MAX IV	christopher.ward@maxiv.lu.se
Jie Nan	MAX IV	jie.nan@maxiv.lu.se
Johan Unge	MAX IV	johan.unge@maxiv.lu.se
Kajsa Sigfridsson Clauss	MAX IV	kajsa.sigfridsson_clauss@maxiv.lu.se
Katarina Norén	MAX IV	katarina.noren@maxiv.lu.se
Marjolein Thunnissen	MAX IV	marjolein.thunnissen@maxiv.lu.se
Thomas Ursby	MAX IV	thomas.ursby@maxiv.lu.se
Tomas Lundqvist	MAX IV	tomas.lundqvist@maxiv.lu.se
Tomas Plivelic	MAX IV	tomas.plivelic@maxiv.lu.se
Yngve Cerenius	MAX IV	yngve.cerenius@maxlab.lu.se
Eller Yannick	Other	yannick.eller@students.unibe.ch
Eskil Mårtensson	Region Skåne	eskil.martensson@skane.se
Jakob Øster	Capital Region of Denmark	jakob.oester@regionh.dk
Mads Beich-Frandsen	Other	mads.beich.frandsen@icloud.com
Susan Cooper	Other	scooper2@uoregon.edu
Anders Bjorholm Dahl	DTU	abda@dtu.dk
Anna Fedrigo	DTU	annfe@dtu.dk
Annika Diederichs	DTU	anmad@mek.dtu.dk
Giovanni Fevola	DTU	gfev@dtu.dk
Henning Nicolajsen	DTU	henning@fysik.dtu.dk
Hilmar Danielsen	DTU	hkda@dtu.dk
Jens Wenzel Andreasen	DTU	jewa@dtu.dk
Kenny Ståhl	DTU	kenny@kemi.dtu.dk
Lise Ørduk Sandberg	DTU	mail@lisesandberg.com
Luise Theil Kuhn	DTU	luku@dtu.dk
Oleg Mishin	DTU	olmi@dtu.dk
Pernille Harris	DTU	ph@kemi.dtu.dk
Pernille Sønderby	DTU	perso@kemi.dtu.dk
Somrita Dhar	DTU	sodh@dtu.dk
Tobias Harlang	DTU	tcbh@fysik.dtu.dk
Ulf Molich	DTU	ulfmol@kemi.dtu.dk
Alberto Viñas	University of Copenhagen	a.vinyas@gmail.com
Dirk Müter	University of Copenhagen	mueter@nano.ku.dk
Ellen Juel Nielsen	University of Copenhagen	ellen.nielsen@chem.ku.dk
Jeppe Knudsen Baden	University of Copenhagen	jeppebaden@gmail.com
Johannes Beil	University of Copenhagen	johannes.beil@nbi.dk
Kell Mortensen	University of Copenhagen	kell@nbi.dk
Kirsten Marie Jensen	University of Copenhagen	kirsten@chem.ku.dk
Linda Udby	University of Copenhagen	udby@nbi.dk
Sine Larsen	University of Copenhagen	sine@chem.ku.dk
Theis Solling	University of Copenhagen	theis@chem.ku.dk
Troels Lindah Christiansen	University of Copenhagen	Troels@chem.ku.dk
Folmer Fredslund	University of Copenhagen	folmer@chem.ku.dk
Dag Hanstorp	University of Gothenburg	dag.hanstorp@gu.se

Florian Schmitz	University of Gothenburg	florian.schmitz@gu.se
Gisela Brändén	University of Gothenburg	gisela.branden@gu.se
Mikael Andersson	University of Gothenburg	insuliner@gmail.com
Anja Olafsen Sjåstad	University of Oslo	a.o.sjastad@kjemi.uio.no
Francois Renard	University of Oslo	francois.renard@geo.uio.no
Helmer Fjellvåg	University of Oslo	helmerf@kjemi.uio.no
Jakob Stensgaard Diget	University of Oslo	j.s.diget@kjemi.uio.no
K. Kristoffer Andersson	University of Oslo	k.k.andersson@ibv.uio.no
Reidar Lund	University of Oslo	reidar.lund@kjemi.uio.no
Sabrina Sartori	University of Oslo	sabrina.sartori@fys.uio.no
Thomas Zinn	University of Oslo	tzinn@kjemi.uio.no

Printed by Media-Tryck | Lund University 2016

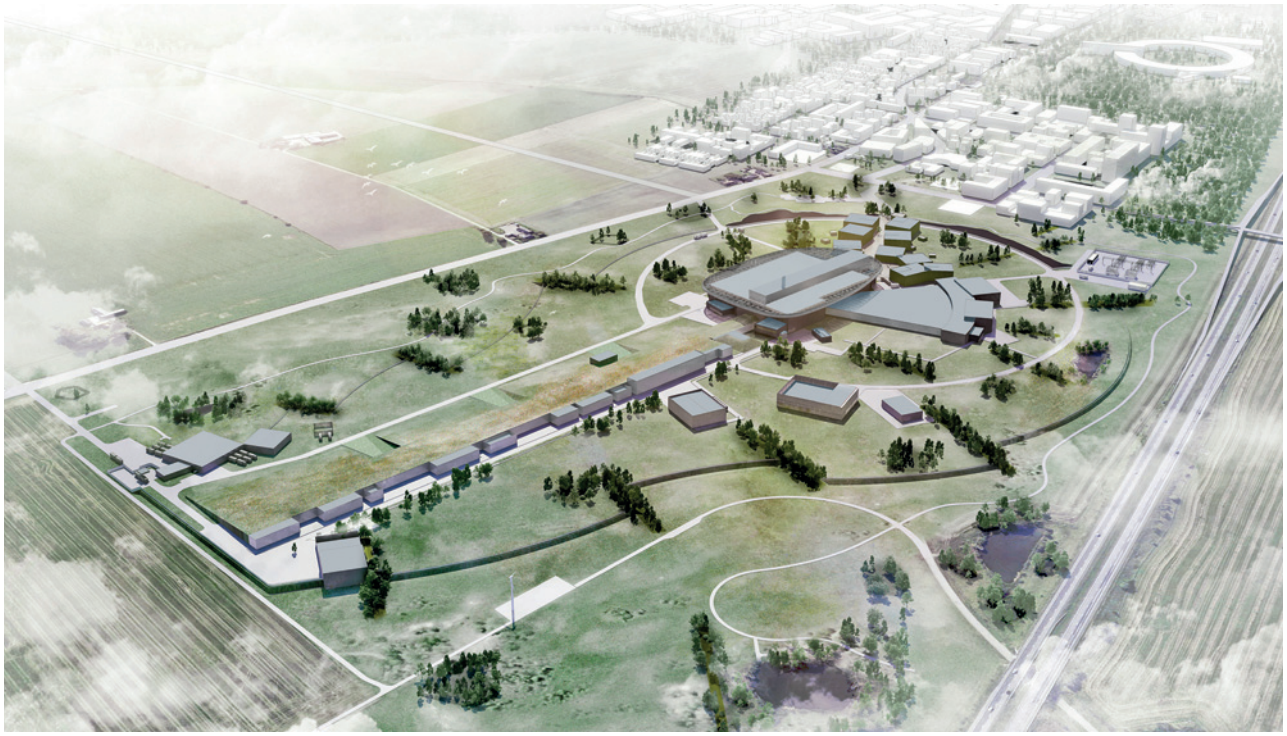

European Spallation Source ERIC

MAX IV synchrotron radiation laboratry